

AD-A038 734

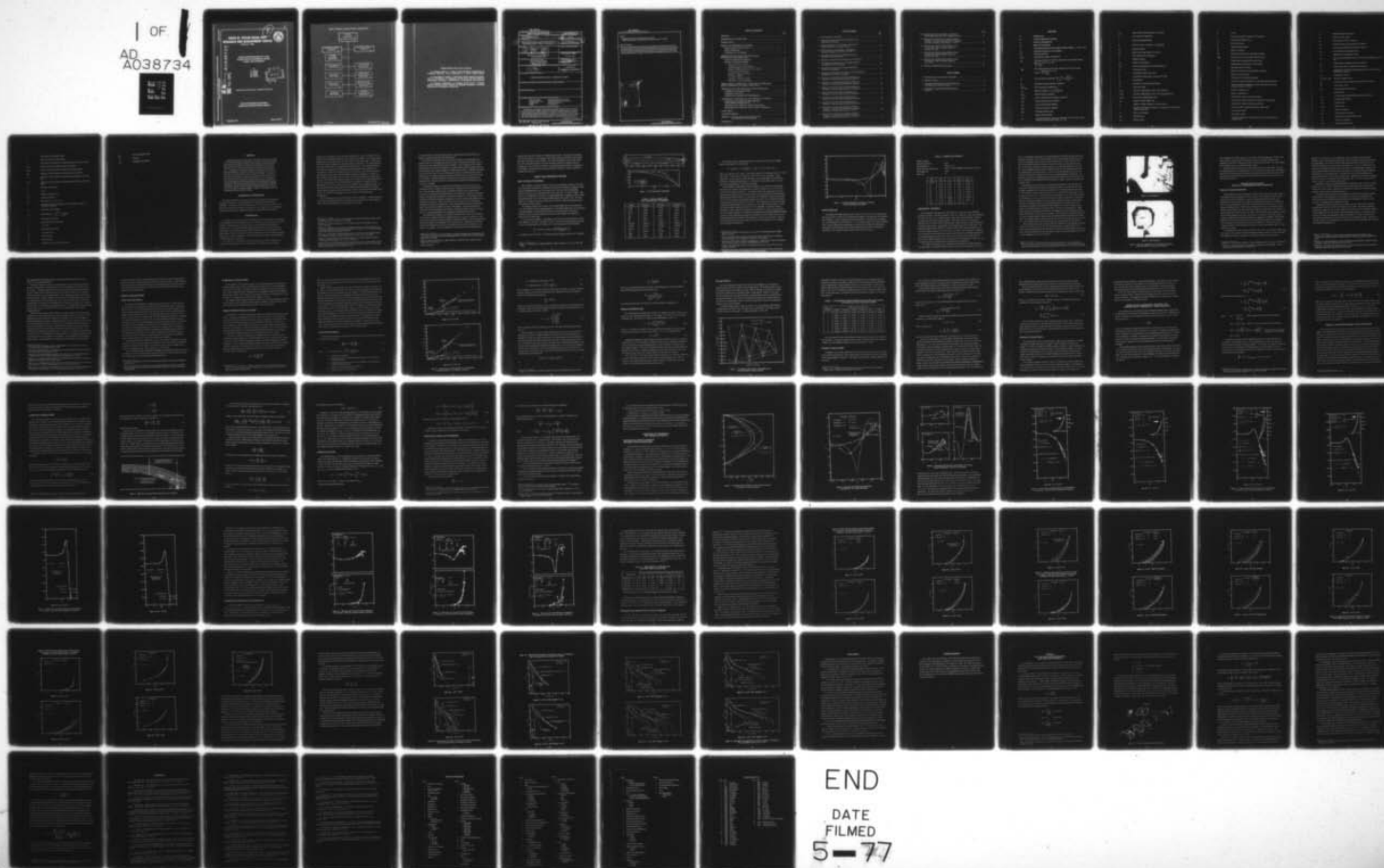
DAVID W TAYLOR NAVAL SHIP RESEARCH AND DEVELOPMENT CE--ETC F/G 20/4  
PROPELLER/STERN/BOUNDARY-LAYER INTERACTION ON AXISYMMETRIC BODI--ETC(U)  
DEC 76 T T HUANG, H T WANG, N SANTELLI

UNCLASSIFIED

DTNSRDC-76-0113

NL

1 OF  
AD  
A038734



Report 76-0113

PROPELLER/STERN/BOUNDARY-LAYER INTERACTION ON AXISYMMETRIC BODIES:  
THEORY AND EXPERIMENT

AD No. **ADA 038734**  
**DDC FILE COPY**

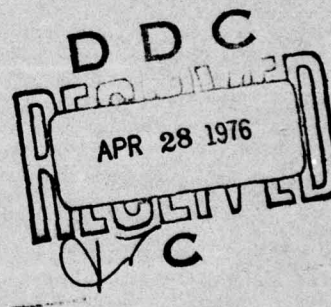
**DAVID W. TAYLOR NAVAL SHIP  
RESEARCH AND DEVELOPMENT CENTER**

Bethesda, Md. 20084



**PROPELLER/STERN/BOUNDARY-LAYER  
INTERACTION ON AXISYMMETRIC BODIES:  
THEORY AND EXPERIMENT**

by  
T.T. Huang  
H.T. Wang  
N. Santelli  
N.C. Groves



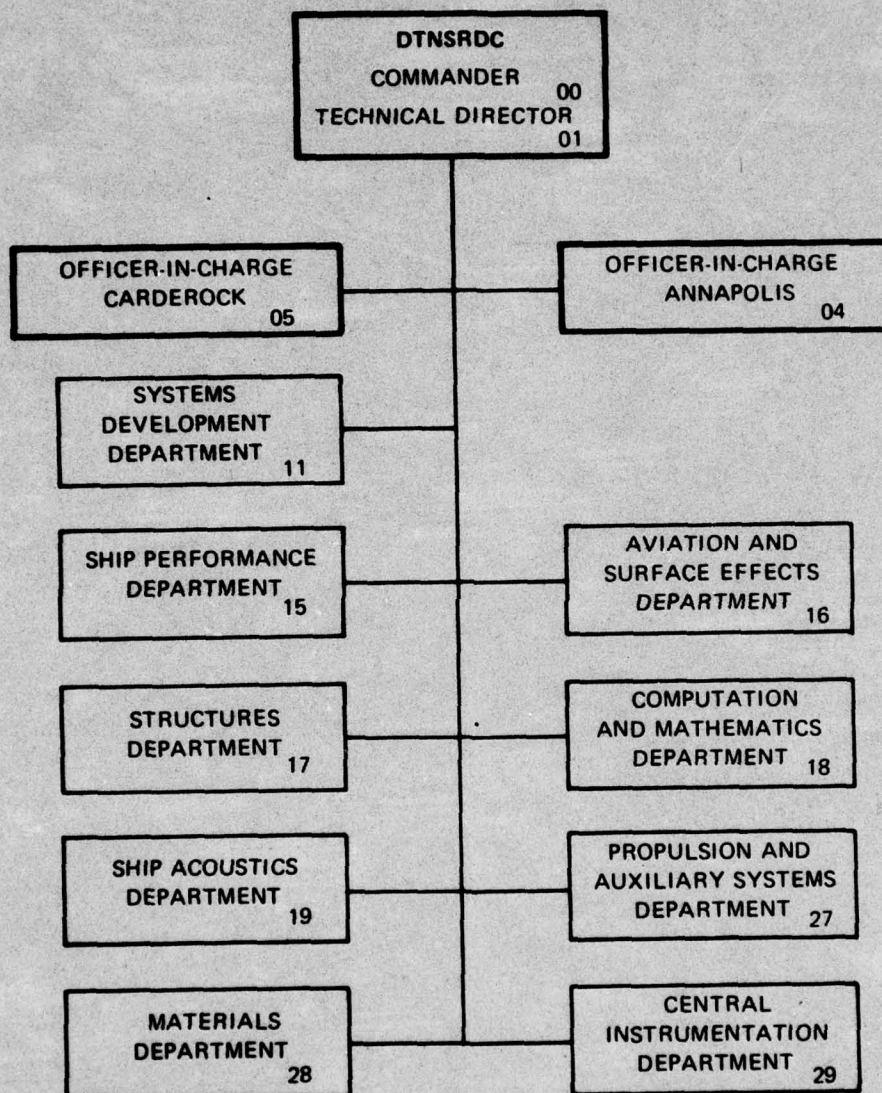
APPROVED FOR PUBLIC RELEASE: DISTRIBUTION UNLIMITED

**SHIP PERFORMANCE DEPARTMENT  
RESEARCH AND DEVELOPMENT REPORT**

December 1976

Report 76-0113

## MAJOR DTNSRDC ORGANIZATIONAL COMPONENTS





**DTNSRDC ISSUES THREE TYPES OF REPORTS**

**(1) DTNSRDC REPORTS, A FORMAL SERIES PUBLISHING INFORMATION OF PERMANENT TECHNICAL VALUE, DESIGNATED BY A SERIAL REPORT NUMBER.**

**(2) DEPARTMENTAL REPORTS, A SEMIFORMAL SERIES, RECORDING INFORMATION OF A PRELIMINARY OR TEMPORARY NATURE, OR OF LIMITED INTEREST OR SIGNIFICANCE, CARRYING A DEPARTMENTAL ALPHANUMERIC IDENTIFICATION.**

**(3) TECHNICAL MEMORANDA, AN INFORMAL SERIES, USUALLY INTERNAL WORKING PAPERS OR DIRECT REPORTS TO SPONSORS, NUMBERED AS TM SERIES REPORTS; NOT FOR GENERAL DISTRIBUTION.**



UNCLASSIFIED

SECURITY CLASSIFICATION OF THIS PAGE (When Data Entered)

REPORT DOCUMENTATION PAGE		READ INSTRUCTIONS BEFORE COMPLETING FORM
1. REPORT NUMBER (14) DTNSRDC-76-0113	2. GOVT ACCESSION NO.	3. RECIPIENT'S CATALOG NUMBER (9) and
4. TITLE (and Subtitle) PROPELLER/STERN/BOUNDARY-LAYER INTERACTION ON AXISYMMETRIC BODIES: THEORY AND EXPERIMENT		5. TYPE OF REPORT & PERIOD COVERED Research & Development report
7. AUTHOR(s) (10) T.T. Huang, N. Santelli H.T. Wang, N.C. Groves		6. PERFORMING ORG. REPORT NUMBER
9. PERFORMING ORGANIZATION NAME AND ADDRESS David W. Taylor Naval Ship R&D Center Bethesda, Maryland 20084		8. CONTRACT OR GRANT NUMBER(s)
11. CONTROLLING OFFICE NAME AND ADDRESS Naval Sea Systems Command Materials and Mechanics Division Washington, D.C. 20362		10. PROGRAM ELEMENT, PROJECT, TASK AREA & WORK UNIT NUMBERS (See reverse side)
14. MONITORING AGENCY NAME & ADDRESS (if different from Controlling Office) (12) 84p.		12. REPORT DATE (10) December 1976
		13. NUMBER OF PAGES 87
		15. SECURITY CLASS. (of this report) UNCLASSIFIED
		15a. DECLASSIFICATION/DOWNGRADING SCHEDULE
16. DISTRIBUTION STATEMENT (of this Report)  APPROVED FOR PUBLIC RELEASE: DISTRIBUTION UNLIMITED		
17. DISTRIBUTION STATEMENT (of the abstract entered in Block 20, if different from Report)		
18. SUPPLEMENTARY NOTES		
19. KEY WORDS (Continue on reverse side if necessary and identify by block number) Axisymmetric Bodies      Nominal and Effective Velocity Profile Turbulent Boundary Layer      Propeller-Stern-Boundary-Layer Interaction Turbulent Wake      Propeller-Hull Interaction Propeller      Thrust Deduction		
20. ABSTRACT (Continue on reverse side if necessary and identify by block number) Measurements of the boundary-layer characteristics and pressure distributions on three axisymmetric bodies with and without a propeller in operation are correlated with analytical techniques for computing (1) the interaction between the hull boundary layer flow and the potential flow and (2) the interaction between the operating propeller and the thick stern boundary layer. The agreement between the measured and computed shear stresses, pressure distributions, and velocity profiles was satisfactory except over the last 5 percent of body length on the two fullest afterbodies. An inviscid propeller-stern-boundary-layer (Continued on reverse side)		

DD FORM 1473 1 JAN 73

EDITION OF 1 NOV 65 IS OBSOLETE  
S/N 0102-LF-014-6601

UNCLASSIFIED

SECURITY CLASSIFICATION OF THIS PAGE (When Data Entered)

287682

UNCLASSIFIED

SECURITY CLASSIFICATION OF THIS PAGE (When Data Entered)

Block 10

IED funding under Element 62766N, Work Unit 1-1552-119.

NAVMAT direct laboratory funding under Element 62543N, Work Unit 1-1520-004.

Block 20 (continued)

interaction model was developed and found to give accurate predictions of effective velocity profiles. The experimental results show that the potential-flow propeller-hull interaction methods give accurate predictions for thrust deduction and the propeller-induced pressure distribution. The present analytical techniques will be useful for predicting the full-scale effective velocity profile for propeller design when account is taken of the effects of Reynolds number, roughness, and propeller suction in modifying the nominal velocity profiles.

NTIS		White Section	<input checked="checked" type="checkbox"/>
U.S.		Puff Section	<input type="checkbox"/>
UNCLASSIFIED			<input type="checkbox"/>
IDENTIFICATION			
BY			
DISTRIBUTION/AVAILABILITY CODES			
DIS. STATE. & SERIAL			
A			

UNCLASSIFIED

SECURITY CLASSIFICATION OF THIS PAGE (When Data Entered)

## TABLE OF CONTENTS

	Page
ABSTRACT .....	1
ADMINISTRATIVE INFORMATION .....	1
INTRODUCTION .....	1
MODELS AND EXPERIMENTAL METHODS .....	4
BODY OF REVOLUTION MODELS .....	4
MODEL PROPELLER .....	7
EXPERIMENTAL TECHNIQUE .....	8
METHOD FOR CALCULATING POTENTIAL-FLOW- BOUNDARY-LAYER INTERACTION .....	11
SURVEY OF PREVIOUS METHODS .....	11
PRESENT ITERATION SCHEME .....	14
Outline of the Present Scheme .....	14
Douglas-Neumann Computer Program .....	15
Douglas CS Differential Boundary-Layer Method .....	15
The Granville Wake Relations .....	16
Modeling of Displacement Body .....	19
Convergence Behavior .....	20
Calculation of Output Variables .....	21
Description of Computer Program .....	23
PROPELLER-HULL INTERACTION: FRICTIONAL AND PRESSURE- DEFECT COMPONENTS OF THRUST DEDUCTION .....	24
PROPELLER AND STERN BOUNDARY-LAYER INTERACTION .....	26
THEORETICAL CONSIDERATIONS .....	27
NUMERICAL SOLUTION .....	30
PREDICTION OF PROPELLER PERFORMANCE .....	31
COMPARISON OF EXPERIMENTAL AND THEORETICAL RESULTS.....	33
MEASURED AND COMPUTED PRESSURE AND SHEAR STRESS DISTRIBUTIONS.....	33
MEASURED AND COMPUTED THRUST DEDUCTION .....	43
MEASURED AND COMPUTED AXIAL VELOCITY PROFILES .....	47
CONCLUSIONS .....	63
ACKNOWLEDGMENTS .....	64
APPENDIX - OFF-AXIS DUAL-BEAM BACKSCATTER LASER DOPPLER VELOCIMETER .....	65
REFERENCES .....	70



## LIST OF FIGURES

	Page
1 – The Axisymmetric Afterbodies .....	5
2 – Computed Distributions of Pressure Coefficient on the Axisymmetric Afterbodies .....	7
3 – Optical Arrangement of Laser Doppler Velocimeter in the Wind Tunnel of the Anechoic Facility .....	10
4 – Determination of Virtual Origin of Axisymmetrical Turbulent Boundary Layer behind a Trip Wire .....	17
5 – Convergence Characteristics of Boundary-Layer and Potential-Flow Iteration Scheme .....	20
6 – Illustration of Propeller/Stern Boundary-Layer Interaction .....	28
7 – Nondimensional Circulation for the Propeller Operated in the Wake of Three Afterbodies .....	34
8 – Measured and Computed Stern Pressure Distribution for the Three Afterbodies .....	35
9 – Measured and Computed Viscous Effect on the Stern Pressure Distributions of the Three Afterbodies .....	36
10 – Measured and Computed Skin Friction Distribution on Afterbody 1 with and without Propeller in Operation .....	37
11 – Measured and Computed Skin Friction Distribution on Afterbody 2 with and without Propeller in Operation .....	39
12 – Measured and Computed Skin Friction Distribution on Afterbody 3 with and without Propeller in Operation .....	41
13 – Measured and Computed Pressure Distribution on Afterbody 1 with and without Propeller in Operation .....	44
14 – Measured and Computed Pressure Distribution on Afterbody 2 with and without Propeller in Operation .....	45
15 – Measured and Computed Pressure Distribution on Afterbody 3 with and without Propeller in Operation .....	46
16 – Measured and Computed Axial Velocity Profiles on Afterbody 1 with and without Propeller in Operation at Different X/L Ratios and with $R_n = 5.9 \times 10^6$ .....	49
17 – Measured and Computed Axial Velocity Profiles on Afterbody 2 with and without Propeller in Operation at Different X/L Ratios and with $R_n = 5.9 \times 10^6$ .....	51

	Page
18 – Measured Axial Velocity Profiles on Afterbody 2 with Propeller Moved $D_p/4$ Aft of Original Location .....	54
19 – Measured and Computed Axial Velocity Profiles on Afterbody 3 with and without Propeller in Operation at Different X/L Ratios and with $R_n = 5.9 \times 10^6$ .....	55
20 – Measured and Computed Axial Velocity Increase on Afterbody 1 Due to Propeller Suction at Different X/L Ratios .....	59
21 – Measured and Computed Axial Velocity Increase on Afterbody 2 Due to Propeller Suction at Different X/L Ratios .....	60
22 – Measured and Computed Axial Velocity Increase on Afterbody 3 Due to Propeller Suction at X/L = 0.977 .....	62
23 – Off-Axis, Dual-Beam Backscatter Optics .....	66

#### LIST OF TABLES

1 – Hull Particulars for Axisymmetric Afterbodies .....	5
2 – Propeller Geometry .....	8
3 – Convergence Characteristics of the Boundary-Layer and Potential Flow Iteration Scheme .....	21
4 – Comparison of Computed and Measured Thrust Deduction .....	47

## NOTATION

A	Reference area
a*	Computed displacement thickness
b	Radius of unfocused beam
b <sub>o</sub>	Radius of focused beam
C	Conventional scale factor for the effective velocity profile; $(1 - w_T)/(1 - w_D)$
C <sub>A</sub>	Correlation allowance for hull roughness
C <sub>D</sub>	Wire drag coefficient
C <sub>DFA</sub>	Drag coefficient based on frontal area
C <sub>DG</sub>	Total drag coefficient of the body computed by the Granville formula; $\frac{4\pi\Omega_t}{A} \left( \frac{U_t}{U_o} \right) [7(h_t + 2) + 3]/8$
C <sub>DSY</sub>	Total drag coefficient of the body computed by the Squire-Young formula; $\frac{4\pi\Omega_t}{A} \left( \frac{U_t}{U_o} \right) (h_t + 5)/2$
C <sub>F</sub>	Total skin friction coefficient; $\frac{2\pi}{A} \int_0^L c_f r_o \left( \frac{U_e}{U_o} \right)^2 dx$
$\tilde{C}_F$	Schoenherr frictional resistance coefficient
$(\tilde{C}_F)_{ITTC}$	ITTC model-ship correlation line
C <sub>p</sub>	Pressure coefficient; $(p - p_o) / \left( \frac{1}{2} \right) \rho U_o^2$
(C <sub>p</sub> ) <sub>b</sub>	Bare-hull pressure coefficient
(C <sub>p</sub> ) <sub>p</sub>	Pressure coefficient with propeller in operation
C <sub>pp</sub>	Initial potential pressure coefficient
C <sub>pv</sub>	Viscous pressure drag coefficient
C <sub>pvf</sub>	Final viscous pressure coefficient
$\tilde{C}_{pA}$	Afterbody prismatic ratio
C <sub>r</sub>	Residual drag coefficient
C <sub>T</sub>	Total drag coefficient of the body considered as the total skin friction coefficient and the pressure drag = C <sub>F</sub> + C <sub>pv</sub>



$C_{TS}$	Thrust loading coefficient based on ship speed
$C_\tau$	Local shear stress distribution
$c$	Chord of the propeller blade
$c_f$	Local skin friction coefficient; $\tau_\omega / \left( \frac{1}{2} \rho U_e^2 \right)$
$D_p$	Propeller diameter
$d_o$	Peak-to-peak fringe spacing; $\lambda / (2 \sin \theta / 2)$
$FL$	Focal length of the focusing lens
$f$	Doppler frequency
$f_M$	Camber of the propeller
$G(r)$	Propeller nondimensional circulation distribution
$H$	Total pressure head
$h$	Axisymmetric shape factor $\Lambda^* / \Omega$
$h_t$	Axisymmetric shape factor at the tail of the body
$K$	Wire diameter
$\tilde{K}_1$	Coefficient of the Granville polynomial
$L$	Total body length
$L_A/D$	Afterbody length/diameter ratio of the actual body
$L'_A/D$	Afterbody length/diameter ratio of the mathematical body
$L_E/D$	Bow-entrance length/diameter ratio
$L_M$	Length of parallel middle body
$N$	Number of fringes contained in a probe volume
$n$	Number of revolutions per second of the propeller or unit outward normal of the surface
$P$	Pitch of the propeller
$P_D$	Delivered power
$P_E$	Effective power

$Q$	Torque
$q$	An exponent taken to be equal to 7 by Granville
$q_p$	Propeller sink strength = $2u_a$
$R$	Bare-hull resistance
$R_n$	Length Reynolds number
$R_p$	Radius of propeller
$R_\theta$	Reynolds number based on momentum thickness
$\Delta R_\theta$	Jump of $R_\theta$ due to the parasitic drag of the wire
$r$	Radial distance measured from the body axis
$r_h$	Nondimensional hub diameter of the propeller
$r_{max}$	Maximum radius of the body
$r_p$	Radius of stream surface with propeller in operation
$r_o$	Radius of the body surface
$S_1$	Coefficient of the Granville polynomial
$T$	The period of Doppler frequency $f$ or the delivered propeller thrust
$t$	Subscript denoting conditions at the tail of the body or the thrust deduction fraction; $(T - R)/T$
$t_f$	Frictional component of $t$
$t_p$	Pressure component of $t$
$U_e$	Potential flow velocity on the body surface
$U_p$	Total surface potential velocity in the presence of the propeller
$U_t$	Potential flow velocity at the tail of the body
$U_x$	Velocity at which a particle traverses the probe volume
$\bar{U}_x$	Time-average velocity
$U_o$	Free-stream velocity
$u$	Tangential component of the mean velocity at any point inside the boundary layer

$u_a$	Propeller-induced axial velocity
$u_e$	Effective velocity profile
$u_K$	Local velocity at the tip of the wire
$u_{np}$	Propeller induced velocity normal to the surface
$u_p$	Axial velocity profiles with propeller in operation
$u_{rp}$	Circumferential average radial velocity
$u_s$	Original surface perturbation velocity
$u_{sn}$	New surface perturbation velocity as the result of cancelling $u_{np}$ on the hull
$u_{sp}$	Propeller-induced tangential velocity on the hull
$u_x$	Axial nominal velocity profiles without propeller
$u_{xh}$	Perturbation velocity at the propeller plane due to the surface source distribution of the hull
$u_{xi}$	Instantaneous velocity
$(\bar{u}'^2/U_o) \times 100$	Measured turbulence levels
$u_\xi$	Velocity correction to satisfy the conservation of vorticity
$\vec{V}$	Total velocity vector
$\vec{V}_p$	Total propeller induced velocity
$v_r$	Radial velocity
$v_{pr}$	Circumferential average radial propeller induced velocity
$v_\theta$	Circumferential velocity
$w(r)$	Nominal wake
$w_e(r)$	Effective wake
$w_T$	Taylor wake fraction
$w_\nabla$	Volume-mean wake fraction
$X$	Axial distance measured from the nose
$X_s$	Location of separation
$X_w$	Upstream matching point



$x$	Axial distance from propeller plane
$y$	Distance normal to the body surface
$\alpha$	Angle which the tangent to the body makes with the axis of the body
$\Delta C_p$	Decrease of pressure coefficient due to the propeller
$\Delta C_{\tau_0}$	Increase of local skin friction coefficient due to the propeller
$\Delta X$	Dimension of probe volume in the direction of the mean flow
$\Delta Y$	Dimension of probe volume in the direction perpendicular to the mean flow
$\Delta Z$	Dimension of probe volume in the direction of the bisector of the beam angle
$\delta$	Boundary layer thickness
$\eta$	$2r_0/D$
$\eta_B$	Propeller behind efficiency
$\eta_D$	Propulsion efficiency
$\eta_H$	Hull efficiency; $(1 - t)/(1 - w)$
$\theta$	Beam angle, ratio of lens diameter to its focal length, or angle in cylindrical coordinates
$\theta_s$	Skew angle of the propeller
$\Lambda^*$	Displacement area $= \int_0^\delta \left(1 - \frac{u}{U_e}\right) r dy$
$\lambda$	Wave length of the laser
$\nu$	Kinematic viscosity of the fluid
$\xi$	$(L - X)/L'_A$
$\rho$	Mass density of the fluid
$\tau_\omega$	Local shear stress
$\Psi$	Stream function
$\Omega$	Momentum area
$\Omega_t$	Momentum area at the tail of the body

$\Omega_0$

Far wake momentum area

$\Omega$

Vorticity

$\omega_\theta$

$\theta$ -component of vorticity

## ABSTRACT

Measurements of the boundary-layer characteristics and pressure distributions on three axisymmetric bodies with and without a propeller in operation are correlated with analytical techniques for computing (1) the interaction between the hull boundary layer flow and the potential flow and (2) the interaction between the operating propeller and the thick stern boundary layer. The agreement between the measured and computed shear stresses, pressure distributions, and velocity profiles was satisfactory except over the last 5 percent of body length on the two fullest afterbodies. An inviscid propeller-stern-boundary-layer interaction model was developed and found to give accurate predictions of effective velocity profiles. The experimental results show that the potential-flow propeller-hull interaction methods give accurate predictions for thrust deduction and the propeller-induced pressure distribution. The present analytical techniques will be useful for predicting the full-scale effective velocity profile for propeller design when account is taken of the effects of Reynolds number, roughness, and propeller suction in modifying the nominal velocity profiles.

## ADMINISTRATIVE INFORMATION

The initial experimental work reported herein was supported by the independent exploratory development program (IED) David W. Taylor Naval Ship R&D Center (DTNSRDC). Funding was provided under Element 62766N, Work Unit 1-1552-119. All subsequent experimental and analytical investigations were supported by the Naval Material Command direct laboratory funding under Element 62543N, Work Unit 1-1520-004.

## INTRODUCTION

The radius of many ship propellers is about the same order of magnitude as the thickness of the boundary layer at the propeller location. In these cases, the flow in the vicinity of the propeller is characterized by the presence of a thick and possibly separated turbulent boundary layer. An operating propeller produces an upstream suction which results in an augmentation of stern pressure drag and skin-friction drag due to the acceleration of flow. Naval architects refer to this drag increase due to propeller suction on the afterbody as thrust deduction; it is usually determined by conducting conventional resistance and self-propulsion model experiments in a towing tank.

The suction of the propeller also increases the velocity in the entire boundary-layer region. The effective inflow velocity experienced by the propeller is the result of the



interaction of the propeller and the thick stern boundary layer, and it is different from the nominal velocity distribution measured in the absence of the propeller. The nominal velocity distribution at the propeller plane of the ship model is usually measured by a standard wake rake before the actual design of the full-scale propeller is undertaken. The radial distribution of effective inflow velocity, an important input in the design of a wake-adapted propeller, is often scaled up or down from the measured circumferential-mean velocity profile by a constant factor. This factor is sometimes taken to be the ratio of the Taylor wake fraction (determined from the results of behind-condition propulsion experiments on the basis of thrust identity with propeller open-water data to the measured volume-mean nominal wake fraction). This constant-factor empirical approach can be used only as a rough approximation. Since few velocity surveys have ever been made in the presence of a propeller, the true distribution of the effective inflow velocity to the propeller has been largely unknown. The effective inflow velocity will no doubt affect propeller powering performance, cavitation characteristics, and unsteady forces and moments. It is thus important that flow fields in the presence of a propeller be investigated over a wide range of stern boundary-layer characteristics.

Thrust deduction has received the attention of many investigators,<sup>1-5</sup> and the theoretical, experimental, and empirical literature on the subject is very extensive; the many references cited by Nowacki and Sharma<sup>6</sup> have application to surface ships.

<sup>1</sup>Beveridge, J.L., "Analytical Prediction of Thrust Deduction for Submersibles and Surface Ships," *Journal of Ship Research*, Vol. 13, No. 4, pp. 258-271 (1969).

<sup>2</sup>Weinblum, G.P., "The Thrust Deduction," *Journal of American Society of Naval Engineers*, Vol. 63, pp. 363-380 (1951).

<sup>3</sup>Amtsberg, H., "Investigations on the Interaction between Hull and Propeller of Bodies of Revolution," (in German), *Jahrbuch der Schiffbautechnischen Gesellschaft*, Vol. 54, pp. 117-152 (1960); also available as David Taylor Model Basin Translation 309 (1965).

<sup>4</sup>Tsakonas, S. and W.R. Jacobs, "Potential and Viscous Parts of the Thrust Deduction and Wake Fraction for an Ellipsoid of Revolution," *Journal of Ship Research*, Vol. 4, No. 2, pp. 1-16 (1960).

<sup>5</sup>Nowacki, H., "Potential Wake and Thrust Deduction Calculations for Ship-Like Bodies," *Jahrbuch der Schiffbautechnischen Gesellschaft*, Vol. 57, pp. 330-363 (1963).

<sup>6</sup>Nowacki, H. and S.D. Sharma, "Surface Effects in Hull Propeller Interaction," *The Ninth Office of Naval Research Symposium on Naval Hydrodynamics*, Paris, France (Aug 1972); available in U.S. Government Printing Office, ACR-203, Vol. 2, pp. 1845-1961 (1972).

In contrast, literature on the interaction between a propeller and stern boundary layer is limited to isolated experimental and empirical data.<sup>7,8</sup>

The first known theoretical effort to compute the effective wake distribution from measured values of the nominal wake and static pressure distributions was made in 1972 by D.M. Nelson of the Naval Undersea Center, San Diego.\* In his unpublished work, Nelson integrated the effective wake calculation into a propeller-design computer program which has been extensively used to design propellers for small submerged bodies. Although the approach used in the present report to treat the theoretical derivation of propeller/hull interaction is independent of that used by Nelson, his numerical results did help to motivate further work on the problem. Of greatest importance, the present work represents the first time that theoretical wake predictions have been correlated with measured wake distributions in the presence of a propeller.

Axisymmetrical bodies were chosen for this investigation in order to focus on the physical nature of the complex interaction between a propeller and a thick stern boundary layer. Their geometric simplicity offers considerable experimental and computational convenience in treating the fundamental aspects of the interaction. Definitive experimental results on boundary-layer characteristics and pressure distributions for axisymmetrical afterbodies with and without propellers in operation are crucial to a better understanding of the propeller-stern interaction. Thus, much effort and care were given to the experimental equipment and procedures described here. The Laser Doppler Velocimeter was successfully used to measure velocity profiles very close to the propeller. The measured differences between the velocity profiles with and without an operating propeller provide the necessary clues to a proper understanding of the propeller/stern boundary-layer interaction.

The experimental techniques are described in detail and the results of the experiments are then used to evaluate several new analytical techniques as well as an existing one. The first of the new analytical techniques enables the pressure distribution, shear stress distribution, and velocity profiles to be determined over the entire body by considering the interaction between the boundary-layer flow next to the body and the external potential flow in the absence of a propeller. The various components of the technique are described in detail

---

<sup>7</sup>Hucho, W.-H., "On the Effect of a Stern Propeller on the Pressure Distribution and the Boundary-Layer of an Afterbody of Revolution," Institut für Strömungsmechanik der Technischen Hochschule Braunschweig, Bericht 64/45, Pt II (1965).

<sup>8</sup>Massaki Namimatsu and Moraoka Kenji, "Wake Distribution of Full Form Ships," *Engineering Review* (Japan), Vol. 7, No. 3 (1975).

\*Private communication

together with an iteration scheme for computing the interaction. The second new technique solves for the influence of the propeller on the nominal velocity distribution at the propeller disk plane in the absence of the propeller. The various assumptions used are clearly stated. One of the principal assumptions is that the interaction between the propeller and stern boundary layer may be taken to be inviscid. An existing analytical technique is evaluated for the calculation of thrust deduction where potential flow methods are used to calculate the propeller-hull interaction.

## MODELS AND EXPERIMENTAL METHODS

### BODY OF REVOLUTION MODELS

After preliminary computer evaluation of the flow characteristics of bodies of revolution, three axisymmetric afterbodies were selected for the present experimental investigation. Their afterbody length/diameter ratios ( $L_A/D$ ) were 4.308, 2.247, and 1.484; corresponding prismatic ratios ( $\tilde{C}_{pA}$ ) were respectively 0.606, 0.526, and 0.416. As shown in Figure 1 and Table 1, each afterbody was connected to a parallel middle body of length  $L_M$  and an existing streamlined forebody with a bow-entrance length/diameter ratio ( $L_E/D$ ) of 1.82. The total length of the model was fixed at a constant value of 3.066 m. Other hull particulars of the three models are listed in Table 1.

The common forebody and a portion of the parallel middle body were constructed of wood. The afterbody and the remaining portions of the parallel middle body were constructed of molded fiberglass; specified profile tolerances were held to less than  $\pm 0.4$  mm, all imperfections were removed, meridians were faired, and the fiberglass was polished to a 0.64-micron rms surface finish.

As can be seen from Figure 1, the fullnesses of the three sterns were selected to provide large variations of stern flow. Afterbody 3 ( $L_A/D = 1.484$ ) was the bluntest and had a cosine curve for the dimensionless body radius  $r_o/L$  of a form similar to that used by Kempf.<sup>9</sup>

$$\frac{r_o}{L} = 0.025886 - 0.0196736 \cos \left[ \frac{0.977137 - X/L}{0.112326} \pi \right]$$

for  $0.864811 \leq X/L \leq 0.977137$ . This afterbody had an inflection point at  $X/L = 0.920974$ .

<sup>9</sup>Kempf, G., "Wirbelablosung bei Volligen Schiffsformen," Schiff und Hafen, Vol. 6, No. 7, pp. 407-408 (1954).



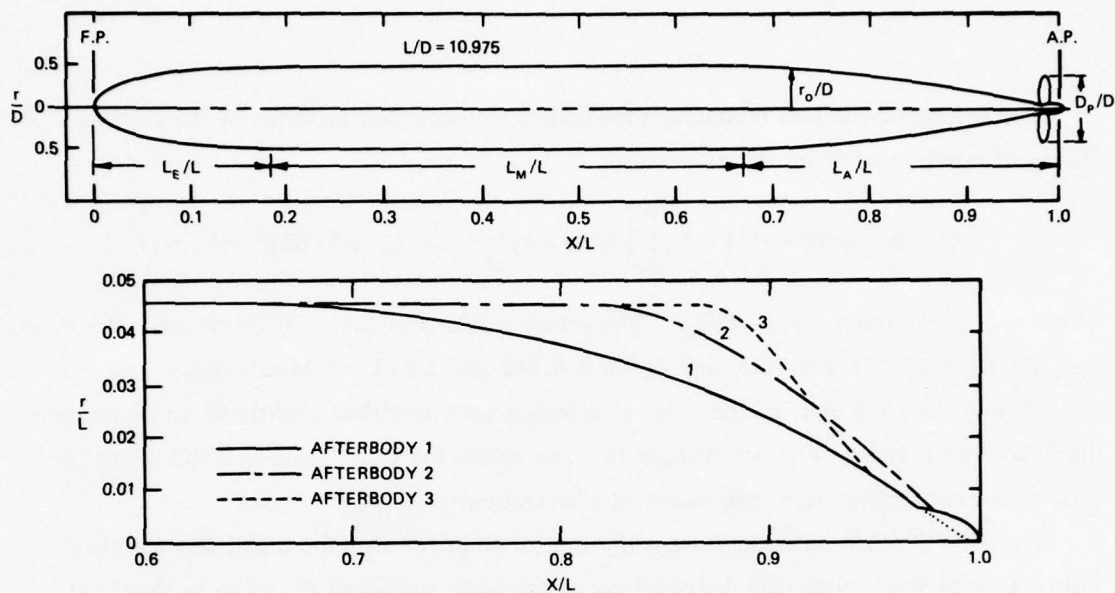


Figure 1 – The Axisymmetric Afterbodies

TABLE 1 – HULL PARTICULARS  
FOR AXISYMMETRIC AFTERBODIES

Model	Afterbody 1	Afterbody 2	Afterbody 3
$L_E/D$	1.8182	1.8182	1.8182
$L_M/D$	4.8485	6.9091	7.6727
$L_A/D$	4.3078	2.2472	1.4836
$\tilde{C}_{PE}$	0.646	0.646	0.646
$\tilde{C}_{PA}$	0.606	0.526	0.416
$\tilde{C}_P$	0.787	0.844	0.862
$\pi D^2/4L^2$	0.006521	0.006521	0.006521
$\pi D^2/4S$	0.02675	0.02560	0.02540
$\nabla^{2/3}/S$	0.122	0.122	0.123
$L/D$	10.9745	10.9745	10.9745
$S(M^2)$	2.291	2.395	2.408
$L(M)$	3.066	3.066	3.066

The offsets of the two remaining afterbodies are described in terms of the Granville family of polynomials<sup>10</sup> by the expression

$$\eta^2 = S_1^2 [\xi^2 (\xi - 1)^4] + \tilde{K}_1 \left[ \frac{1}{3} \xi^3 (\xi - 1)^3 \right] + 1 - (\xi - 1)^4 (10 \xi^2 + 4 \xi + 1)$$

where  $\eta = 2r_o/D$  and  $\xi = (L - X)/L'_A$ . The selected values of the coefficients were  $S_1^2 = 7.9254$  and 3.4,  $\tilde{K}_1 = 17.281$  and 32.5, and  $L'_A/D = 4.242$  and 1.812 for Afterbodies 1 and 2, respectively. The tail ends of the three afterbodies were modified slightly to accommodate the hub of an existing propeller (Figure 1). The values for  $L_A/D$  given in Table 1 are the final values corresponding to the modified afterbodies.

The Hess-Smith<sup>11</sup> potential-flow computer program for an unbounded incompressible fluid was used to calculate the distributions of pressure coefficient  $C_p = (p - p_o)/(1/2)\rho U_o^2$  on the three afterbodies; see Figure 2. As would be expected, the magnitudes of the stern negative pressure troughs and the subsequent adverse pressure gradients increased dramatically with increasing afterbody fullness, i.e., decreasing  $L_A/D$ . Preliminary boundary-layer calculations<sup>12,13</sup> used as input the potential flow velocity up to  $X/L = 0.95$  and linear extrapolation of potential flow velocity between  $0.95 \leq X/L \leq 1$ ; these indicated that the three afterbodies would provide three different types of stern flow. It was predicted that Afterbody 3 would have strong shoulder separation at about  $X/L = 0.92$ , Afterbody 2 would have incipient separation or nearly separated flow further aft, and Afterbody 1 would not have separation. In a more refined calculation of the thick stern boundary-layer flow, the potential flow velocities, (based on pressure distributions iterated from consideration of the boundary-layer and wake displacement thicknesses) indicated that Afterbody 2 would not have separation.\* Thus, the three afterbodies provided a wide range of stern flow for the investigation of the propeller/stern boundary-layer interaction.

<sup>10</sup>Granville, P.S., "Geometrical Characteristics of Noses and Tails for Parallel Middle Bodies," NSRDC Report 3763 (1972).

<sup>11</sup>Hess, J.L. and A.M.O. Smith, "Calculation of Potential Flow about Arbitrary Bodies," in "Progress in Aeronautical Sciences," Vol. 8, Pergamon Press, New York (1966), Chapter 1.

<sup>12</sup>Kerney, K.P. and N.M. White, "Description and Evaluation of a Digital-Computer Program for Calculating the Viscous Drag of Bodies of Revolution," DTNSRDC Report 4641 (1975).

<sup>13</sup>Cebeci, T. and A.M.O. Smith, "Analysis of Turbulent Boundary Layers," Academic Press, New York (1974), pp. 329 - 384.

\*Experimental results, which will be discussed in detail later, confirmed that Afterbody 3 had shoulder separation at  $X/L = 0.918$  and that Afterbodies 1 and 2 had no separation.

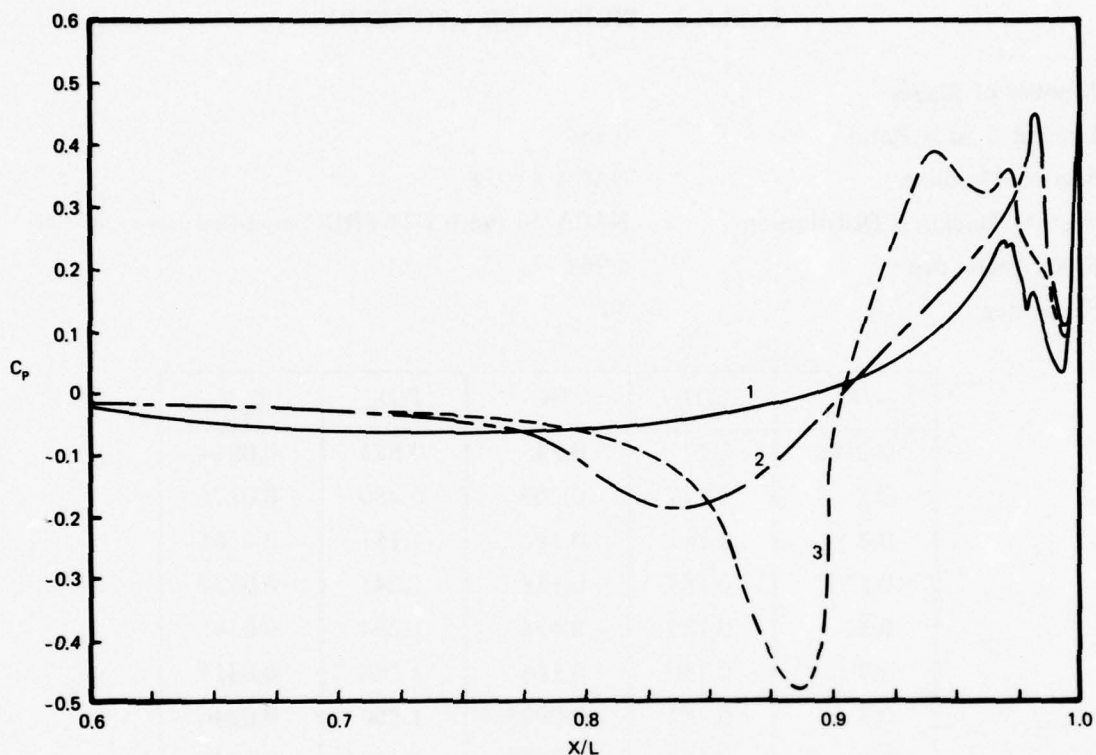


Figure 2 – Computed Distributions of Pressure Coefficient on the Axisymmetric Afterbodies

### MODEL PROPELLER

An existing seven-bladed propeller, with a diameter of 54.5 percent of the hull diameter, was located at  $X/L = 0.983$  for the experimental investigation of propeller and stern boundary-layer interaction. Table 2 summarizes the propeller geometry. This propeller was designed for a wake distribution which was different from the wakes generated by the three afterbodies. Thus, an inverse propeller computing program was required to calculate the hydrodynamic characteristics of the propeller with the given propeller geometry and the specified wake distribution. This calculation procedure will be given later in the report.



TABLE 2 - PROPELLER GEOMETRY

Number of Blades	7
Expanded Area Ratio	0.584
Section Meanline	NACA $a = 0.8$
Section Thickness Distribution	NACA 66 (with DTNSRDC modified nose and tail)
Rake Angle, deg	6.964
Skew, deg	30

$r/R_p$	$C/D_p$	$t/C$	$P/D_p$	$f_M/C$
0.2106	0.171	0.235	0.823	0.0014
0.3	0.177	0.209	0.980	0.0175
0.4	0.182	0.182	1.151	0.0288
0.5	0.185	0.158	1.243	0.0337
0.6	0.185	0.135	1.264	0.0341
0.7	0.180	0.116	1.248	0.0311
0.8	0.164	0.0995	1.206	0.0246
0.9	0.132	0.0875	1.157	0.0141
1.00	0.069	0.0813	1.108	0.

## EXPERIMENTAL TECHNIQUE

The experimental investigation was conducted in the wind tunnel of the DTNSRDC anechoic flow facility. The wind tunnel has a 2.438- by 2.438-m test section with a maximum air speed of 61 m/s. Air is circulated around a closed loop and passes through a closed-jet test section into an open-jet anechoic chamber. With a model in place, the free-stream turbulence level in the test section was measured by a DISA 55M series, constant-temperature anemometer with linearizer. The diameter of the tungsten wire used was 0.0006 mm. The measured turbulence levels ( $\sqrt{\bar{u}'^2}/U_0$ )  $\times 100$  were 0.075, 0.090, 0.100, and from 0.12 to 0.15 for free-stream velocities  $U_0$  of 24.4, 30.5, 38.1, and 45.7 m/s, respectively. Integration of the measured noise spectrum levels in the test section from 0 to 10,000 Hz indicated that the typical background acoustic noise at 30.5 m/s was around 93 dB re 0.0002 dyn/cm<sup>2</sup>. These levels of ambient turbulence and acoustic noises were considered low enough so as not to unfavorably affect the measurements of boundary-layer characteristics.

The model was supported by two streamlined struts separated by roughly one-third of the model length. The upstream strut had a 15-cm chord and the downstream strut a 3-cm

chord. The disturbances generated by the supporting struts were within the region below the horizontal centerplane. Prior to the experiment, pressure taps and Preston tubes were used to check the axisymmetrical characteristics of the stern flow at  $X/L = 0.90, 0.95$ , and  $0.977$ . The circumferential variations of pressure and surface shear stress on the upper half of the body at these three locations were within two percent. All the measurements were made in the vertical centerplane along the upper meridian and there was little extraneous effect from the supporting strut. Each stern protruded from the closed-jet working section of the wind tunnel into the anechoic chamber ( $6.4 \times 6.4 \times 6.4$  m) located upstream of the diffuser. The propeller was driven by a 9-kW high-speed motor mounted inside the stern of the model. The rate of revolution of the propeller shaft was measured by a magnetic pickup and displayed by a digital counter.

Measurements of surface shear stress, surface pressure distribution, and boundary-layer axial velocity distribution were made on each stern first without a propeller and then with a propeller operating at one or two advance coefficients. The following equipment was used. A 1.83-mm Preston tube was taped to the sterns at successively further aft locations in order to measure shear stress at 12 locations along the upper meridian of each stern. (The tube has been calibrated in a 2.54-cm water pipe flow facility described by Huang and von Kerczek.<sup>14</sup>) Because a logarithmic boundary-layer velocity profile is required in order to analyze Preston tube data, shear stresses could not be accurately determined by this method at locations downstream of separation. Pressure taps (0.8-mm diameter) were used to measure steady pressure at the same locations as the Preston tubes. The holes were connected by "Tygon" plastic tubing to a scanning valve and then to a strain-gage type pressure transducer located underneath the floor of the closed-jet test section. The pressure transducer (ACEC Model 310) was used in conjunction with a signal conditioner (Endevco 4470), an amplifier (Dana Model 2856), and a digital voltmeter to measure the pressure from Preston tubes and surface pressure taps. An automatic control for the scanning valve was located outside the wind tunnel.

Steady boundary-layer axial velocity profiles were measured by a laser Doppler velocimeter (LDV) at five stations on each stern. The LDV was located on an optical bench in the quiescent region of the anechoic chamber and was operated in a dual-beam off-axis backscatter mode, which is described in detail in the appendix. Figure 3 shows photographic views of the optical arrangements for two of the models.

<sup>14</sup>Huang, T.T. and C.H. von Kerczek, "Shear Stress and Pressure Distribution on a Surface Ship Model: Theory and Experiment," The Ninth Office of Naval Research Symposium on Naval Hydrodynamics, Paris, France (Aug 1972); available in U.S. Government Printing Office, ACR-203, Vol. 2, pp. 1963 - 2010 (1972).

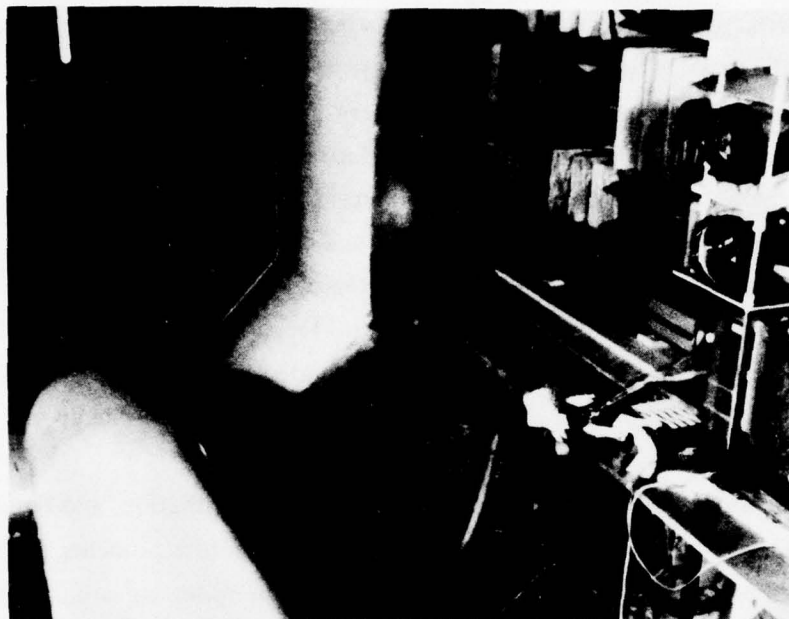


Figure 3a - With Afterbody 2

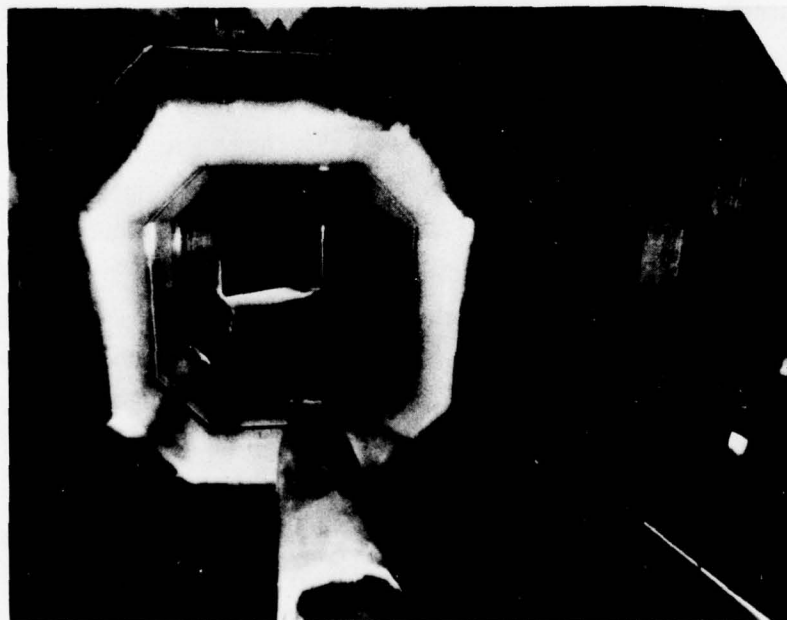


Figure 3b - With Afterbody 3

Figure 3 - Optical Arrangement of Laser Doppler Velocimeter  
in the Wind Tunnel of the Anechoic Facility



The focal length of the LDV optics was 1.5 m and the total beam angle was 3.722 deg. The effective probe volume of this off-axis backscatter optics was roughly ellipsoidal, with dimensions of about 0.5 x 5 mm, and the probe volume could be focused in the stern boundary layer at distances down to 2 mm from the hull surface.

A detailed analysis of the accuracy of the measurements has not been made. However, the standard deviations of the measured data can be estimated from repeat runs. The standard deviations of the measured static wall pressure and shear stress were about 5 percent of their mean values and the standard deviations of the measured velocities were about 2 percent of the free-stream velocity.

## METHOD FOR CALCULATING POTENTIAL-FLOW-BOUNDARY-LAYER INTERACTION

### SURVEY OF PREVIOUS METHODS

Several studies have recently attempted to calculate the complete pressure field acting on axisymmetric bodies, including the effects of viscosity. They generally start with an initial estimate of the pressure distribution, usually the potential flow distribution with some modifications in the tail region, and employ standard boundary-layer theory to calculate the flow over the forward region of the body. The boundary-layer equations may be in either integral or differential form. These methods differ greatly, however, in the approach used to calculate the flow field at the stern of the body (where the boundary layer may be thick), in the near wake region, and in the far wake region. These differences will be pointed out below. The initial flow calculations are then used to modify the geometry of the body and wake, usually by adding the local displacement thickness as suggested by Lighthill.<sup>15</sup> Potential-flow methods are then utilized to compute the pressure distribution around the modified body. Flow calculations are repeated for the new pressure distribution, and this basic scheme is continued until the pressure distributions from two successive approximations agree to within a given error criterion.

The modeling of the flow over the stern of the body and in the wake region ranges from very simple to very complex. Perhaps the simplest modeling is by Beatty.<sup>16</sup> He merely adds the displacement thickness calculated by the Douglas CS differential boundary-layer

<sup>15</sup> Lighthill, M.J., "On Displacement Thickness," *Journal of Fluid Mechanics*, Vol. 4, Pt 4, pp. 383-392 (1958).

<sup>16</sup> Beatty, T.D., "A Theoretical Method for the Analysis and Design of Axisymmetric Bodies," *National Aeronautics and Space Administration CR-2498* (1975).

method<sup>13,17</sup> to the body up to the trailing edge. He then calculates the potential flow distribution about the resulting open-ended body and a semi-infinite stream tube (which leaves the trailing edge of the open body and proceeds downstream) until the cross section of the stream tube approaches a constant value far downstream. In the case of separated flow, the portion of the displaced body from the separation point to the trailing edge is assumed to be an open-ended cylinder with radius equal to the radius of the original body plus the displacement thickness at the separation point. A circular arc is used to fair the displaced body ahead of the separation point into the cylindrical body. Agreement is good with experimental results for the case of a streamlined body with fineness ratio 12:1, but it is only fair for the case of a sphere at a subcritical Reynolds number.

Beveridge<sup>18</sup> considers a generally similar model but allows the wake to extend to infinity. However, he does not specify such details as how the body is faired into the wake and the width of the wake at infinity. Agreement of this method is relatively poor with experimental results for a Series 58 body with fineness ratio 10.

In a general method outlined by Cebeci, Mosinskis, and Smith<sup>17</sup> for adding the displacement thickness to the original body, the modeling of the wake is left unspecified. The difference between the potential flow and viscous pressure distributions is shown for a few cases, but no comparisons with experiment are given.

The Myring<sup>19</sup> method is somewhat more complex. He uses boundary-layer equations in integral form to solve for the flow on the body and in the wake. The principal difference between the equations for the two flow regions lies in the form for the entrainment coefficient which is larger in the far wake because of increased turbulent mixing. In the region close to the tail of the body, the entrainment coefficient appropriate to the body is faired into the corresponding coefficient for the far wake by means of an exponential function. However, an important constant in the fairing function is unspecified and must be determined by comparison with available experimental data.

---

<sup>17</sup>Cebeci, T. et al., "Calculation of Viscous Drag and Turbulent Boundary-Layer Separation on Two-Dimensional and Axisymmetric Bodies in Incompressible Flows," Douglas Aircraft Report MDC J0973-01 (1970).

<sup>18</sup>Beveridge, J.L., "Pressure Distribution on Towed and Propelled Streamlined Bodies of Revolution at Deep Submergence," David Taylor Model Basin Report 1665 (1966).

<sup>19</sup>Myring, D.F., "The Profile Drag of Bodies of Revolution in Subsonic Axisymmetric Flow," Royal Aircraft Establishment (Great Britain) Technical Report 72234 (1972).

The computed pressure distributions agree well with experimental results for the Lyon body<sup>20,21</sup> and the airship AKRON.<sup>22</sup>

Nakayama<sup>23</sup> considers an even more complex model. He uses standard boundary-layer equations in integral form to model the flow over the forward portion of the body and in the far wake. A significant difference between this model and those previously mentioned is that in the region near the tail and in the near wake, allowance is made for the transverse variation of pressure across the boundary layer. Also, a simple linear profile is assumed for the normal velocity. Another significant difference is that the displacement thickness, which is an integrated effect of the boundary layer, is not used to modify the body. Instead, the potential solution is matched to the boundary layer calculations at the edge of the boundary layer and wake. The computed pressure distributions are in good agreement with experimental results for the case of the Lyon body,<sup>20,21</sup> but in only fair agreement for the case of a modified spheroid.<sup>24</sup>

Perhaps the most complex method outside of a complete solution of the Navier-Stokes equations in the entire flow field is that considered by Brune, Rubbert, and Forester.<sup>25</sup> This method may be best described by referring to their sample case of a 4:1 prolate ellipsoid. Standard boundary-layer equations in differential form are used to calculate the flow over the front half of the body,  $0 \leq X/L \leq 0.5$ , where  $X$  is the axial distance measured from the nose and  $L$  is the total length of the body. The complete Navier-Stokes equations were used to calculate the flow over the rear half of the body and in the near wake,  $0.5 \leq X/L \leq 1.26$ . The shape of the displacement tail for  $X/L \geq 1.26$  is taken to be a faired shape which ends in a point at  $X/L = 2.5$ . The authors give no precise method for obtaining this displacement tail but simply state that it is specified by "extrapolation." No comparisons with experimental results are given. It is worthwhile to note that use of the Navier-Stokes equations greatly

<sup>20</sup> Lyon, H.M., "Effect of Turbulence on Drag of Airship Models," Aeronautical Research Committee (Great Britain) Reports and Memoranda 1511 (1932).

<sup>21</sup> Lyon, H.M., "A Study of the Flow in the Boundary Layer of Streamlined Bodies," Aeronautical Research Committee Reports and Memoranda 1622 (1934).

<sup>22</sup> Freeman, H.B., "Pressure Distribution Measurements on the Hull and Fins of a 1/40-Scale Model of the US Airship 'Akron'," National Advisory Committee for Aeronautics Report 443 (1932).

<sup>23</sup> Nakayama, A., "Viscid-Inviscid Interaction Due to the Thick Boundary Layer near the Tail of a Body of Revolution," Ph.D. Thesis, University of Iowa (1974).

<sup>24</sup> Patel, V.C. et al., "Measurements in the Thick Axisymmetric Turbulent Boundary Layer near the Tail of a Body of Revolution," Journal of Fluid Mechanics, Vol. 63, Pt 2, pp. 345-367 (1974).

<sup>25</sup> Brune, G.W. et al., "The Analysis of Flow Fields with Separation by Numerical Matching," Symposium on Flow Separation, Advisory Group for Aerospace Research and Development, Germany (1975).



increases the overall computer time requirements of the method. The authors state that the laminar boundary layer and potential flow calculations require about 40 sec of CDC-6600 time per iteration whereas the Navier-Stokes equations require approximately 40 min per iteration. This method is limited to laminar flow. The extension to turbulent flow would, of course, require even more computer time.

## PRESENT ITERATION SCHEME

### Outline of the Present Scheme

The Douglas CS differential<sup>13,17</sup> boundary-layer method is used to calculate the flow over the body, and the integral wake relations given by Granville<sup>26</sup> are used to calculate the flow in the wake. The calculated displacement thicknesses are then utilized to generate an overall body-wake displacement model. However, since neither of the two methods properly models the thick boundary layer in the stern/near-wake region, where there may be sizeable pressure variations across the boundary layer, the calculated displacement body is not assumed to be valid in the region  $0.95 \leq X/L \leq 1.05$ . Instead, a fifth-degree polynomial is used in this region, with the six constants determined by requiring the thickness, slope, and curvature to be equal to those calculated at  $X/L = 0.95$  and  $1.05$ . Should separation occur before  $X/L = 0.95$ , the upstream matching point is moved to the separation point. The pressure distribution over the displacement body is calculated by the Douglas-Neumann method.<sup>11,27</sup> The resulting pressure distribution is then used to calculate the new viscous flow over the body and in the wake. This process is repeated until two successive pressure distributions agree to within a specified error criterion everywhere in the flow field.

The potential-flow pressure distribution over the body, without a displacement thickness correction, constitutes the first iteration except that the velocity ratio is linearly extrapolated over the last 5 percent of body length. In the wake, the velocity ratio is initially taken to increase exponentially from the value at the tail to 1 in the far wake.

Since the Douglas-Neumann method and the Douglas CS differential boundary-layer method are widely used to calculate flows around axisymmetric bodies, only brief descriptions are given here. Other aspects of the method are described in greater detail.

<sup>26</sup>Granville, P.S., "The Calculation of the Viscous Drag of Bodies of Revolution," David Taylor Model Basin Report 849 (1953).

<sup>27</sup>Smith, A.M.O. and J. Pierce, "Exact Solution of the Neumann Problem. Calculation of Non-Circulatory Plane and Axially Symmetrical Flows About or Within Arbitrary Boundaries," Douglas Aircraft Report ES-26988 (1958).

### Douglas-Neumann Computer Program

In this method,<sup>11,27</sup> the Laplace equation for the unknown potential is converted into a Fredholm integral equation of the second kind for the unknown source density distribution on the surface of the body. The body is considered as composed of a series of frustums of cones, and the integral equation is converted to a set of algebraic equations for the unknown constant source density on the surface of each frustum. Once the source densities have been obtained, it is a simple matter to obtain all flow variables of interest.

The original computer program included several options for solving the algebraic equations. For the number of points typically used in the present calculations (about 140 on the body and 35 in the wake), the Seidel iterative procedure is the most economical.

### Douglas CS Differential Boundary-Layer Method

This method<sup>13,17</sup> solves the boundary-layer equations in partial differential equation form. Thus, no assumptions are made about the form of the velocity profiles. The method also accounts for the effects of transverse curvature, which are important in the tail region where the thickness of the boundary layer may be greater than the body radius. However, the pressure variation across the boundary layer, which may be appreciable in the tail region, is neglected. The equations are solved by the Keller box method<sup>13</sup> which essentially consists of first reducing the original set of second-order partial differential equations to a first-order system and then solving the resulting set by an implicit finite difference method.

The location of transition from laminar to turbulent flow may be specified. In the experimental work described here, a 0.61-mm-diameter trip wire was used at an X/L location of 5 percent. The Granville<sup>26</sup> boundary-layer computation method programmed by Kerney and White<sup>12</sup> is used to compute the laminar boundary layer upstream of the trip wire and the turbulent boundary layer downstream of the trip wire. The jump in momentum thickness Reynolds number  $\Delta R_\theta$  due to the parasitic drag of the wire is specified according to McCarthy, Power, and Huang<sup>28</sup> by

$$\Delta R_\theta = \frac{C_D}{2} \left( \frac{u_K}{U_e} \right) \frac{u_K K}{\nu}$$

<sup>28</sup> McCarthy, J.H. et al., "The Roles of Transition, Laminar Separation, and Turbulence Stimulation in the Analysis of Axisymmetric Body Drag," The Eleventh Office of Naval Research Symposium on Naval Hydrodynamics, London, England (1976).

Here  $u_k$  is the local velocity at the tip of the wire,  $U_e$  is the potential flow velocity at the trip location,  $K$  is the diameter of the wire (0.61 mm), and  $C_D$  is the drag coefficient of the wire (taken as 0.75).

When the flow was probed with a hot wire, the trip wire was found to effectively trip the flow at 1 cm downstream from the wire. Because of the finite parasitic drag of the wire, the boundary layer can be considered to become turbulent at a virtual origin upstream of the trip wire. This virtual origin for the turbulent flow is defined such that the sum of the laminar frictional drag from the nose to the trip, the parasitic drag of the trip, and the turbulent frictional drag after the trip equals the sum of the laminar frictional drag from the nose to the virtual origin and the turbulent frictional drag from the virtual origin to the after end of the model.<sup>28</sup> As can be seen from Figure 4, the virtual origin can be obtained by finding the intersection of lines L and T (plotted as  $r_o R_\theta / r_{max}$  versus  $X/L$ , where  $r_o$  is the model local radius and  $r_{max}$  is the maximum radius of the body). Line L is valid for the axisymmetrical laminar boundary layer and line T is valid for the axisymmetrical turbulent boundary layer with a jump of  $\Delta R_\theta$  above Line L at the trip location. The magnitude of the jump  $\Delta R_\theta$  is related to the parasitic drag of the trip wire.<sup>28</sup> The location of transition in the mathematical model for the present boundary-layer calculation is specified at the virtual origin. The initial value of  $R_\theta$  at the virtual origin for turbulent boundary-layer computation is then equal to the laminar value of  $R_\theta$  (Line L) at the virtual origin.

### The Granville Wake Relations

The differential momentum equation for wake flow is simply the boundary-layer equation with skin friction neglected<sup>26</sup>

$$\frac{d\Omega}{dX} + (h + 2) \frac{\Omega}{U_e} \frac{dU_e}{dX} = 0 \quad (1)$$

$$\text{where } \Omega = \text{momentum area} = \int_0^\delta \left(1 - \frac{u}{U_e}\right) \frac{u}{U_e} r \, dy \quad (2)$$

$\delta$  = boundary-layer thickness

$u$  = tangential component of the mean fluid velocity at any point inside the boundary layer

$U_e$  = computed potential flow velocity at the boundary of the displacement body representing the wake

$r$  = radial distance measured from the body axis

$y$  = distance normal to the body surface



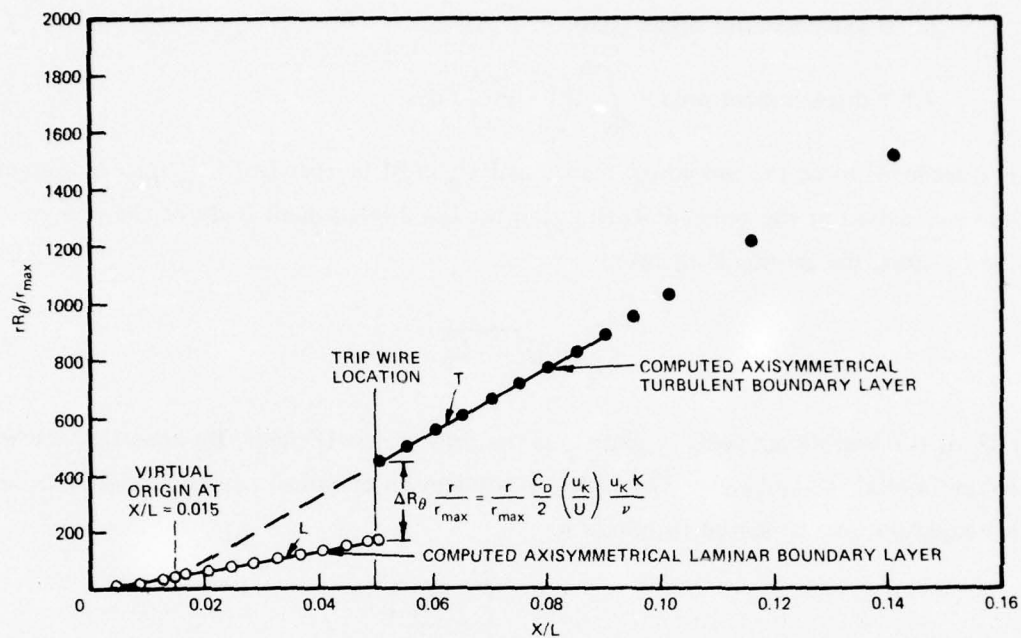


Figure 4a -  $R_n = 5.9 \times 10^6$

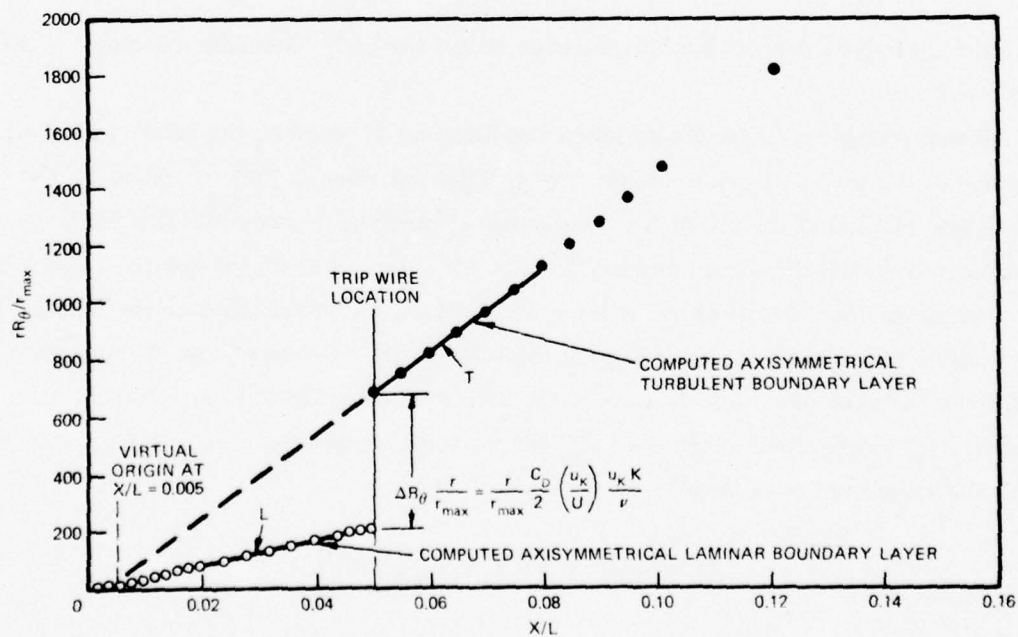


Figure 4b -  $R_n = 8.8 \times 10^6$

Figure 4 - Determination of Virtual Origin of Axisymmetrical Turbulent Boundary Layer behind a Trip Wire

$$h = \text{axisymmetric shape factor} = \Lambda^*/\Omega \quad (3)$$

$$\Lambda^* = \text{displacement area} = \int_0^\delta \left(1 - \frac{u}{U_e}\right) r \, dy \quad (4)$$

If  $\Omega$  is considered to be the unknown, then  $h$  and  $U_e$  must be specified.  $U_e$  may be obtained from the calculation of the pressure distribution for the displacement body of the previous iteration by using the Bernoulli equation

$$\frac{U_e}{U_o} = \sqrt{1 - C_p} \quad (5)$$

where  $U_o$  is the free-stream velocity and  $C_p$  is the pressure coefficient. By analyzing the wake data behind a Mark 13 torpedo,<sup>29</sup> Granville<sup>26</sup> postulates an empirical equation relating  $U_e$  and  $h$ . This equation may be solved to obtain  $h$

$$h = 1 + (h_t - 1) \left[ \frac{\ln \frac{U_o}{U_e}}{\ln \frac{U_o}{U_t}} \right]^{1/q} \quad (6)$$

where the subscript  $t$  denotes conditions at the tail of the body; Granville recommends the value  $q = 7$ .

All that remains is to specify an initial condition for  $\Omega$ , namely, the value of  $\Omega$  at the beginning of the wake. It would be incorrect to take this value as that computed by the Douglas CS method at the tail of the body since, as mentioned previously, this method does not accurately model the thick boundary layer at the stern. Instead, the approach taken is first to compute the value of  $\Omega$  in the far wake based on the calculated drag coefficient. This may be done by equating the total drag on the body to the net rate of loss of momentum of the flow in the axial direction. In view of the definition given for  $\Omega$  in Equation (2), this equation may be expressed in terms of  $\Omega_o$ , the far wake momentum area, and  $C_{DFA}$ , the drag coefficient based on frontal area<sup>26</sup>:

$$2\pi \Omega_o \rho U_o^2 = \pi r_{\max}^2 C_{DFA} \frac{1}{2} \rho U_o^2 \quad (7)$$

or

<sup>29</sup>Eggers, H.A., "Wake Survey of the Mark 13 Torpedo," David Taylor Model Basin Report 583 (1947).

$$\Omega_0 = \frac{C_{DFA} r_{\max}^2}{4} \quad (8)$$

where  $r_{\max}$  is the maximum radius of the body. From Equations (1) and (6), Granville<sup>26</sup> derives the following equation for  $\Omega_t$  in terms of  $\Omega_0$

$$\Omega_t = \frac{\Omega_0}{\left(\frac{U_t}{U_0}\right) \frac{(h_t + 2)q + 3}{1 + q}} \quad (9)$$

$\Omega_t$  is then the initial value of  $\Omega$  required to start the integration of Equation (1).

#### Modeling of Displacement Body

The computed effective displacement thickness  $a^*$  is added to the body for  $X/L \leq X_w/L$ , where  $X_w$  is the upstream matching point, i.e., the smaller of the values 0.95 or the location of separation  $X_s$ . The value of  $a^*$  is related to the displacement area  $\Lambda^*$  by<sup>26</sup>

$$a^* = \frac{-r_0 + \sqrt{r_0^2 + 2\Lambda^* \cos \alpha}}{\cos \alpha} \quad (10)$$

where  $r_0$  is the radius of the body and  $\alpha$  is the angle which the tangent to the body makes with the axis of the body. In the far wake, where  $r_0 = \alpha = 0$ ,  $a^*$  is simply given by

$$a^* = \sqrt{2\Lambda^*} \quad (11)$$

Although the displacement wake should theoretically be infinite in length, it is typically terminated at  $X/L = 30$  in the present calculations for the sake of computational convenience. At this point, the value of  $\Omega$  usually agrees with the value of  $\Omega_0$  given in Equation (8) to three significant figures. The tail of the displacement wake is left open so that the flow leaves parallel to the tail. This is considered preferable to having a blunt end where the flow must turn around a sharp corner, thus causing a jump in the local pressure coefficient.

For  $X_w/L \leq X/L \leq 1.05$ , where neither the thin boundary layer nor far wake assumptions are valid, a fifth-degree polynomial is used to represent the displacement body. The six constants of the polynomial are adjusted to obtain continuity of displacement, slope, and curvature at the upstream and downstream matching points.



### Convergence Behavior

In an earlier displacement model used in the present investigation, only continuity of displacement and slope were enforced at the matching points. The computed values of  $C_p$  at both matching points showed large local jumps. With the addition of continuity of curvature, the pressure distribution for a particular iteration became smooth. However, it was found that the convergence near the matching points was substantially slower than anywhere else on the displacement body. This is because the requirements on slope and curvature, which are derivatives of the displacement, tend to accentuate the differences between the displacement bodies of two successive iterations.

As typical examples, Figure 5 shows the values of  $C_p$  at the upstream and downstream matching points and Table 3 shows the values of  $C_p$  at other points on the body for each successive iteration for Afterbody 1 at a Reynolds number of  $5.88 \times 10^6$ .

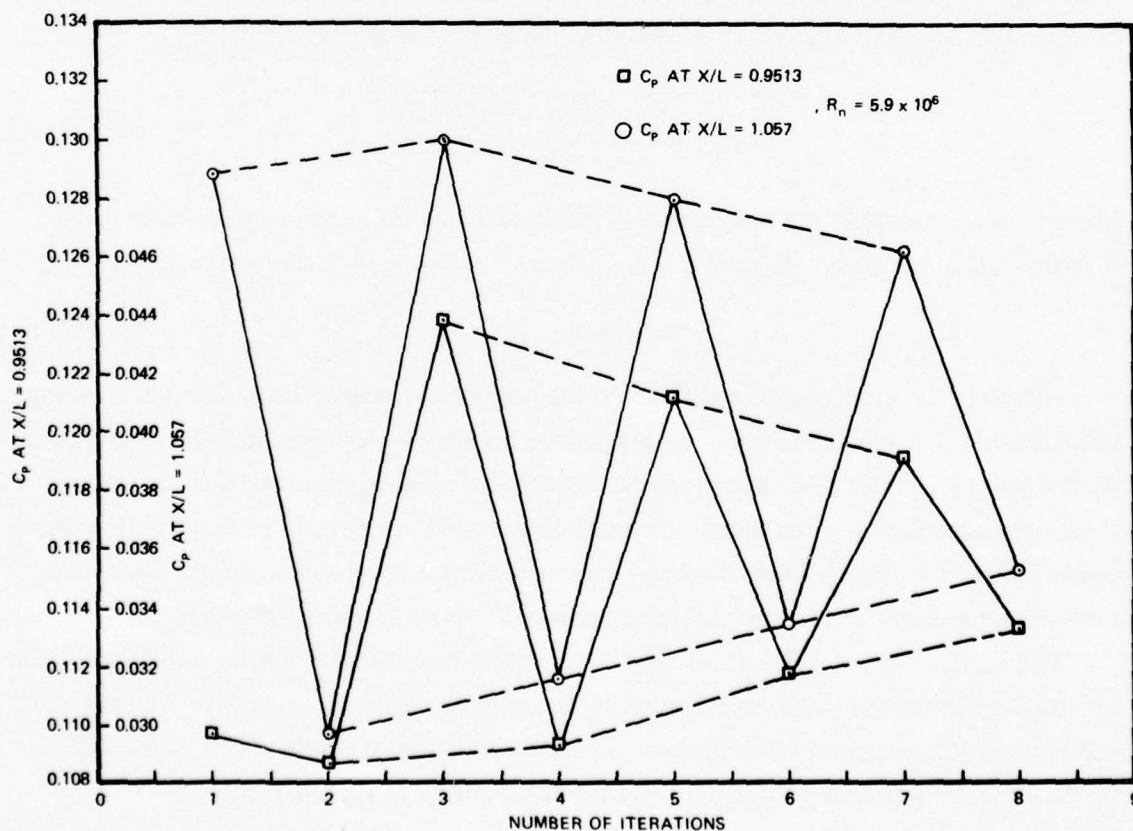


Figure 5 – Convergence Characteristics of Boundary-Layer and Potential-Flow Iteration Scheme

In this figure, Iteration  $n$  refers to the pressure distribution for the  $n$ th displacement body (Iteration 0, not shown in the figure, would refer to the potential flow pressure distribution over the original body). Figure 5 indicates that the  $C_p$ 's converge slowly to a mean value which is approximately the arithmetic average of two successive iterations. Even after eight iterations, the  $C_p$ 's at the upstream matching point have not quite converged to within a 0.01 error. On the other hand,  $C_p$ 's elsewhere in the flow field usually converge to 0.01 after the third iteration.

**TABLE 3 – CONVERGENCE CHARACTERISTICS OF THE BOUNDARY-LAYER AND POTENTIAL FLOW ITERATION SCHEME**

No. of Iteration	Value of $C_p$ at Various $X/L$					
	0.9106	0.9390	0.9538	0.9652	0.974	0.986
1	0.525	0.1123	0.1296	0.1310	0.1234	0.1016
2	0.0358	0.0729	0.0999	0.1236	0.1350	0.1389
3	0.0357	0.0977	0.1268	0.1366	0.1354	0.1225
4	0.0407	0.0834	0.1041	0.1229	0.1306	0.1299
5	0.0349	0.0910	0.1280	0.1364	0.1375	0.1273
6	0.0399	0.0882	0.1075	0.1231	0.1288	0.1263
7	0.0360	0.0874	0.1201	0.1361	0.1390	0.1302
8	0.0388	0.0910	0.1107	0.1233	0.1275	0.1238

In view of the above, most of the numerical results presented in this report are based on three iterations. The pressure distribution used to make the final boundary-layer calculations is taken to be the arithmetic average of the  $C_p$ 's from Iterations 2 and 3.

#### Calculation of Output Variables

In addition to the pressure distribution, several other variables of interest are calculated at each station along the body. These include most of the boundary-layer variables calculated in the original Douglas CS program.<sup>30</sup> The original output has been expanded significantly in two areas.

<sup>30</sup>Cebeci, T. et al., "A Finite-Difference Method for Calculating Compressible Laminar and Turbulent Boundary Layers," Douglas Aircraft Report DAC-67131 (1969).

First, whereas the original program printed out only the tangential velocity profile, the present program also prints out the normal, axial, and radial velocity profiles. Wake distributions in the propeller disk plane are usually given in terms of the latter two profiles.

Second, the total drag coefficient of the body is computed by three separate methods. The first employs the Squire-Young formula as given in Cebeci et al.<sup>17</sup>

$$C_{DSY} = \frac{4\pi\Omega_t}{A} \left( \frac{U_t}{U_o} \right)^{(h_t + 5)/2} \quad (12)$$

where A is the reference area. The second method uses the Granville formula as given in Cebeci et al.<sup>17</sup>

$$C_{DG} = \frac{4\pi\Omega_t}{A} \left( \frac{U_t}{U_o} \right)^{[7(h_t + 2) + 3]/8} \quad (13)$$

The third method considers the total drag coefficient as the sum of the total skin friction coefficient  $C_F$  and the pressure drag  $C_{pv}$

$$C_T = C_F + C_{pv} \quad (14)$$

where  $C_F$  is given by<sup>17</sup>

$$C_F = \frac{2\pi}{A} \int_0^L c_f r_o \left( \frac{U_e}{U_o} \right)^2 dx \quad (15)$$

Here  $c_f$  is the local skin friction coefficient  $= \tau_\omega / \frac{1}{2} \rho U_e^2$  and  $\tau_\omega$  is the local shear stress.

At first, the pressure drag  $C_{pv}$  was obtained by integrating the final viscous pressure distribution around the body (usually the arithmetic average of the  $C_p$ 's from the second and third iterations). As a check on this method, it was decided to also integrate the original potential flow pressure distribution around the body. It was found that this did not give the theoretically predicted zero pressure drag and often resulted in a value of the same order of magnitude as the viscous pressure drag. A closer inspection of the detailed output revealed that the contributions to the total drag from the first few stations near the nose were of the same order of magnitude as the final integrated pressure drag. In view of this, some of the bodies were rerun with a finer grid in the nose region. Also, an integration method of higher accuracy, Simpson's rule, was used instead of the simpler trapezoidal rule. Although these changes usually produced large changes in the computed potential flow drag, the resulting values were not necessarily closer to the theoretically predicted value of zero. It became clear



that a prohibitively large number of points near the nose would be required to obtain numerically the theoretically predicted value of zero for the potential flow pressure drag.

Since the numerical inaccuracy in the computed pressure drag was largely because of the pressure distribution near the nose, which is essentially not affected by viscosity, it was decided to compute the viscous pressure drag  $C_{pv}$  by integrating  $\Delta C_{pv}$  around the body, where

$$\Delta C_{pv} = C_{pvf} - C_{pp} \quad (16)$$

Here  $C_{pvf}$  is the final viscous pressure coefficient and  $C_{pp}$  is the initial potential pressure coefficient. The pressure drag is then given by

$$\begin{aligned} C_{pv} &= \frac{\pi r_{\max}^2}{A} \int_0^1 \frac{L}{r_{\max}} \frac{2 r_o}{r_{\max}} \Delta C_{pv} \tan \alpha \, d \left( \frac{X}{L} \right) \\ &= \frac{2\pi}{A} \int_{r_o(x=0)}^{r_o(x=L)} r_o \Delta C_{pv} \, d r_o \end{aligned} \quad (17)$$

The overall drag coefficient has been computed for three reference areas: frontal area, wetted area, and  $(\text{volume})^{2/3}$ . The frontal area and  $(\text{volume})^{2/3}$  are of interest under certain design constraints where the frontal area and/or the volume are taken to be fixed. On the other hand, the use of the wetted area is convenient when the drag of a body is compared to that of an equivalent flat plate.

### Description of Computer Program

The above method has been synthesized into a single computer program by essentially combining the Douglas potential-flow program<sup>27</sup> and the Douglas CS boundary-layer program.<sup>13,30</sup> Since the original potential-flow program consisted of several overlay links, the boundary-layer program was made the last link of the potential-flow program. In order to simplify the overall program as much as possible, several computations contained in the original potential-flow program were deleted, including all the computations for cross flow. Also, all of the options for solving for source densities were deleted except for the Seidel iteration method.

The synthesized program expands the number of boundary-layer output variables and adds the calculation of flow in the wake to the boundary-layer program. The program has been written so that it can bypass the potential flow calculations and directly accept pressure distribution as an input. In these cases, the program also allows for the reading in of

additional data which modify the input pressure distribution. This feature is of direct interest for studying the influence of the propeller on the boundary-layer flow over the body. In these cases, the input pressure distribution may be the calculated or measured bare-hull pressure distribution and the modifying pressure distribution is that due to the propeller.

On the CDC 6700 computer currently being used at the Center, 470 sec of execution time are typically needed to compute the three iterations required to arrive at the final pressure distribution. The program requires approximately 65 sec to compile and a computer memory of approximately 145,000 octal words.

#### **PROPELLER-HULL INTERACTION: FRICTIONAL AND PRESSURE-DEFECT COMPONENTS OF THRUST DEDUCTION**

It is well known in naval architecture that the delivered propeller thrust is greater than the hull resistance in the absence of the propeller, except in very rare cases. Traditionally, the increase in resistance due to propeller-hull interaction has been defined in terms of a thrust deduction fraction  $t$

$$t = \frac{T - R}{T}$$

where  $T$  is the delivered propeller thrust and  $R$  is the hull resistance. The theoretical and experimental literature on thrust deduction is very extensive.<sup>1-6</sup> Weinblum<sup>2</sup> summarized the earlier contributions of hydrodynamicists to the understanding and formulation of the physics of thrust deduction. In addition, an extensive list of references with application to surface ships can be found in the paper by Nowacki and Sharma.<sup>6</sup> A potential-flow computation scheme based on Lagally's theorem for calculating thrust deduction was presented by Beveridge.<sup>1</sup>

An operating propeller produces an upstream suction which causes a reduction in pressure on the afterbody and results in an increase of hull pressure drag. Simultaneously, this suction also causes an increase of shear stress on the afterbody and results in an increase of frictional drag. Thus, the thrust deduction for a fully submerged, axisymmetrical, self-propelled body may be divided into two components, namely,  $t = t_F + t_P$ . The pressure-defect component  $t_P$  is given by

$$\begin{aligned}
t_p &= \frac{2}{C_{TS}} \int_0^{L/R_p} -(\Delta C_p) \frac{r}{R_p} \tan \alpha \frac{dx}{R_p} \\
&\cong \frac{2}{C_{TS}} \int_{r_h}^{r_{\max}} (\Delta C_p) \frac{r}{R_p} \frac{dr}{R_p}
\end{aligned} \tag{18}$$

and the frictional component  $t_F$  by

$$\begin{aligned}
t_F &= \frac{2}{C_{TS}} \int_0^{L/R_p} (\Delta C_{\tau}) \left( \frac{U_e}{U_o} \right)^2 \frac{r}{R_p} \frac{dx}{R_p} \\
&\cong \frac{2}{C_{TS}} \int_{x_{\max}}^{x_h} (\Delta C_{\tau_o}) \frac{r}{R_p} \frac{dx}{R_p}
\end{aligned} \tag{19}$$

where  $C_{TS} = \frac{T}{\rho \frac{U_o^2}{2} \pi R_p^2}$  (thrust loading coefficient based on ship speed)

$\Delta C_p = (C_p)_b - (C_p)_p$  (decrease of pressure coefficient due to propeller)

$\Delta C_{\tau_o} = (\Delta C_{\tau}) \left( \frac{U_e}{U_o} \right)^2 = [(C_{\tau})_p - (C_{\tau})_b] \left( \frac{U_e}{U_o} \right)^2$  (increase of local skin friction coefficient due to propeller)

$\tan \alpha = dr/dx$

The pressure contribution to the propeller-hull interaction is approximated by the potential-flow approximation of  $\Delta C_p$ . The propeller-induced velocity on the hull can be computed from the propeller field point program.<sup>31</sup> To determine the change in pressure due to the presence of the propeller, the Douglas-Neumann computer program<sup>13</sup> has to be employed with a nonzero normal velocity at each quadrilateral in order to cancel the normal velocity induced by the propeller

$$\frac{\partial \phi}{\partial n} = -V_n = (V_n)_{\text{propeller}} = v_{pr} \cos \alpha - u_a \sin \alpha$$

<sup>31</sup>Kerwin, J.E. and R. Leopold, "A Design Theory for Subcavitating Propellers," Transactions of the Society of Naval Architects and Marine Engineers, Vol. 72, pp. 294 - 335 (1964).



Here  $n$  is the unit outward normal to the surface,  $v_{pr}$  is the propeller-induced radial velocity, and  $u_a$  is the propeller-induced axial velocity. Thus, when the velocity fields of the hull and the propeller are superimposed, the normal velocity will be zero along the body contour. The total pressure coefficient in the presence of the propeller is

$$(C_p)_p = 1 - \frac{U_p^2}{U_o^2} = 1 - \left( 1 + \frac{u_s}{U_o} + \frac{u_{sn}}{U_o} + \frac{u_{sp}}{U_o} \right)^2 \quad (20)$$

Here  $U_p$  is the total surface potential velocity in the presence of the propeller, which consists of  $u_s$  (the perturbation velocity due to the bare hull),  $u_{sn}$  (perturbation velocity as the result of cancelling the normal propeller-induced velocity), and  $u_{sp} = u_a \cos \alpha + v_{pr} \sin \alpha$  (the propeller-induced tangential velocity on the hull). The original pressure coefficient of the bare hull is denoted by  $(C_p)_b$ . Since the pressure-defect component of thrust deduction is of a potential-flow nature, the computed  $t_p$  due to the interaction of propeller-induced velocity on the hull, Equation (18), is therefore equal to the Beveridge<sup>1</sup> formulation of the effect of hull-induced velocity on the propeller.

### PROPELLER AND STERN BOUNDARY-LAYER INTERACTION

The boundary-layer velocity profile in the absence of the propeller is called the nominal profile. The nominal velocity distribution at the propeller plane of the ship model is usually measured by a standard wake rake before the actual design of the full-scale propeller is undertaken. The suction of the propeller accelerates the flow in the vicinity of the propeller. The effective velocity profile to be used in the design of a wake-adapted propeller is the result of the interaction of the propeller and the thick stern boundary layer. The radial distribution of effective velocity profile is sometimes scaled up or down from the measured circumferential-mean nominal velocity profile by a constant factor. This constant factor has been taken as the ratio of the Taylor wake fraction to the measured volume-mean nominal wake fraction. This constant-factor approach can be considered only as a rough empirical approximation. As stated earlier, the only known previous effort to address this problem theoretically was by D.M. Nelson\* who developed an unpublished computer program for calculating the effective wake from the measured nominal wake *and* static pressure distribution across the boundary layer. The method to be presented below was developed by using an approach different from

\*Private communication as indicated earlier.

that of Nelson and requires only the measured nominal wake distribution. A serious effort has been made here to compare the theoretical wake predictions with wake distribution measured by LDV in the presence of a propeller.

### THEORETICAL CONSIDERATIONS

The experimental evidence shown in the next section allows one to conclude that the influence of the propeller on the axisymmetrical stern boundary layer is limited to a region extending two propeller diameters upstream of the propeller. It is also known, from theory, that the mean circumferential velocity  $v_\theta$  upstream of the propeller is identically equal to zero with (or without) the propeller in operation. The following assumptions are made to derive a theoretical approximation of the hydrodynamic interaction between a propeller and a fully developed thick turbulent boundary layer upstream of the propeller: (1) the flow is axisymmetric and the fluid is incompressible; (2) the interaction of propeller and stern boundary layer is considered to be inviscid in nature and thus propeller-induced viscous losses and turbulent Reynolds stresses are neglected; (3) the conventional boundary-layer assumption of  $\partial v_r / \partial x \ll \partial u_x / \partial r$  is considered to be valid for the nominal boundary layer in the absence of a propeller; and (4) upstream of the propeller, no energy is added to the fluid by the propeller, and the propeller-induced velocity field upstream of the propeller is irrotational.

The vector equation of steady motion for an inviscid fluid is given by (see, for example, Thwaites<sup>32</sup>)

$$\vec{V} \times \vec{\omega} = \frac{1}{\rho} \text{grad } H \quad (21)$$

Here  $\vec{V}$  is the fluid velocity,  $\vec{\omega} = \nabla \times \vec{V}$  is the vorticity vector, and  $H = P + \frac{1}{2} \rho (\vec{V} \cdot \vec{V}) = P + \frac{1}{2} \rho (v_r^2 + v_\theta^2 + u_x^2)$  is the total head. For cylindrical polar coordinates  $(r, \theta, x)$ , with  $\vec{V} = (v_r, v_\theta, u_x)$ , the radial component of Equation (21) may be written in the form

$$\frac{r v_\theta}{r^2} \frac{\partial(r v_\theta)}{\partial r} - u_x \omega_\theta = \frac{1}{\rho} \frac{dH}{d\psi} \frac{d\psi}{dr} \quad (22)$$

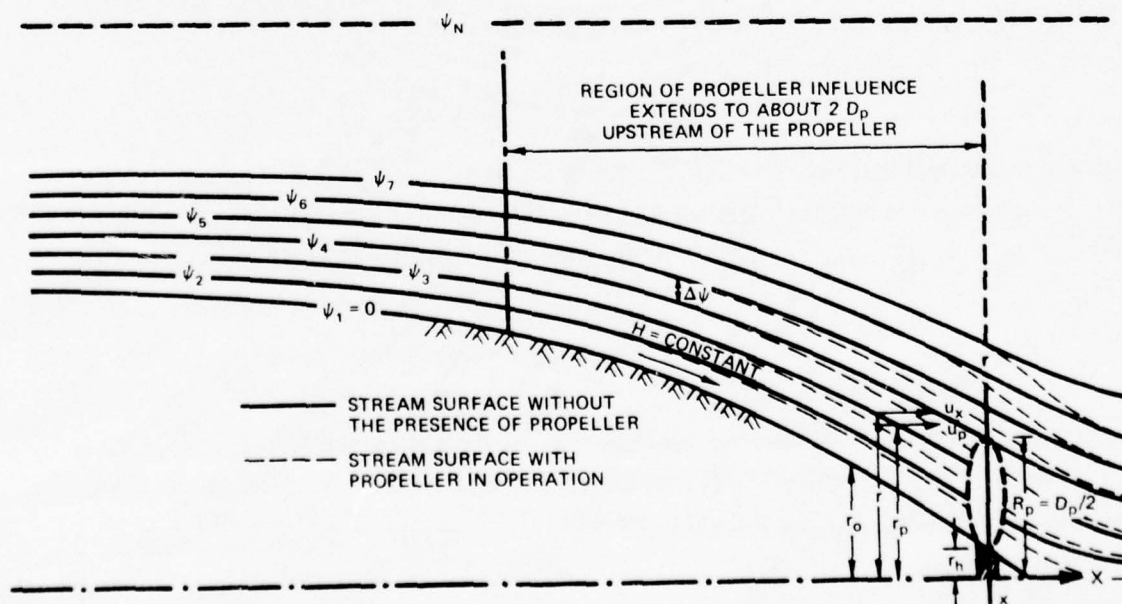
where the total pressure head  $H$  is a function only of the stream function  $\psi$  and  $\omega_\theta = \partial v_r / \partial x - \partial u_x / \partial r$  is the  $\theta$ -component of the vorticity vector. For an incompressible axisymmetrical flow, a stream function may be introduced such that

<sup>32</sup>Thwaites, B., "Incompressible Aerodynamics," Oxford University Press (1960), Chapter XI.

$$v_r = \frac{1}{r} \frac{\partial \psi}{\partial x}$$

$$\frac{1}{\rho} \frac{\partial H}{\partial \psi} = \frac{1}{r} \left( \frac{\partial u_x}{\partial r} - \frac{\partial v_r}{\partial x} \right) \quad (23)$$

Recall that the boundary-layer velocity profile in the absence of the propeller is called the nominal profile. The suction of the propeller accelerates the flow in the vicinity of the propeller and the stream surfaces are shifted closer to the body surface. As shown in Figure 6, a typical stream surface moves inward from  $r$  to  $r_p$  while the velocity is increased from the nominal velocity  $u_x$  to  $u_p$  due to the interaction of the propeller with the nominal velocity profile. The resultant velocity  $u_p$  measured in front of an operating propeller will be called the apparent velocity profile. The input velocity profile to be used in the design of a wake-adapted propeller will be called the effective velocity profile. The effective velocity profile is the apparent velocity profile minus the irrotational-flow, propeller-induced velocity profile.



28



The normal boundary-layer approximation  $\partial v_r / \partial x \ll \partial u_x / \partial r$  is assumed to be valid for the nominal profile. Therefore, from Equation (23)

$$\frac{1}{\rho} \frac{dH}{d\psi} = \frac{1}{r} \left( \frac{\partial u_x}{\partial r} - \frac{\partial v_r}{\partial x} \right) \cong \frac{1}{r} \frac{\partial u_x}{\partial r} \text{ without a propeller} \quad (24)$$

Applied to the resultant flow with the propeller in operation, Equation (23) results in

$$\frac{1}{\rho} \left( \frac{\partial H}{\partial \psi} \right)_p = \frac{1}{r_p} \left[ \frac{\partial u_p}{\partial r_p} - \frac{\partial (v_r + v_{pr})}{\partial x} \right] \cong \frac{1}{r_p} \left( \frac{\partial u_p}{\partial r_p} - \frac{\partial v_{pr}}{\partial x} \right), \text{ with propeller} \quad (25)$$

Here we have neglected propeller interaction on the radial velocity. The radial velocity with the propeller in operation is equal to  $v_r + v_{pr}$ , where  $v_r$  is the radial velocity without propeller and  $v_{pr}$  is the circumferential-average propeller-induced radial velocity. The term  $\partial v_r / \partial x$  used to approximate Equation (24) has also been neglected for the same reason.

Since no energy is added to the upstream fluid by the propeller and since we assume no viscous losses due to propeller-induction effects, the total pressure head within the same stream annulus remains constant with and without the propeller in operation, i.e., upstream of the propeller

$$\frac{1}{\rho} \frac{dH}{d\psi} = \frac{1}{\rho} \left( \frac{dH}{d\psi} \right)_p$$

Furthermore, we have assumed that the propeller-induced velocity field is irrotational, i.e.,

$$\nabla \times \vec{V}_p = \frac{\partial v_{pr}}{\partial x} - \frac{\partial u_a}{\partial r_p} = 0$$

where  $\vec{V}_p$  is the total propeller-induced velocity, and  $v_{pr}$  and  $u_a$  are the circumferential-average radial and axial propeller-induced velocities, respectively. With these two conditions, we obtain a simple formula from Equations (24) and (25) for the location of the new stream surface  $r_p$

$$\frac{1}{r} \frac{\partial u_x}{\partial r} = \frac{1}{r_p} \left( \frac{\partial u_p}{\partial r_p} - \frac{\partial u_a}{\partial r_p} \right) \quad (26)$$

At a given location of  $x$  within a given stream annulus having constant mass flow, we have by definition

$$d\psi = r u_x dr = r_p u_p dr_p \quad (27)$$

Thus, Equation (26) may be rewritten as

$$u_x du_x = u_p d(u_p - u_a) \quad (28)$$

Equations (27) and (28) are the governing equations for the propeller and stern boundary-layer interaction. (The same theory is also valid for a windmilling propeller which retards the flow upstream of the propeller.) In the absence of a propeller, the nominal velocity profile ( $u_x$  versus  $r$ ) and the propeller-induced axial velocity profile ( $u_a$  versus  $r$ ) can be used to obtain the new location of the stream surface  $r_p$  with velocity equal to  $u_p$  via Equations (27) and (28). Equation (27) is a statement of the conservation of mass in an incompressible fluid; the values of  $r$  and  $r_p$  begin at  $r = r_p = r_0$  ( $r_0$  is the radius of the body) and move outward. Far outside the boundary layer as  $r_p \rightarrow \infty$ ,  $du_x = 0$  in Equation (28); this implies  $d(u_p - u_a) = 0$  and  $u_p - u_a = \text{constant} = U_0$  since  $u_a$  is zero and  $u_p$  has to be equal to  $U_0$  as  $r_p \rightarrow \infty$ . Thus, for  $r_p \rightarrow \infty$ , the effective velocity is identically equal to  $U_0$  or the apparent velocity  $u_p = U_0 + u_a$ . These results are, of course, valid for a propeller operating in open water where the difference in the nominal velocity  $du_x$  is identically equal to zero since  $u_x = U_0$  for all  $r$ . Thus, the effective velocity for a propeller operating in open water is identically equal to  $U_0$  even though the apparent velocity  $u_p$  is equal to  $U_0 + u_a(r_p)$ .

## NUMERICAL SOLUTION

The nominal velocity  $u_x$  can be approximated very accurately over a small increment of radius  $dr$  by a linear function of  $r$ . Although the velocity at the wall is zero, the velocity profile in the present approximation will be extrapolated linearly toward the wall, resulting in a nonzero velocity at the wall. Since  $u_x$  and  $u_p$  can be approximated locally by a linear function of  $r$  and  $r_p$ , the mass flux within the stream tube annulus given by  $dr = r_{i+1} - r_i$  and  $dr_p = r_{pi+1} - r_{pi}$  can be integrated from Equation (27) as

$$\psi_{i+1} - \psi_i = \Delta\psi_i = \int_{r_i}^{r_{i+1}} r u_x dr = \int_{r_{pi}}^{r_{pi+1}} r_p u_p dr_p$$

with  $u(r) = u_i + [(r - r_i)/(r_{i+1} - r_i)](u_{i+1} - u_i)$  and  $r_i \leq r \leq r_{i+1}$  to obtain the finite difference form as

$$\begin{aligned}
& (r_{i+1}^2 - r_i^2) \left[ (2u_{x_{i+1}} + u_{x_i}) - (u_{x_{i+1}} - u_{x_i}) \frac{r_i}{r_{i+1} + r_i} \right] \\
& = (r_{p_{i+1}}^2 - r_{p_i}^2) \left[ (2u_{p_{i+1}} + u_{p_i}) - (u_{p_{i+1}} - u_{p_i}) \frac{r_{p_i}}{r_{p_{i+1}} + r_{p_i}} \right] \quad (29)
\end{aligned}$$

Equation (28) can also be written in the finite difference form

$$(u_{x_{i+1}}^2 - u_{x_i}^2) = (u_{p_{i+1}} + u_{p_i})(u_{p_{i+1}} - u_{p_i} - u_{a_{i+1}} + u_{a_i}) \quad (30)$$

Equations (29) and (30) are simultaneous equations to be used to solve for  $r_p$  and  $u_p$ . A simple computer program has been developed<sup>33</sup> to solve them.

## PREDICTION OF PROPELLER PERFORMANCE

The nominal circumferential-mean velocity profile at the propeller plane ( $x = 0$ ) of a ship model is usually determined experimentally from pitot tube measurements in the absence of the propeller. The effective velocity profile is the profile the propeller blades experience in producing the local thrust and torque. The effective profile is an important input in the design of the modern wake-adapted propeller. The effective profile is sometimes scaled up or down from the measured nominal profile by a constant factor which is taken to be the ratio  $(1 - w_T)/(1 - w_V)$ , where  $w_T$  is the Taylor wake fraction and  $w_V$  is the volumetric mean nominal wake fraction determined from a pitot-tube survey. An accurate effective velocity profile is vital for the successful design of a wake-adapted propeller and for the correct prediction of propeller powering and cavitation performance. It is essential to develop a reliable and sound theoretical procedure to calculate the effective velocity profile. In the present investigation, the effective velocity profile will be computed by a simple iteration scheme based on propeller/stern boundary-layer interaction theory and a propeller inverse program.<sup>34</sup> A brief description is outlined below.

The nominal wake  $w(r)$  is defined as

$$\frac{u_x(r)}{U_0} = 1 - w(r)$$

<sup>33</sup>Huang, T.T., "User's Manual for a Fortran IV Computer Program for Calculating Propeller/Stern Boundary-Layer Interaction on Axisymmetrical Bodies," DTNSRDC Report SPD-737-02 (1976).

<sup>34</sup>Cummings, D.E., "Numerical Prediction of Propeller Characteristics," Journal of Ship Research, Vol. 17, Pt 3, pp. 12-18 (1973).



The effective wake experienced by a propeller blade section is defined by

$$\frac{u_e(r_p)}{U_o} = \frac{u_p(r_p)}{U_o} - \frac{u_a(r_p)}{U_o} = 1 - w_e(r_p)$$

In current design practice, the effective wake distribution is sometimes estimated by the following approximation

$$\frac{u_e(r_p)}{U_o} = 1 - w_e(r_p) = C \frac{u_x(r_p)}{U_o}$$

where

$$C = \frac{1 - w_T}{1 - w_V}, \quad 1 - w_V = \frac{2}{1 - r_h^2} \int_{r_h}^1 \frac{u_x(r_p)}{U_o} \frac{r_p}{R_p} d\left(\frac{r_p}{R_p}\right)$$

The Taylor wake fraction  $w_T$  is determined experimentally from self-propulsion and open-water propeller tests in a towing tank;  $w_V$  is the volumetric mean wake derived from wake surveys conducted in the absence of a propeller. Because of the difference in the propeller loading and ambient turbulence (which affects the propeller section drag coefficient), the propeller characteristics in the behind condition can be quite different from characteristics in open water. Furthermore, the propeller interaction on the boundary layer cannot be represented by a constant correction factor. In order to improve the prediction of the effective velocity profile from the measured velocity profile at the propeller plane, we use the following simple iteration scheme based on the previously discussed propeller/stern boundary-layer interaction program and the propeller inverse program developed by Cummings:<sup>34</sup>

1. Use the measured nominal velocity profile to estimate an effective velocity profile. One may start with the guess  $u_e(r) = 1.1 u_x(r)$ .
2. Use the propeller inverse program developed by Cummings<sup>34</sup> to calculate the propeller nondimensional circulation distribution  $G(r_p)^*$  from the estimated effective velocity profile  $u_e(r_p)$  and the propeller geometry.
3. Use the propeller field-point velocity program<sup>31</sup> to calculate the average propeller-induced axial velocity  $u_a$ .

\*The inverse program has to be calibrated with the conventional design program<sup>31, 35, 36</sup> for the given effective profile for which the particular propeller is designed.

<sup>35</sup>Cox, G.G. and W.B. Morgan, "Use of Theory in Propeller Design," *Marine Technology*, Vol. 2, No. 4, pp. 319 - 329 (1972).

<sup>36</sup>Morgan, W.B. et al., "Propeller Lifting-Surface Corrections," *Transactions, the Society of Naval Architects and Marine Engineers*, Vol. 76, pp. 309 - 347 (1968).

4. Use the propeller/stern boundary-layer interaction program to compute  $u_p(r_p)$  from the measured value of  $u_x(r)$  and computed value of  $u_a(r_p)$ .

5. The new effective profile becomes  $u_e(r_p) = u_p(r_p) - u_a(r_p)$ .

6. Repeat Steps 2-4 until  $u_e(r_p)$  and  $G(r_p)$  converge.

The final computed nondimensional circulation distributions  $G(r)$  for the three afterbodies are shown in Figure 7. It has been found that the values of  $u_e/U_0$  and  $G(r)$  have essentially converged to their final values after three iterations. The computations also show that the ratio of the effective to nominal velocity distribution  $u_e(r_p)/u_x(r_p) = u_p(r_p)/u_x(r_p) - 1 - u_a(r_p)/u_x(r_p)$  does not take a constant value. In fact, the ratio of  $u_e(r_p)/u_x(r_p)$  has a larger value near the hub of the propeller than near the tip.

## COMPARISON OF EXPERIMENTAL AND THEORETICAL RESULTS

### MEASURED AND COMPUTED PRESSURE AND SHEAR STRESS DISTRIBUTIONS

The measured and computed values of pressure coefficient are compared in Figure 8 for Afterbodies 1, 2, and 3 at a length Reynolds number  $R_n = 5.9 \times 10^6$ . The virtual origin of turbulence was fixed at  $X/L = 0.015$  (Figure 4b). The agreement was very good for Afterbody 1, fairly good for Afterbody 2, and relatively poor for Afterbody 3. Recall that Afterbody 1 did not separate, Afterbody 2 approached separation, and Afterbody 3 separated at  $X/L = 0.92$ . Because of the severe adverse pressure gradients on Afterbodies 2 and 3, the boundary layer became very thick and the accuracy of the predictions was degraded. The results suggest that the present method is accurate for sterns without severe adverse pressure gradients but less accurate for sterns with progressively more severe pressure gradients. Thus, further improvement of the present computation method is necessary.

Figure 9 shows the measured and computed difference between the viscous flow and potential flow pressure ( $C_{pvf} - C_{pp}$ ) for the three afterbodies. The shaded areas indicate the additional drag caused by separation on Afterbody 3 and the additional measured stern pressure drag over the prediction on Afterbody 2.

The measured and computed local shear stress distributions  $C_\tau$  are compared for Afterbody 1 in Figure 10, for Afterbody 2 in Figure 11, and for Afterbody 3 in Figure 12. Two body-length Reynolds numbers ( $R_n = U_0 L/\nu$ ) of  $5.9 \times 10^6$  and  $8.8 \times 10^6$  were used in the experiments. As can be seen from these figures, the agreement was good for Afterbodies 1 and 2. However, for Afterbody 3, agreement between measured and computed shear stresses

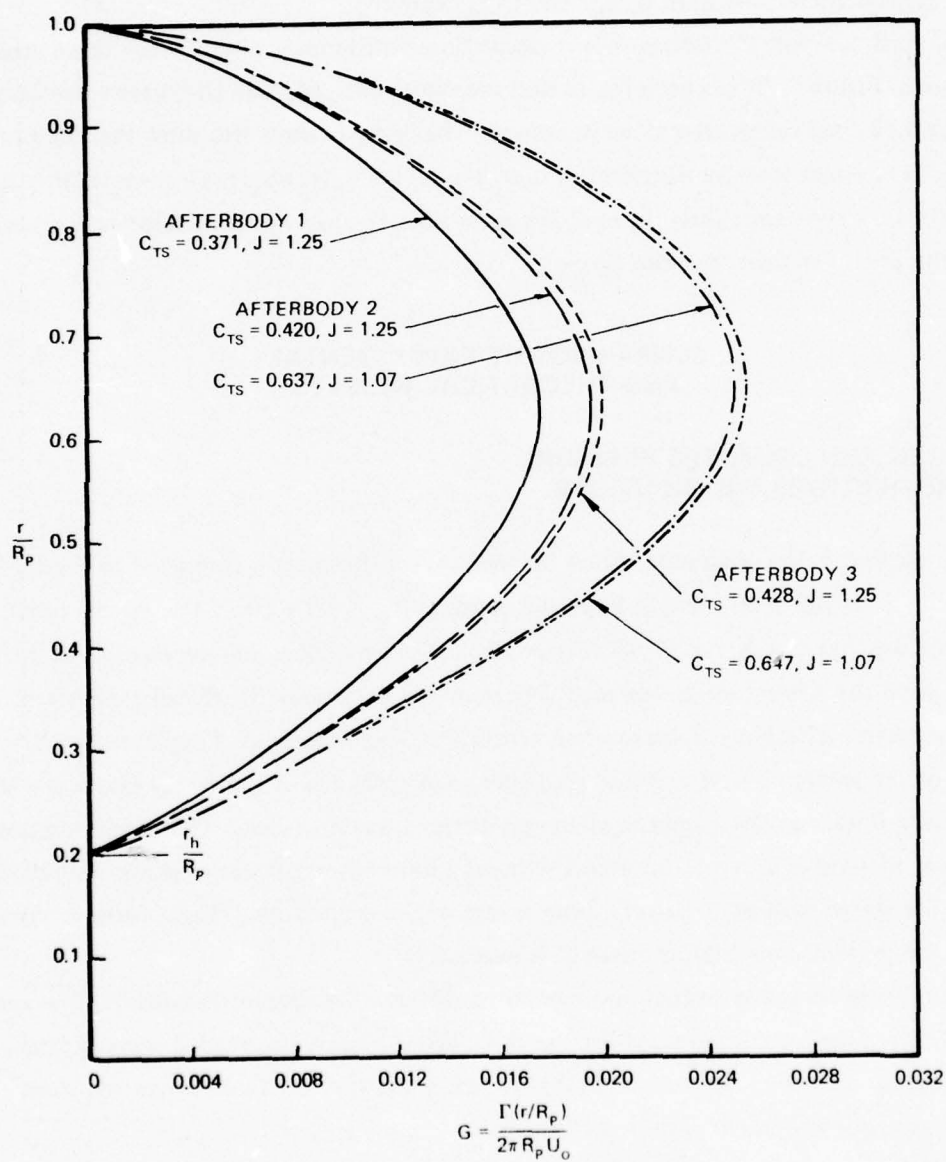


Figure 7 – Nondimensional Circulation for the Propeller Operated in the Wake of Three Afterbodies



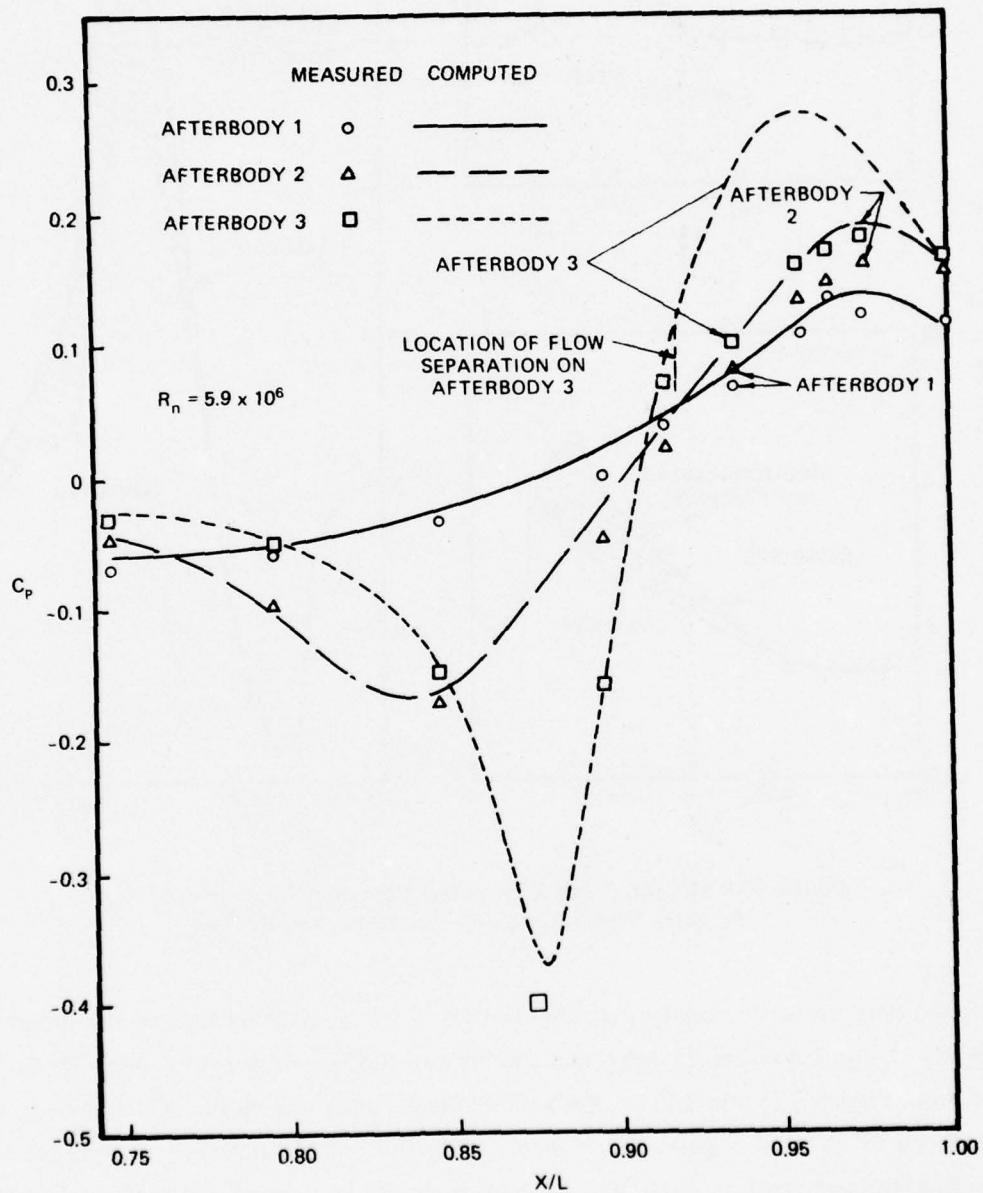


Figure 8 — Measured and Computed Stern Pressure Distributions for the Three Afterbodies

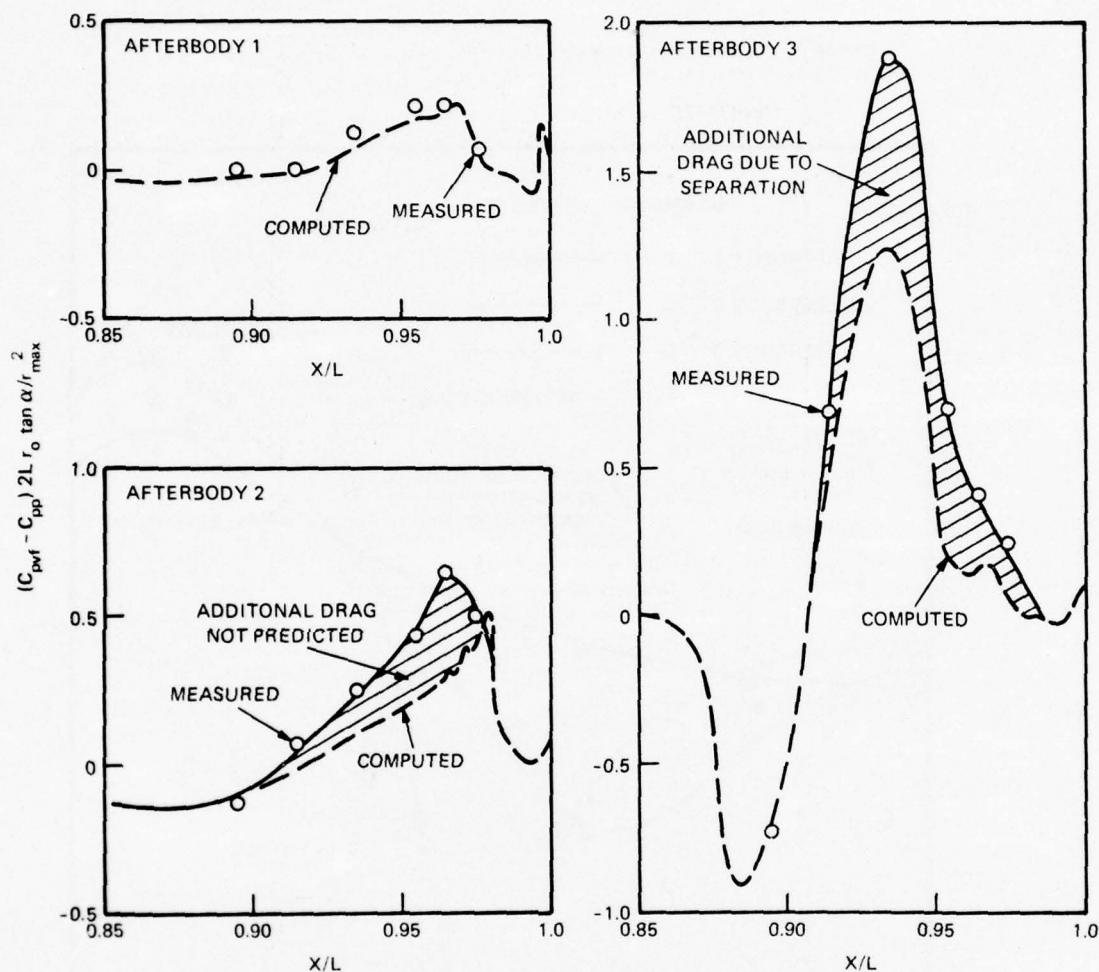


Figure 9 — Measured and Computed Viscous Effect on the Stern Pressure Distributions of the Three Afterbodies

was good only up to the point of separation ( $X/L = 0.92$ ); after separation, the present computational method breaks down and the Preston tube measurement is also questionable. Therefore, Figures 12a and 12b do not include results after separation. Qualitatively, the shear stress takes small negative values in the separation bubble and becomes positive again after flow reattachment at about  $X/L = 0.97$ . It should be pointed out that the computed values of  $C_T$  for Afterbodies 1 and 2 were higher than the measured values of  $C_T$  at  $X/L > 0.95$ . This discrepancy is similar to that for the measured and computed pressure distributions. The disagreement between measured and computed values of  $C_T$  at  $X/L > 0.95$  was more noticeable for Afterbody 2 than Afterbody 1.

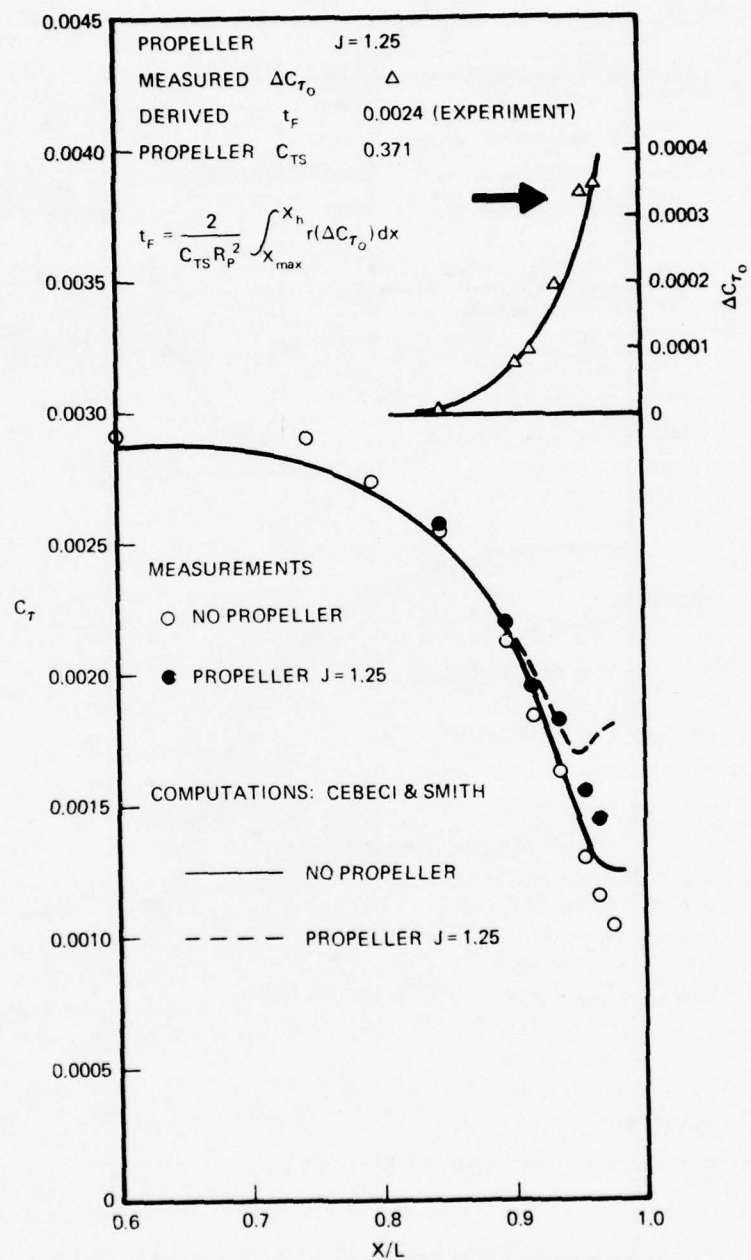


Figure 10a -  $R_n = 5.9 \times 10^6$

Figure 10 - Measured and Computed Skin Friction Distribution on Afterbody 1 with and without Propeller in Operation



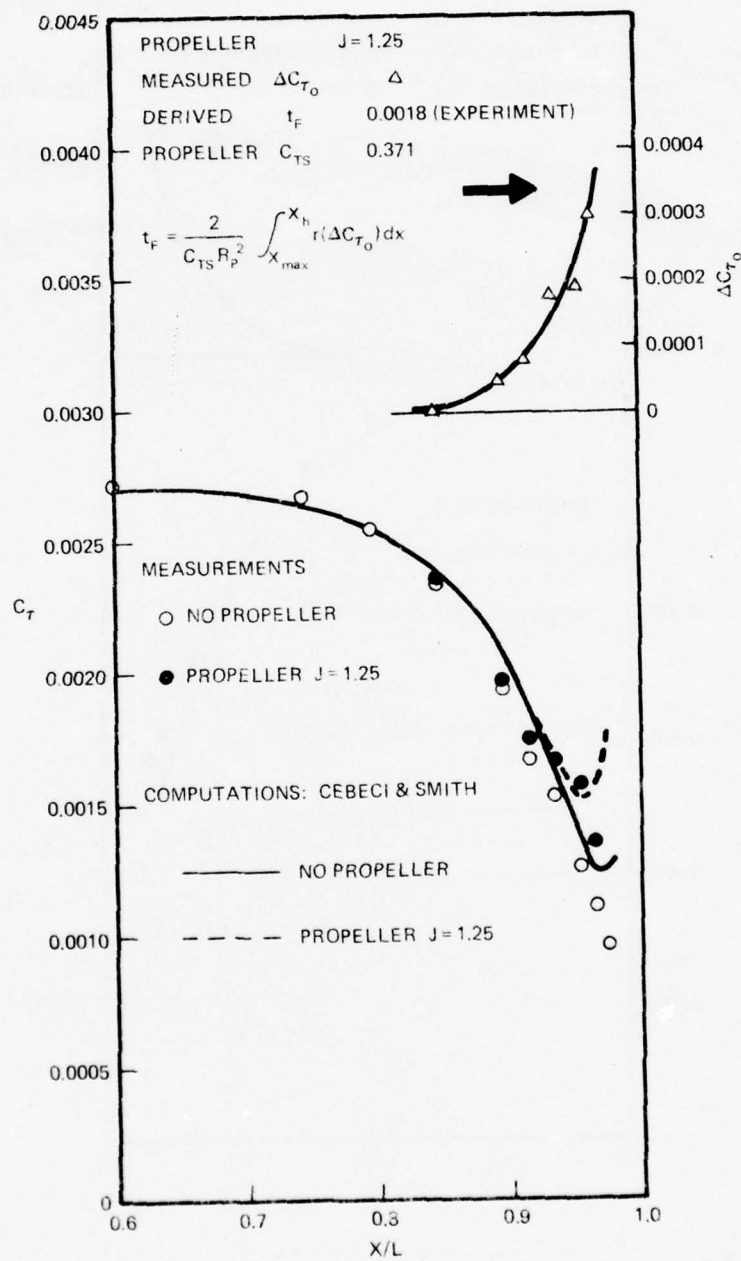


Figure 10b -  $R_n = 8.8 \times 10^6$

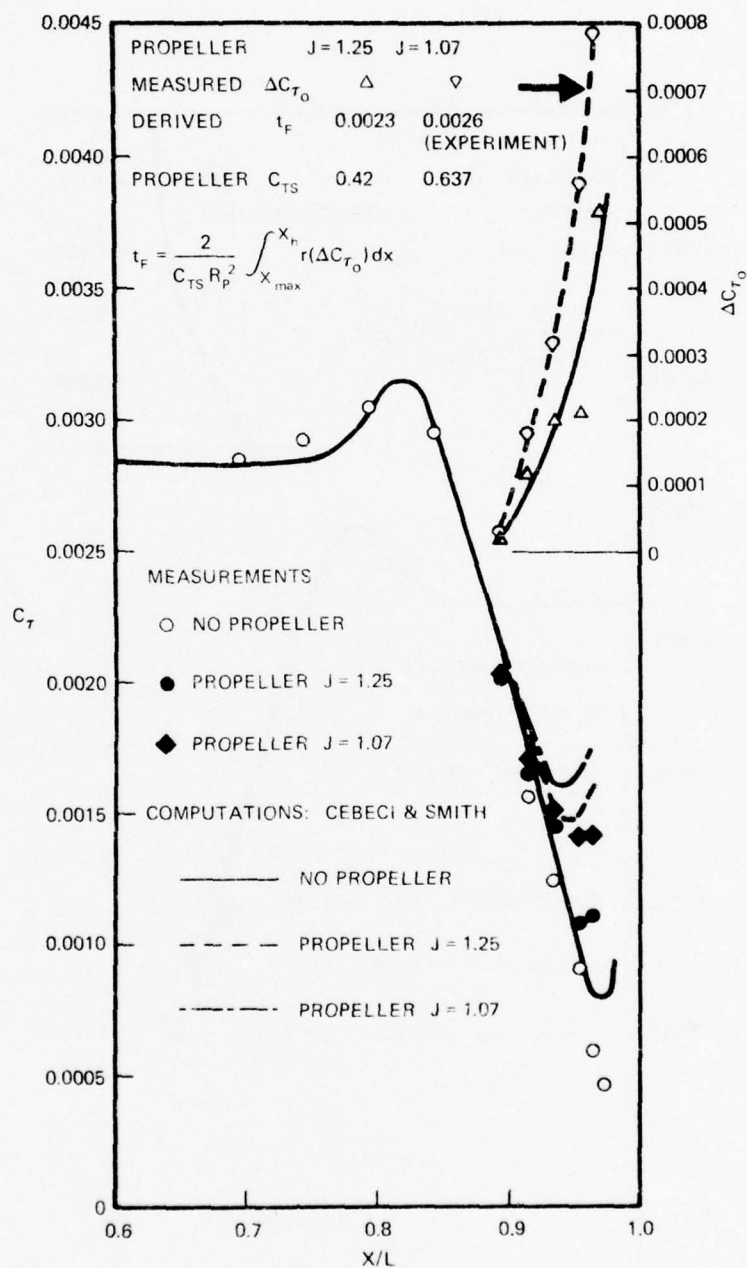


Figure 11a -  $R_n = 5.9 \times 10^6$

Figure 11 - Measured and Computed Skin Friction Distribution on Afterbody 2 with and without Propeller in Operation

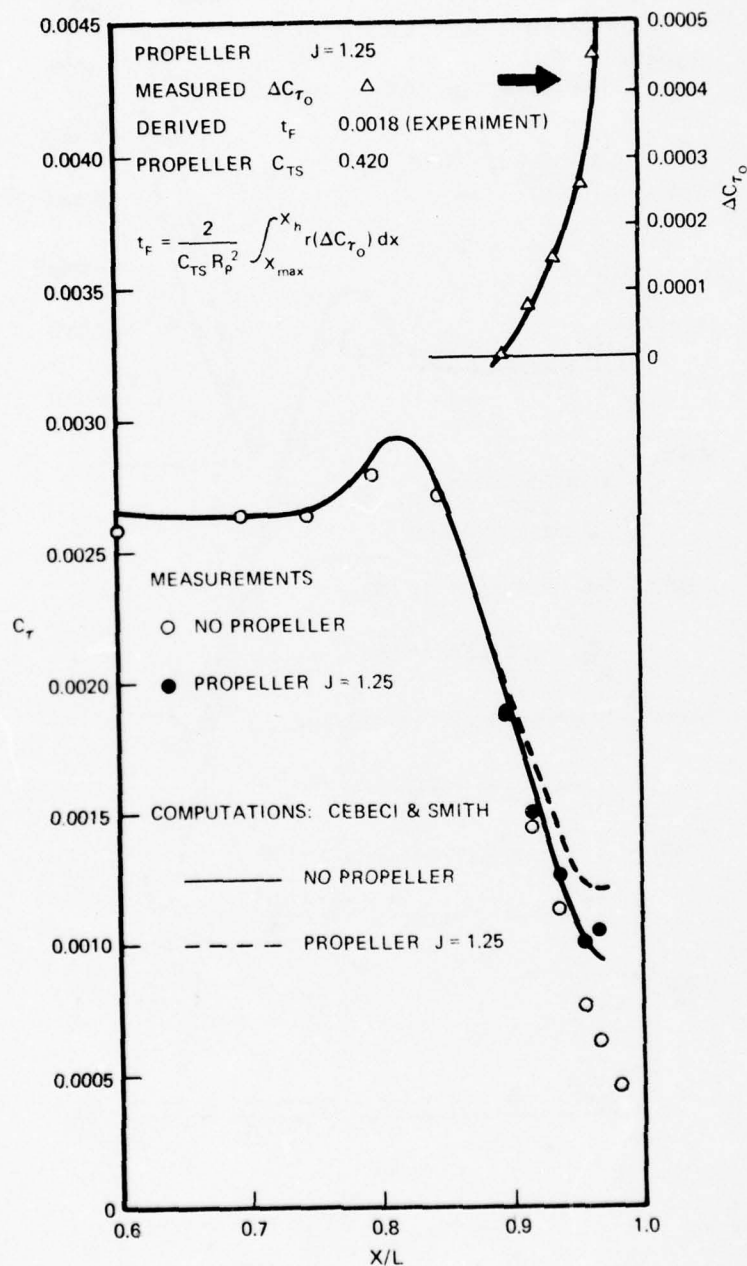


Figure 11b -  $R_n = 8.8 \times 10^6$



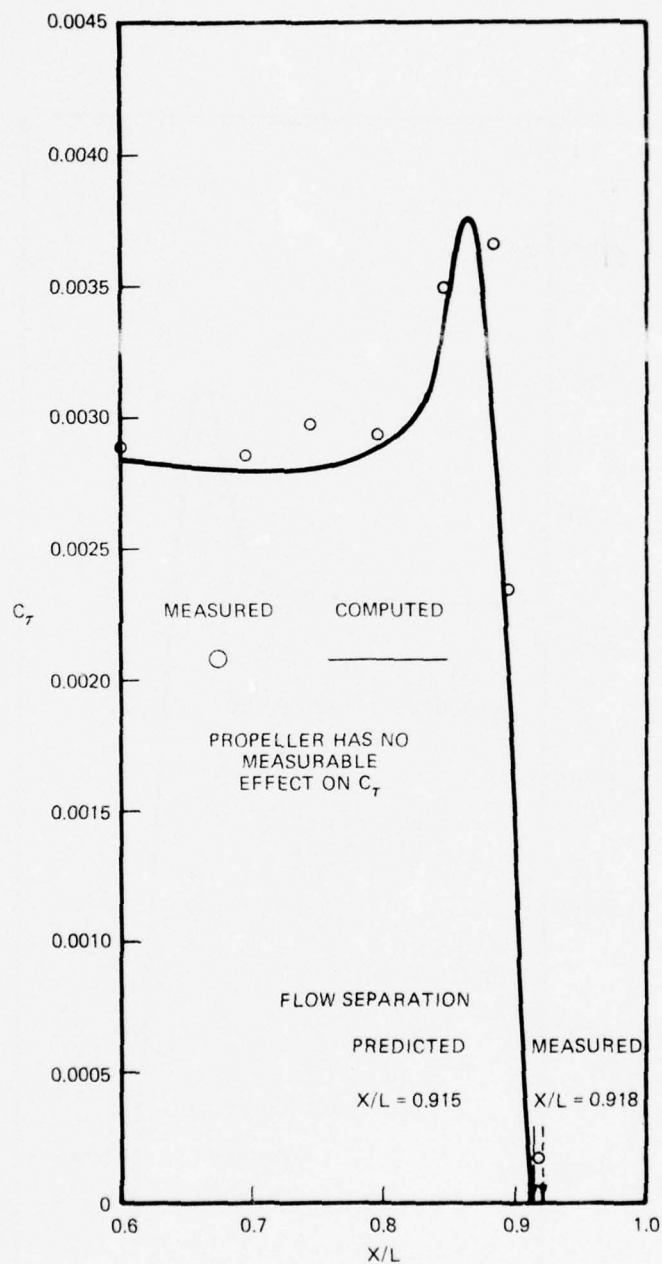


Figure 12a -  $R_n = 5.9 \times 10^6$

Figure 12 - Measured and Computed Skin Friction Distribution on Afterbody 3 with and without Propeller in Operation

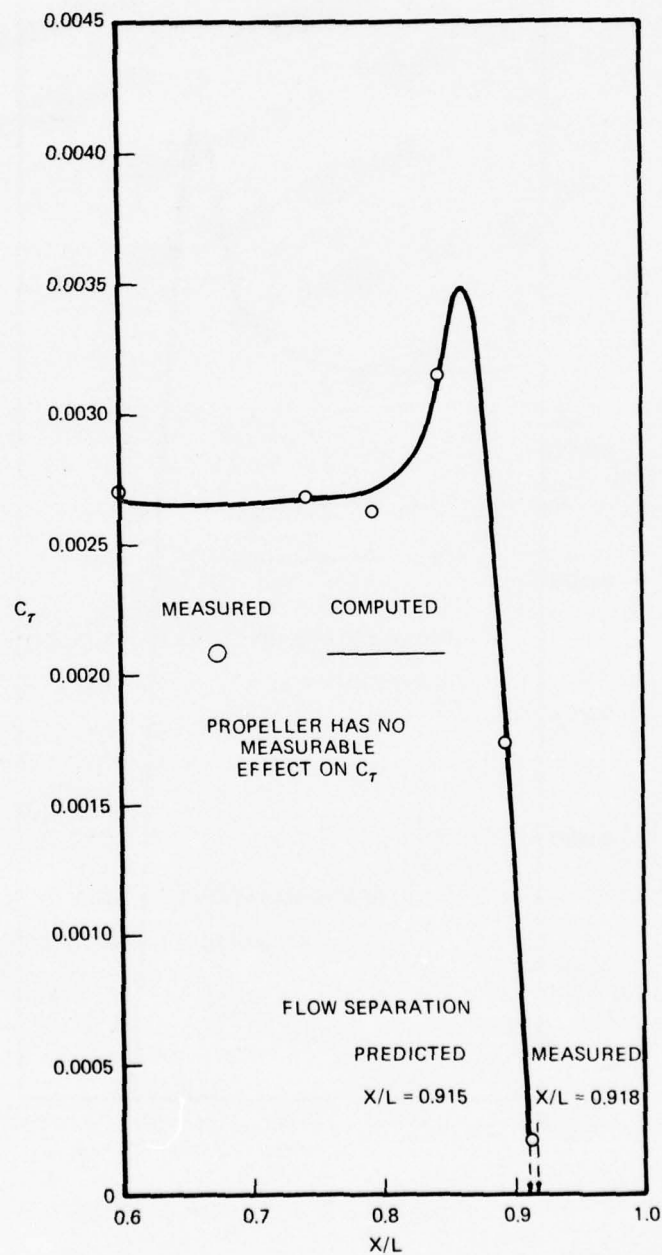


Figure 12b -  $R_n = 8.8 \times 10^6$

The effect of the propeller on the stern pressure distribution was computed by the potential-flow approximation method described earlier. As can be seen from Equation (20), the total surface perturbation potential velocity in the presence of the propeller is the sum of the bare-hull perturbation velocity (including the displacement effect), the perturbation velocity as the result of cancelling the propeller-induced velocity normal to the hull, and the propeller-induced velocity tangential to the hull. The boundary-layer calculation can be made by using the computed total surface perturbation potential velocity in the presence of a propeller.

In connection with the measured and computed values of  $C_T$  with the propeller in operation (Figures 10-12), note that as expected, the propeller accelerated the flow at the stern, resulting in an increase of shear stress. However, this increase of  $C_T$  was limited to the region  $X/L \geq 0.90$ . No effect was noted at distances larger than two propeller diameters ( $2D_p$ ) upstream from the propeller. As shown in Figures 12a and 12b, the suction of the propeller did not change the point of boundary-layer separation on Afterbody 3. The distance between the propeller plane and the point of separation was 1.3 propeller diameters. The propeller-induced velocity at  $1.3 D_p$  upstream of the propeller was not strong enough to alter the characteristics of the separation.

Figures 13-15 show the measured and computed pressure distributions with and without the propeller in operation. Again, the effect of the propeller on pressure distribution was evident up to a distance of  $2D_p$  upstream of the propeller. As can be seen from Figures 13 and 14, the measured values of  $(C_p)_p$ ,  $(C_p)_b$ , and  $\Delta C_p = (C_p)_b - (C_p)_p$  were in good agreement with the computed values for Afterbodies 1 and 2. In the case of Afterbody 3 (Figure 15), the measured values of  $\Delta C_p$  were smaller than the computed values of  $\Delta C_p$  aft of the separation point  $X/L = 0.92$ . These smaller measured values of  $\Delta C_p$  may have been caused by the cushion effect of the separation bubble. Upstream of the separation point, however, the measured values were larger than the computed values of  $\Delta C_p$ , reflecting the possible contraction of the separation streamline due to the propeller.

## MEASURED AND COMPUTED THRUST DEDUCTION

As shown in Figures 13 and 14, the measured values of  $(C_p)_p$ ,  $(C_p)_b$ , and  $\Delta C_p = (C_p)_b - (C_p)_p$  were in good agreement with the computed values for Afterbodies 1 and 2. The agreement for  $\Delta C_p$  was less satisfactory for Afterbody 3 near the separation point of  $X/L = 0.92$  (Figure 15). These figures also show the values of  $t_p$  calculated from the integration of the measured values of  $\Delta C_p$  by using Equation (18).



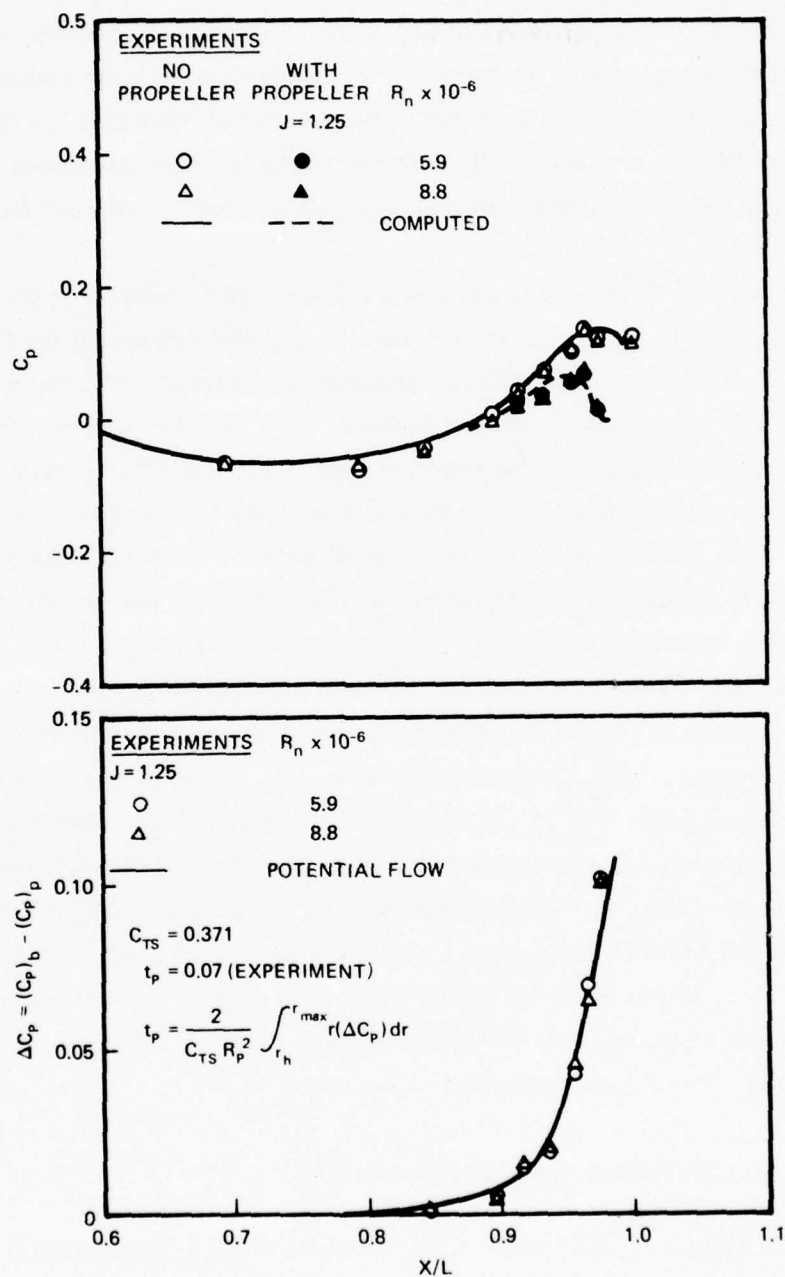


Figure 13 – Measured and Computed Pressure Distribution on Afterbody 1 with and without Propeller in Operation

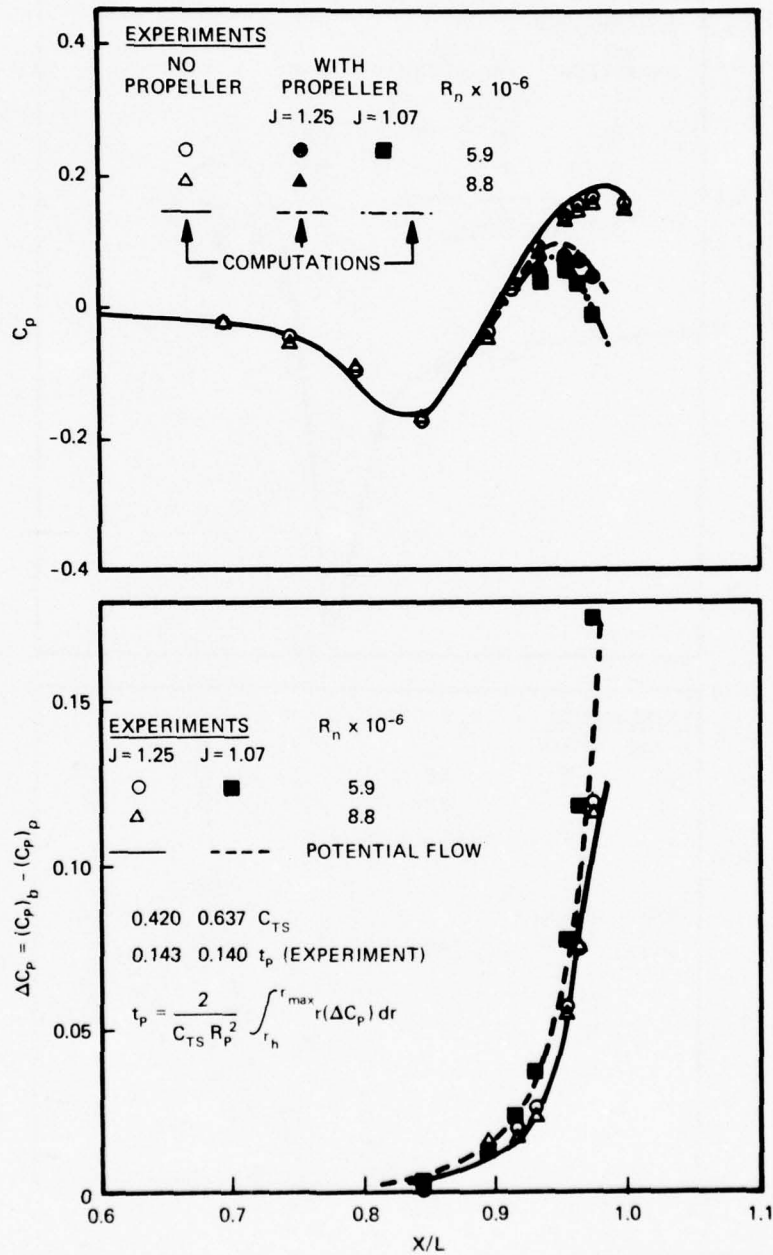


Figure 14 – Measured and Computed Pressure Distribution on Afterbody 2 with and without Propeller in Operation

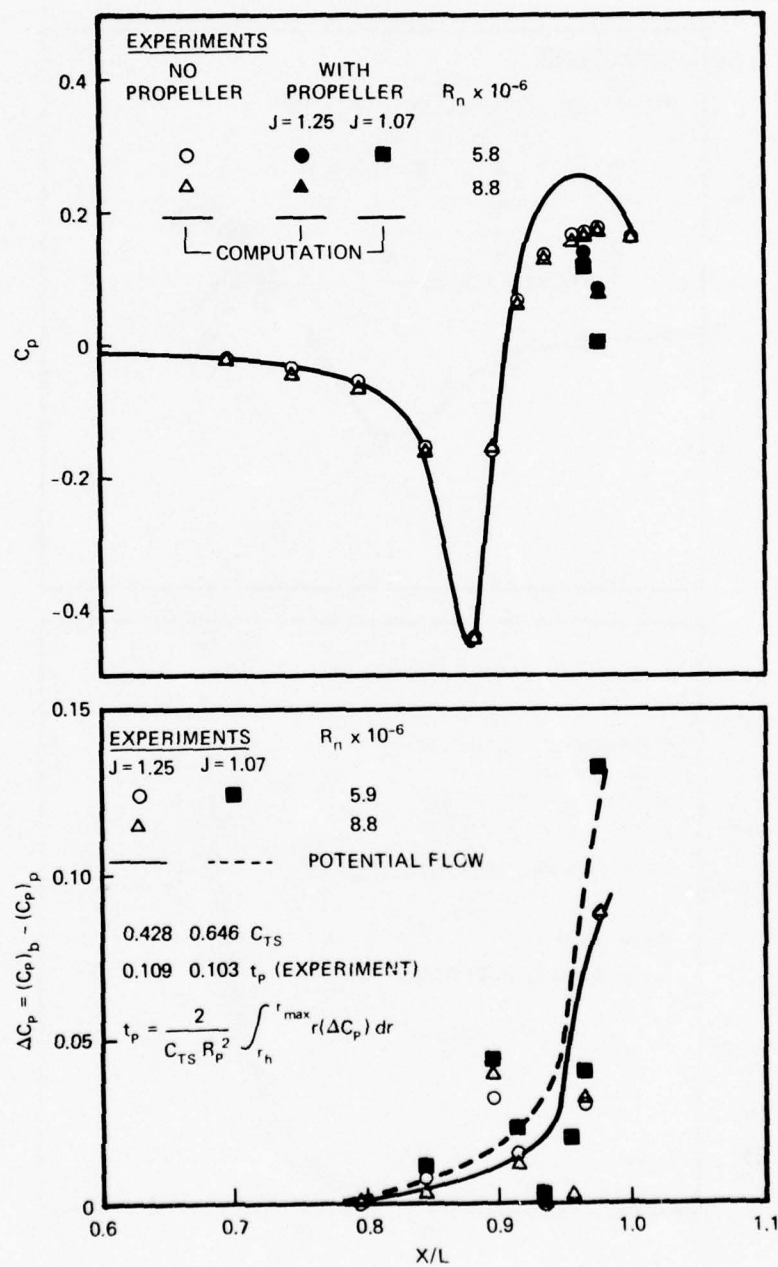


Figure 15 – Measured and Computed Pressure Distribution on Afterbody 3 with and without Propeller in Operation

The good agreement between the measured and computed values of  $\Delta C_p$  shown in Table 4 for Afterbodies 1, 2, and 3 indicates that the pressure component of thrust deduction can be well predicted by the potential-flow propeller-hull interaction approximation. However, if there is flow separation at the stern, the potential-flow interaction approximation for  $t_p$  should be used with caution. Although the computed value of  $t_p$  for Afterbody 3 agreed well with the measured value of  $t_p$  obtained from the interaction of the measured  $\Delta C_p$ , the latter did not agree very well with the computed  $\Delta C_p$  in the vicinity of the separation point (Figure 15).

The CS boundary-layer computation<sup>17</sup> can be performed with the new pressure distribution  $(C_p)_p$ . The measured and computed local shear stress distributions and the value of  $t_F$  computed by integration of measured values of  $\Delta C_{\tau_0}$  (by using Equation (19)) over the three afterbodies have already been shown in Figures 10-12. The measured value of  $t_p$  and  $t_F$  for the three afterbodies at  $R_n = 5.9 \times 10^6$  are summarized in Table 4.

**TABLE 4 - COMPARISON OF COMPUTED AND MEASURED THRUST DEDUCTION**

Configuration	Computed* $t_p$	Measured $t_p$	Measured $t_F$	Measured $t = t_p + t_F$	Measured $t_F/t_p$
Afterbody 1, $J = 1.25$	0.068	0.07	0.0024	0.0724	3.4%
Afterbody 2, $J = 1.25$	0.129	0.143	0.0023	0.1453	1.6%
Afterbody 2, $J = 1.07$	0.126	0.140	0.0026	0.1426	1.9%
Afterbody 3, $J = 1.25$	0.106	0.109	0	0.109	0
Afterbody 3, $J = 1.07$	0.103	0.103	0	0.103	0

\*The computed values of  $t_p$  were obtained by integration of the computed values of  $\Delta C_p$ .

Agreement was satisfactory between the computed and measured pressure components of thrust deduction  $t_p$ . The measured ratio  $t_F/t_p$  was less than 5 percent for the three afterbodies at  $J = 1.25$  and  $J = 1.07$ . Therefore, the value of thrust deduction  $t$  can be satisfactorily estimated from its pressure component  $t_p$  and its frictional component  $t_F$  can be neglected.

#### MEASURED AND COMPUTED AXIAL VELOCITY PROFILES

The mean axial velocity profiles in the boundary layers of the three afterbodies with and without a propeller in operation were measured by a laser doppler velocimeter. The boundary-layer profiles were also computed by the Douglas CS differential boundary-layer computer



program.<sup>13,17,30</sup> The pressure distributions calculated from the present potential-flow boundary-layer iteration scheme were used to compute the profiles for the bare hull. On the other hand, the pressure distributions calculated from the potential-flow propeller-hull interaction approximation, Equation (20), were used to compute the profiles with propeller in operation. The measured and computed mean axial velocity profiles are compared in Figures 16 to 19. The present approximations for the profiles with a propeller in operation were computed from the inviscid propeller/stern boundary-layer interaction approximation.

Figures 16a - 16e respectively show the measured and computed axial velocity profiles  $u_x/U_0$  for Afterbody 1 at  $X/L = 0.845, 0.915, 0.954, 0.964$ , and  $0.977$ . The agreement was reasonably good except at  $X/L = 0.977$  where the measured velocities were noticeably smaller than the computed velocities near the body in the absence of a propeller. The generally good agreement between measured and computed velocity profiles (except very close to the body) on Afterbody 1 is consistent with the good agreement between the measured and computed shear stress (Figure 10) and pressure distributions (Figure 8).

Corresponding data for Afterbody 2 at  $X/L = 0.935, 0.964$ , and  $0.977$  are shown in Figure 17. Agreement was good at  $X/L = 0.935$  but the measured velocities were progressively slower than the computed velocities as the end of the stern was approached. This discrepancy near the stern is consistent with that found between the measured and the computed shear stresses (Figure 11) and pressure distribution (Figure 8) on Afterbody 2. The present potential-flow boundary-layer iteration scheme is not adequate for handling the flow on a full afterbody with a small value of  $L_A/D$  (2.24) and with a strong adverse pressure gradient. However, the iteration scheme does provide a very good approximation of the stern flow for Afterbody 1 which has a mild adverse pressure gradient (Figure 2) and a moderate value of  $L_A/D$  (= 4.3).

Figure 18 shows only the measured axial velocity profiles at  $X/L = 0.963$  and  $0.977$  for Afterbody 2 with the propeller moved one-quarter propeller diameter ( $D_p/4$ ) aft of its original location at  $X/L = 0.983$ . Comparing Figures 17b and 17c with 18a and Figures 17d and 17e with 18b, one finds as expected that the velocity augmentation due to propeller suction is reduced by moving the propeller further downstream.

Figures 19a - 19e respectively show the measured and computed velocity profiles for Afterbody 3 at  $X/L = 0.795$  and  $0.915$  and only measured values at  $X/L = 0.934, 0.954$ , and  $0.977$ . The agreement was excellent at  $X/L = 0.795$  (Figure 19a) but only fair at  $X/L = 0.915$  (Figure 19b) immediately upstream of the separation point ( $X/L = 0.92$ ). It is also important to note that the measured axial velocity approached the free-stream velocity.

Figure 16 – Measured and Computed Axial Velocity Profiles on Afterbody 1 with and without Propeller in Operation at Different X/L Ratios and with  $R_n = 5.9 \times 10^6$

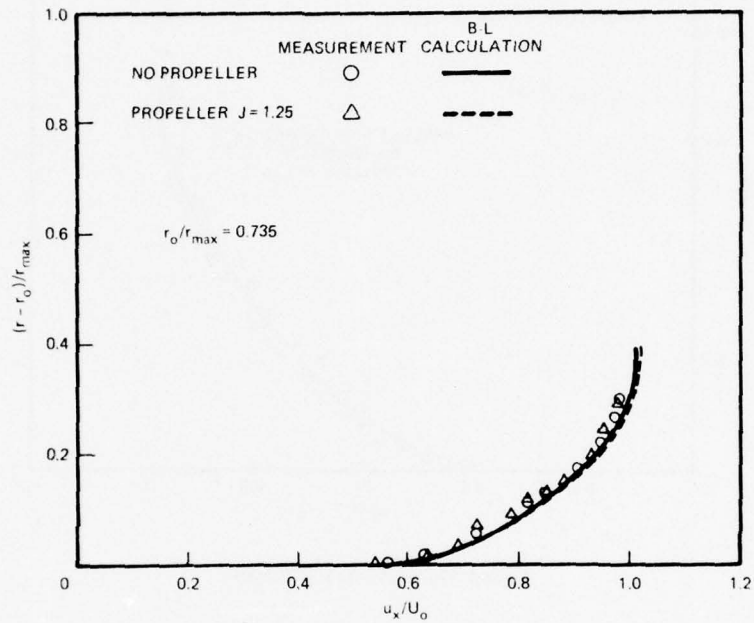


Figure 16a – At  $X/L = 0.845$

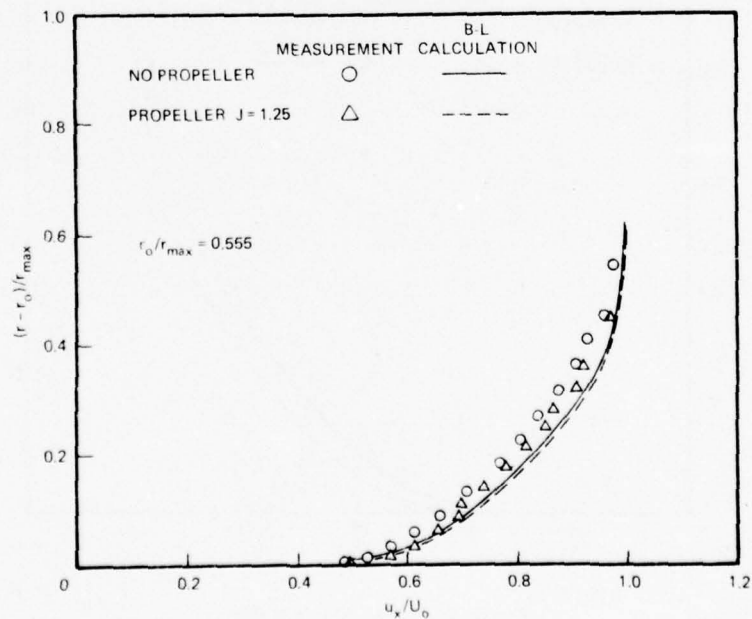


Figure 16b – At  $X/L = 0.915$

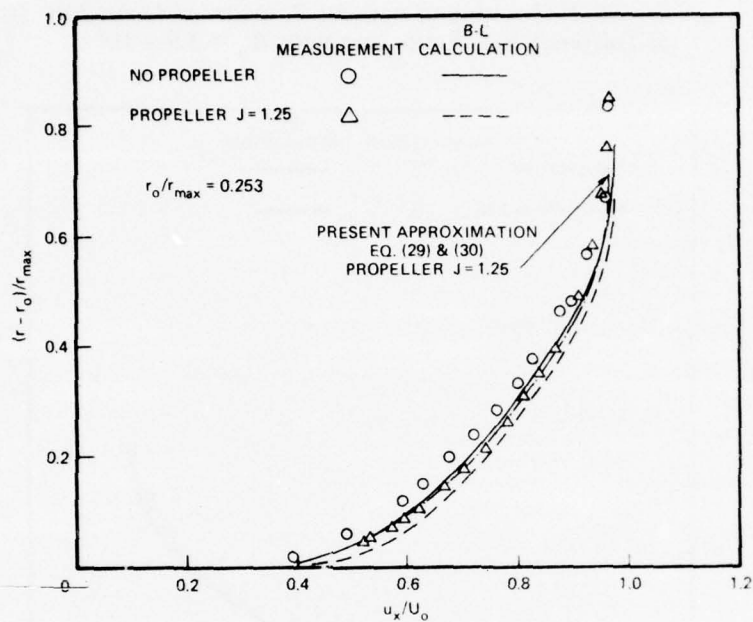


Figure 16c - At  $X/L = 0.954$

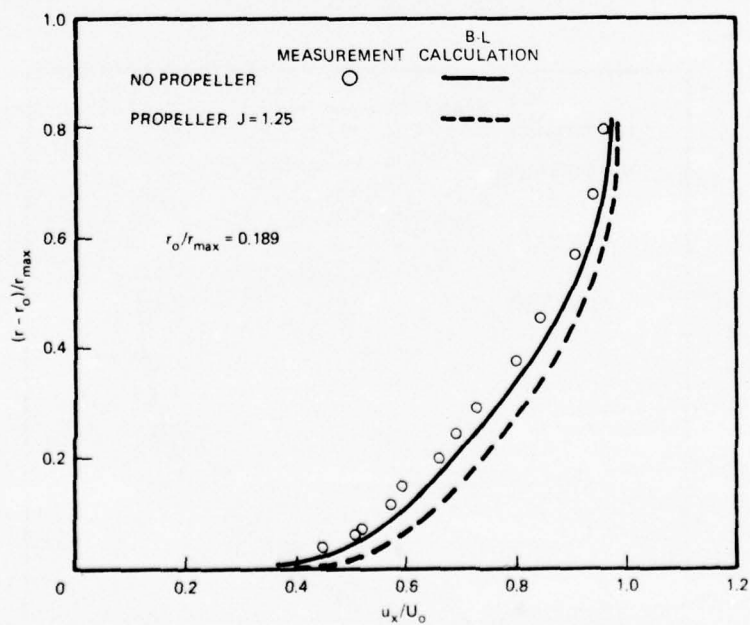


Figure 16d - At  $X/L = 0.964$

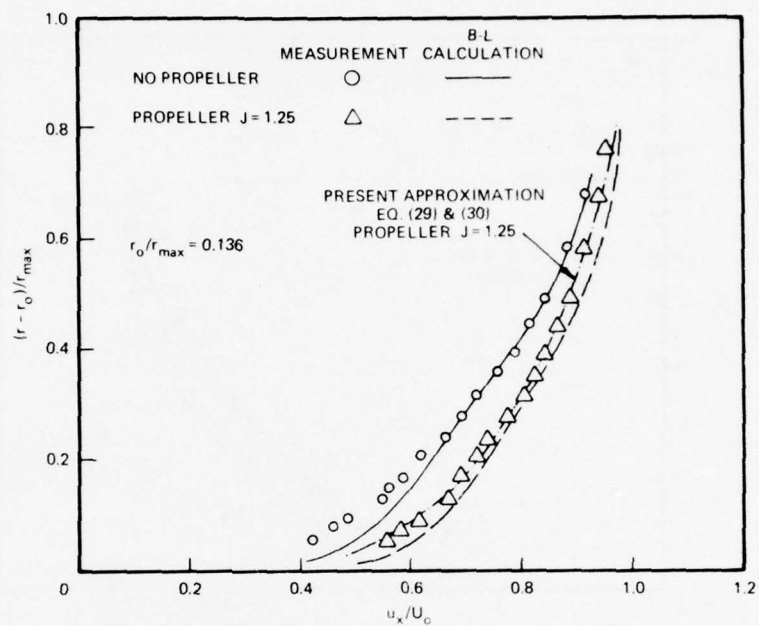


Figure 16e - At  $X/L = 0.977$

Figure 17 - Measured and Computed Axial Velocity Profiles on Afterbody 2 with and without Propeller in Operation at Different  $X/L$  Ratios and with  $R_n = 5.9 \times 10^6$

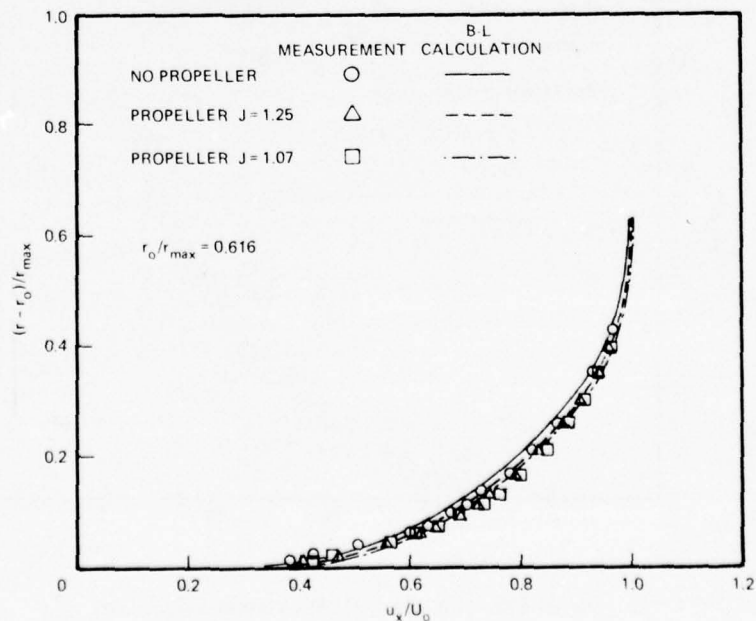


Figure 17a - At  $X/L = 0.935$



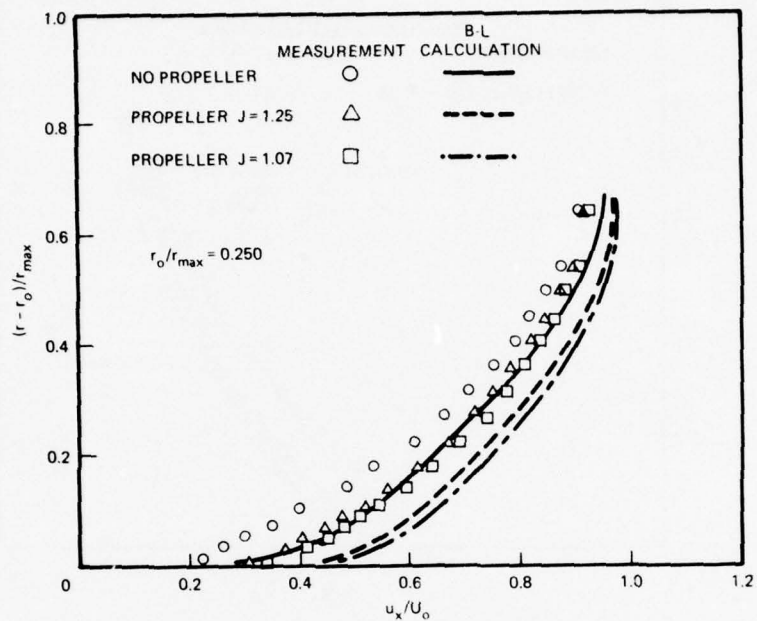


Figure 17b - At  $X/L = 0.964$ , B-L Calculation

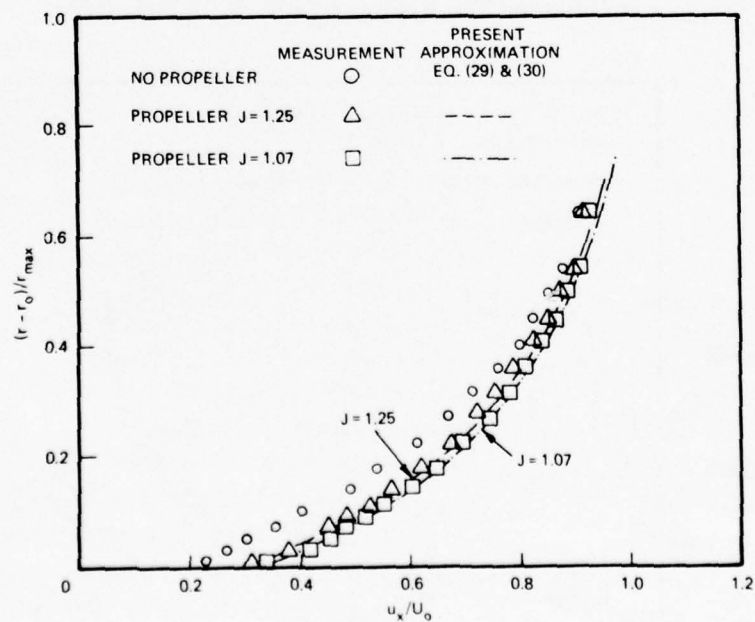


Figure 17c - At  $X/L = 0.964$ , Present Calculation

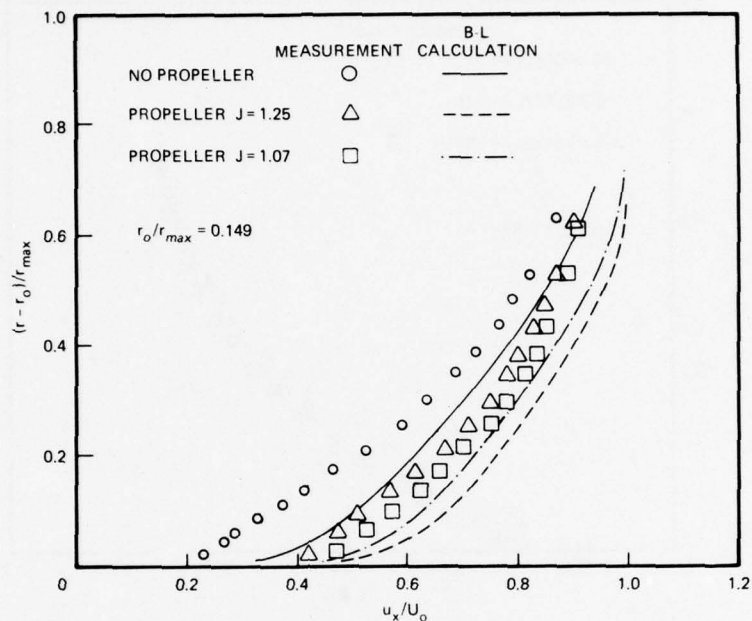


Figure 17d - At  $X/L = 0.977$ , B-L Calculation

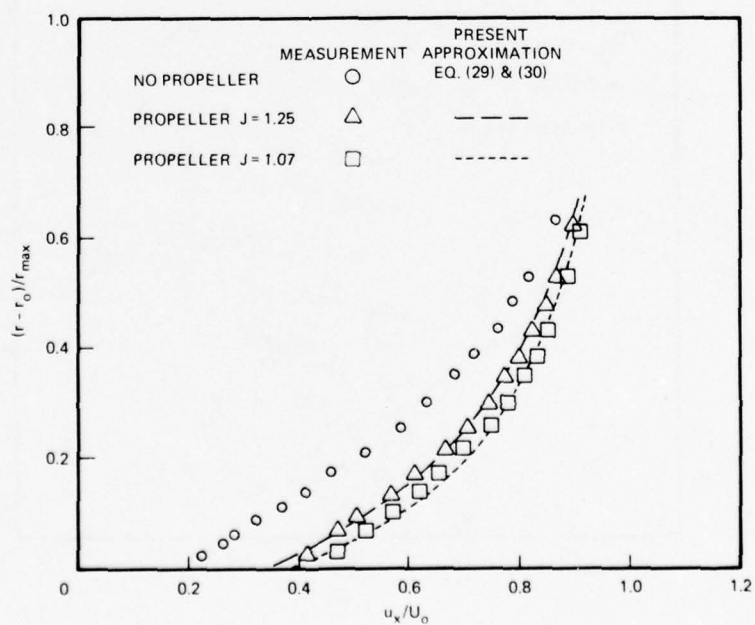


Figure 17e - At  $X/L = 0.977$ , Present Approximation

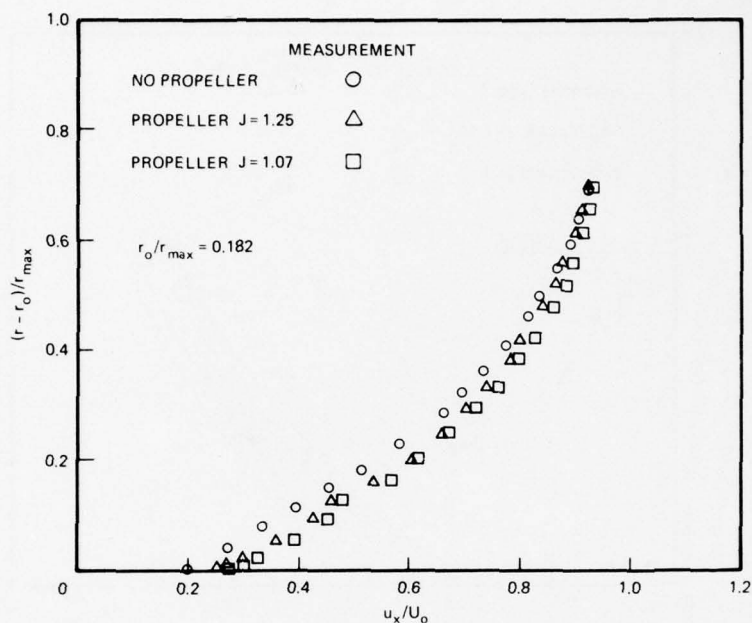


Figure 18a - At  $X/L = 0.963$

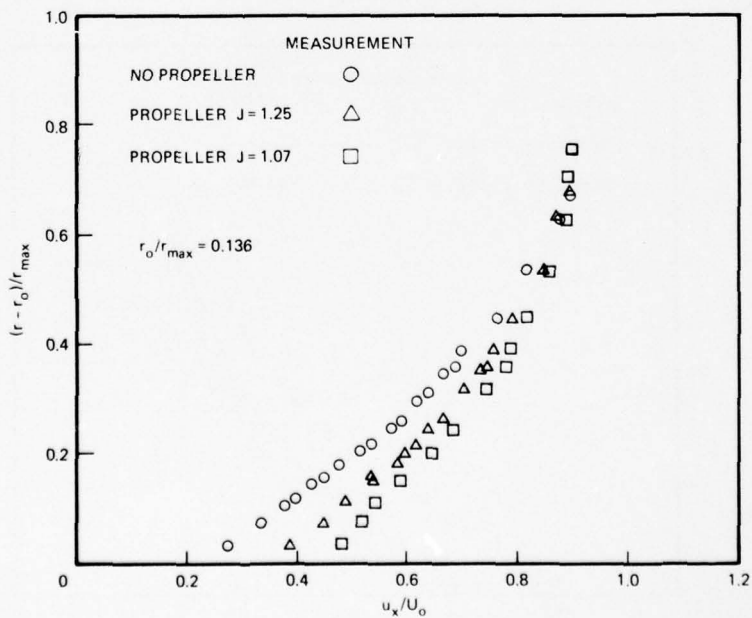


Figure 18b - At  $X/L = 0.977$

Figure 18 - Measured Axial Velocity Profiles on Afterbody 2 with Propeller Moved  $D_p/4$  Aft of Original Location

Figure 19 – Measured and Computed Axial Velocity Profiles  
on Afterbody 3 with and without Propeller in Operation  
at Different X/L Ratios and with  $R_n = 5.9 \times 10^6$

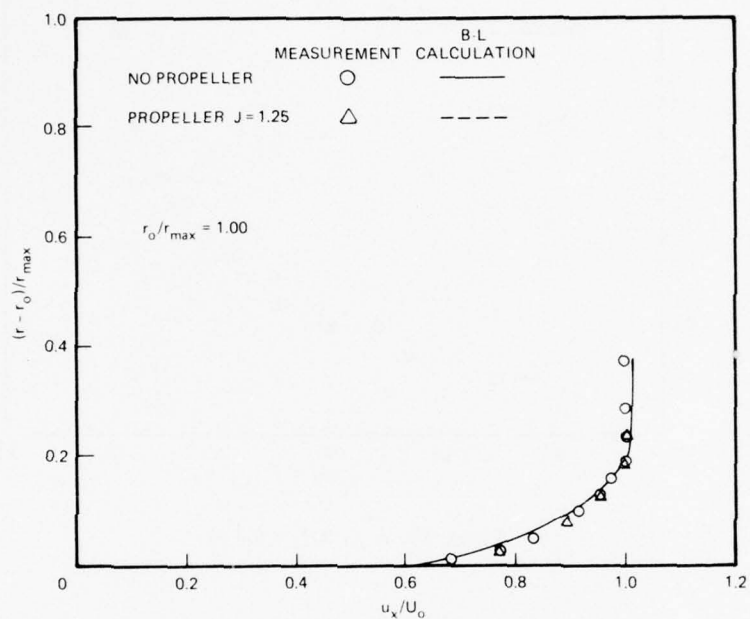


Figure 19a – At  $X/L = 0.795$

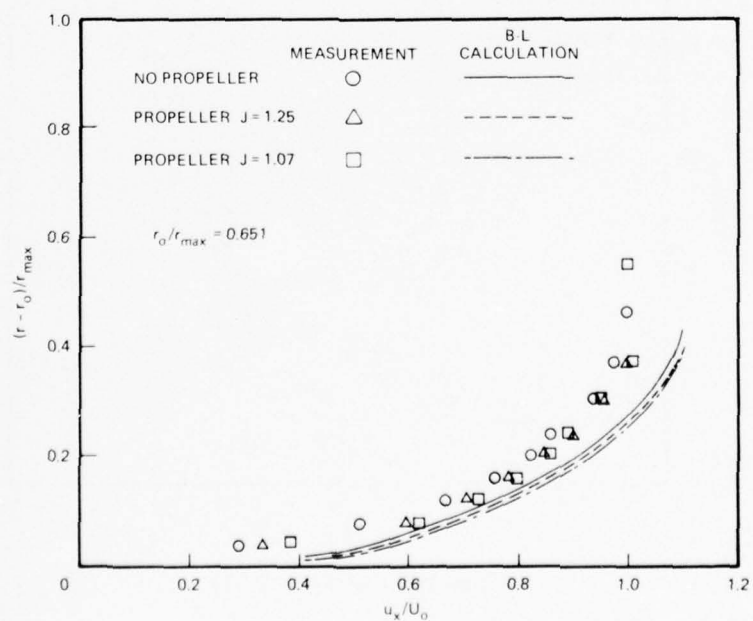


Figure 19b – At  $X/L = 0.915$



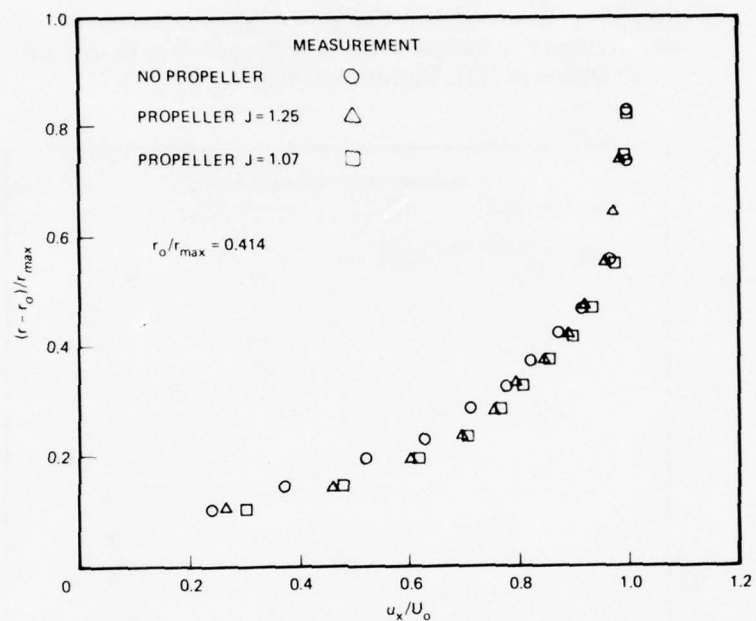


Figure 19c - At  $X/L = 0.934$

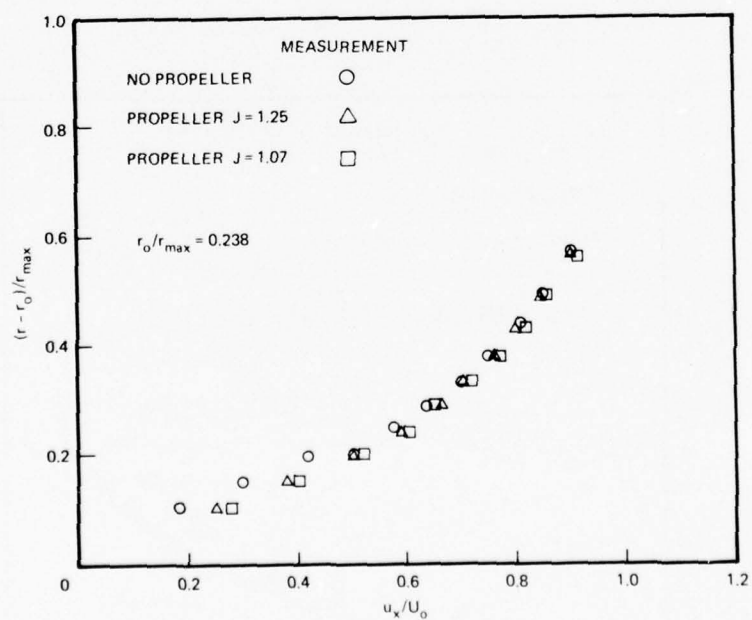


Figure 19d - At  $X/L = 0.954$

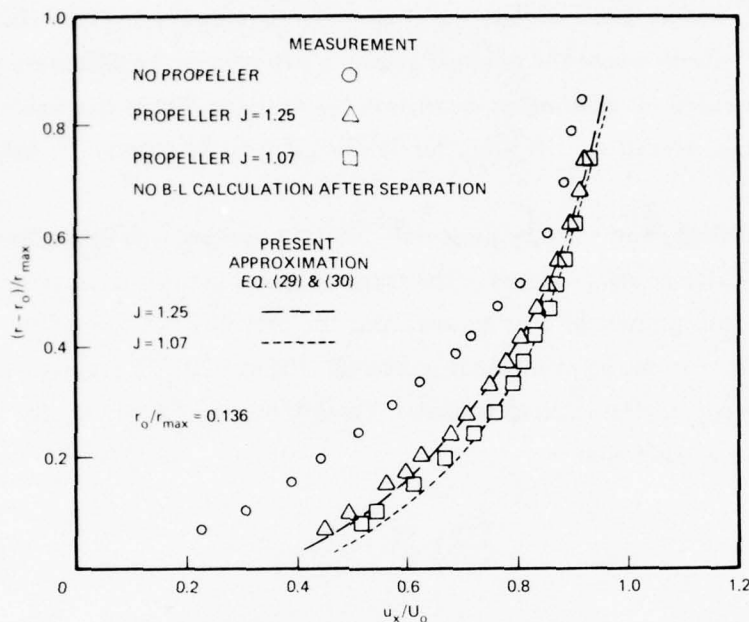


Figure 19e – At  $X/L = 0.977$

On the other hand, within the boundary-layer approximation, the computed axial velocity approached the local potential axial velocity on the body at the edge of the boundary layer. The separated flow reattached at  $X/L = 0.97$ . Since the CS boundary-layer computer program terminates computation when flow separation is encountered, no computed results are presented at  $X/L = 0.934$ ,  $0.954$ , and  $0.977$ . The effect of the propeller on the measured profiles at  $X/L = 0.934$  and  $0.954$  (Figures 19c and 19d) was relatively small, but it became significant at  $X/L = 0.977$  (Figure 19e) where the flow reattached after separation.

The fact that the effect of the propeller on the measured velocity profiles of the three afterbodies was limited to distances of two propeller diameters upstream of the propeller (Figures 18 and 19) was consistent with the measured effect of the propeller on shear stress (Figures 10–12) and pressure (Figures 13–15) distributions.

Let us briefly review data already presented for the measured and computed axial velocity profiles  $u_p(r)$  with the propeller in operation. Examine Figure 16c ( $X/L = 0.954$ ) and Figure 16e ( $X/L = 0.977$ ) for Afterbody 1, Figures 17b and 17c ( $X/L = 0.964$ ) and Figures 17d and 17e ( $X/L = 0.977$ ) for Afterbody 2, and Figure 19e ( $X/L = 0.977$ ) for Afterbody 3. Agreement between the measured and computed values of  $u_p$  was good for all of the cases. It is important to note that the propeller plane was at  $X/L = 0.983$  in all cases. The measurement stations were located at small distances from the propeller. The propeller field-point

velocity program<sup>31</sup> was used to calculate the circumferential-mean, propeller-induced axial velocities at the positions where the nominal and effective velocity profiles were measured. The change in the radial distribution of circulation for the propeller in the wakes of the three different afterbodies, needed for the propeller field-point velocity program,<sup>31</sup> has already been discussed.

The propeller field-point velocity program<sup>31</sup> has two options; one uses lifting-line theory and the other uses lifting-surface theory. The mean propeller-induced axial velocities  $u_a$  calculated by the two options differ somewhat near the propeller but the difference diminishes as distance from the propeller is increased. Figures 20 - 22 present the computed profiles  $u_a/U_o$  at various measurement stations. The difference in axial velocity with and without a propeller is defined as

$$\frac{\Delta u_x}{U_o} = \frac{u_p}{U_o} - \frac{u_x}{U_o}$$

The measured and calculated values of  $\Delta u_x/U_o$  at the various stations of the three afterbodies are also shown in Figures 20 - 22. As indicated in Figure 20a ( $X/L = 0.954, 0.58 D_p$  upstream of the propeller), the measured and calculated values of  $\Delta u_x/U_o$  were in good agreement and this was so even for the values of  $\Delta u_x/U_o$  calculated by the boundary-layer method, with the wall pressure distribution modified to account for the suction of the propeller. However, at  $X/L = 0.977 (0.12 D_p)$ , the values of  $\Delta u_x/U_o$  determined by the boundary-layer calculation did not agree well with the measured data (Figures 20b, 21c, and 21d). The present approximation with the lifting-surface option was in good agreement with all the measured data.

Thus, it may be concluded that the present inviscid approximation provides a good representation of the complex hydrodynamic interaction between the propeller and the stern boundary layer. The good agreement between the measured and computed values of  $\Delta u_x/U_o$  at small distances from the propeller suggests that the present approximation can be used with confidence to calculate the effective velocity profile for the propeller from the measured nominal velocity profile and a computed average propeller-induced axial velocity profile.

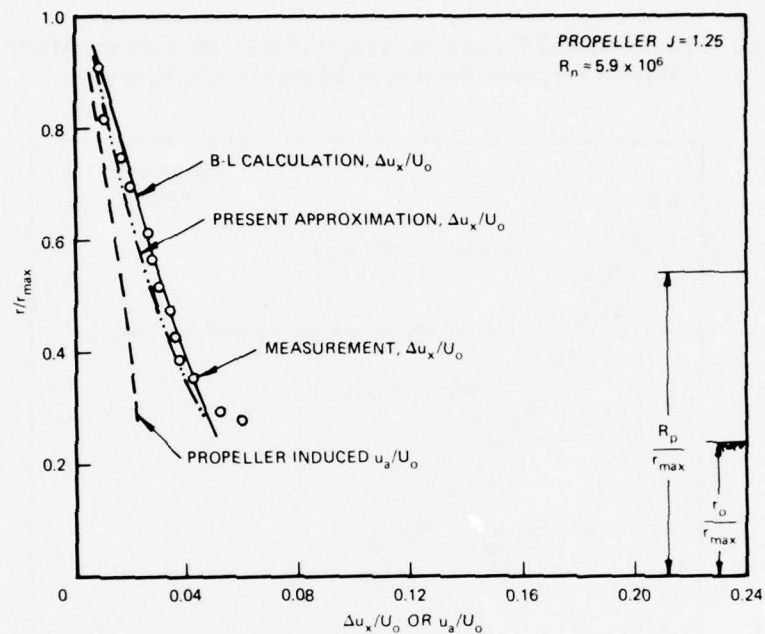


Figure 20a - At  $X/L = 0.954$

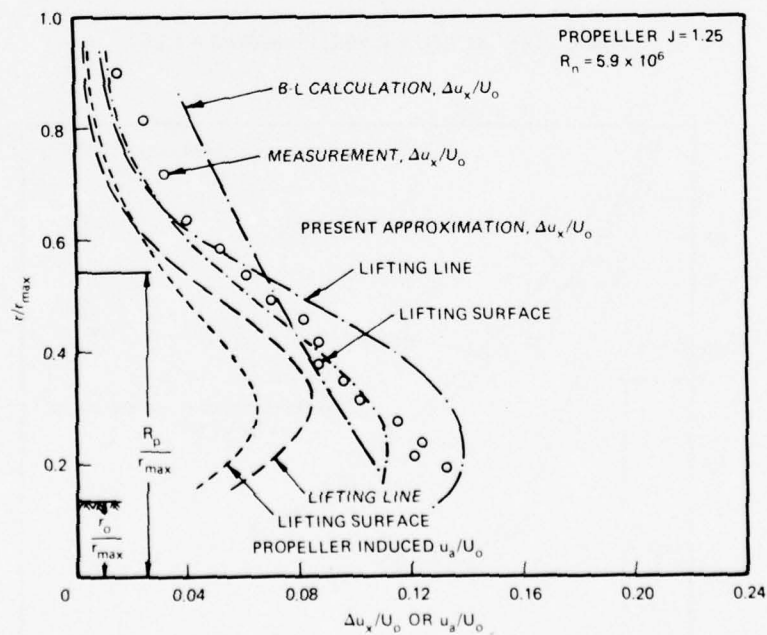
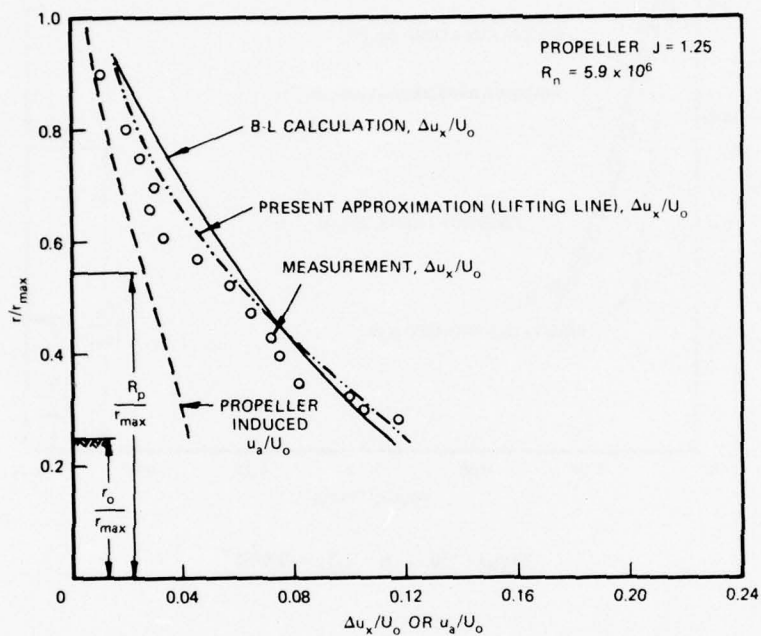


Figure 20b - At  $X/L = 0.977$

Figure 20 - Measured and Computed Axial Velocity Increase on Afterbody 1 Due to Propeller Suction at Different  $X/L$  Ratios



**Figure 21 – Measured and Computed Axial Velocity Increase on Afterbody 2  
Due to Propeller Suction at Different X/L Ratios**



**Figure 21a – At X/L = 0.964, Propeller J = 1.25**

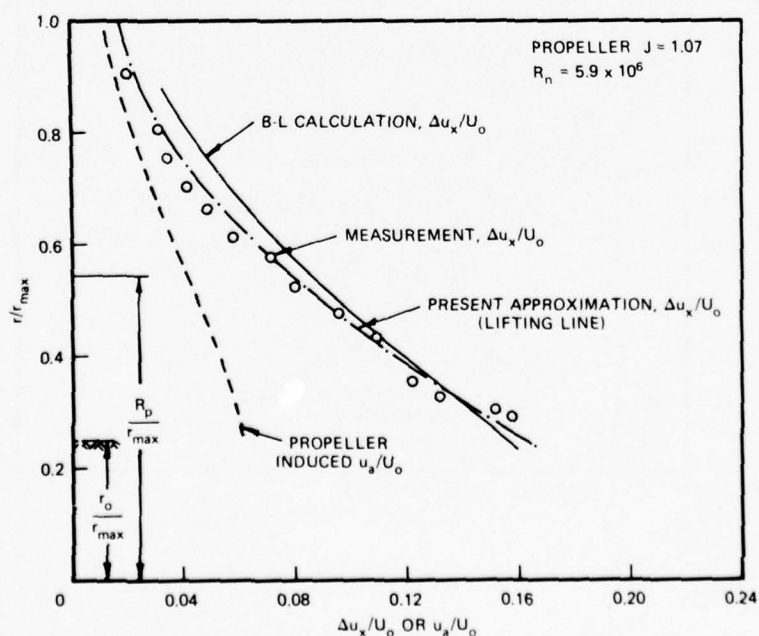


**Figure 21b – At X/L = 0.964, Propeller J = 1.07**

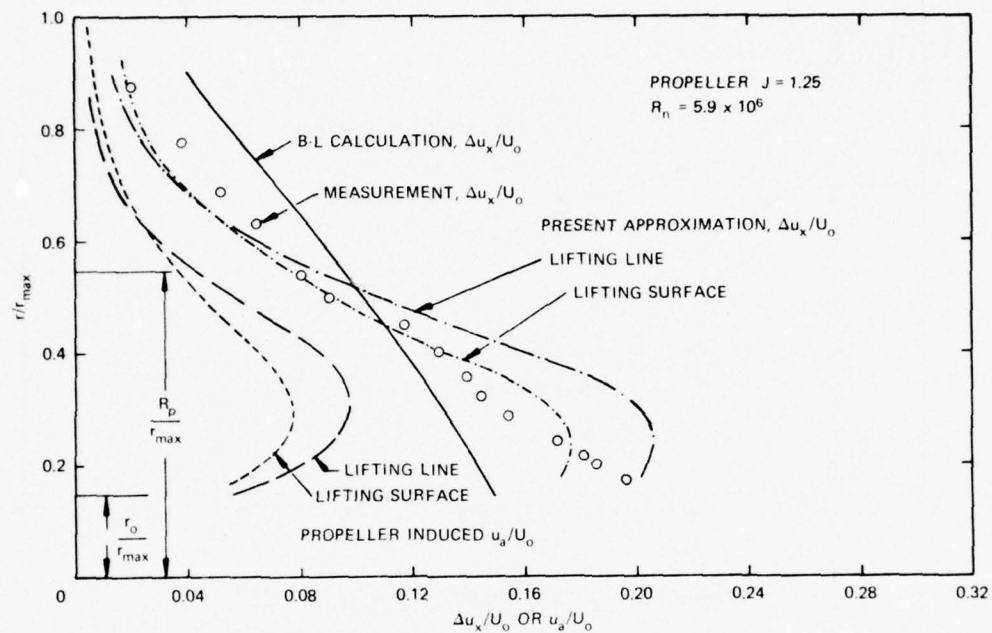


Figure 21c - At  $X/L = 0.977$ , Propeller  $J = 1.25$

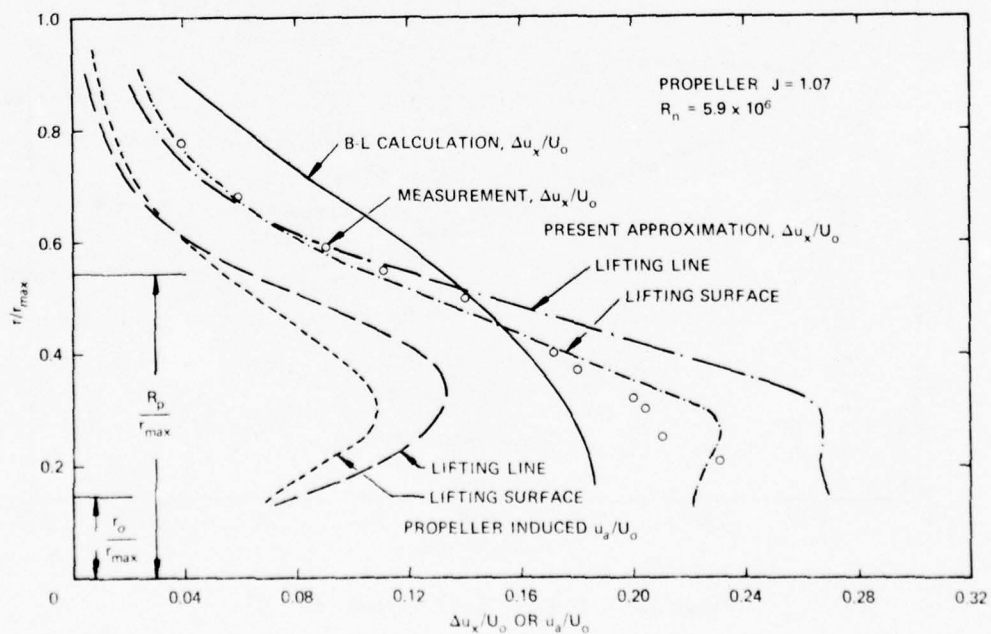


Figure 21d - At  $X/L = 0.977$ , Propeller  $J = 1.07$

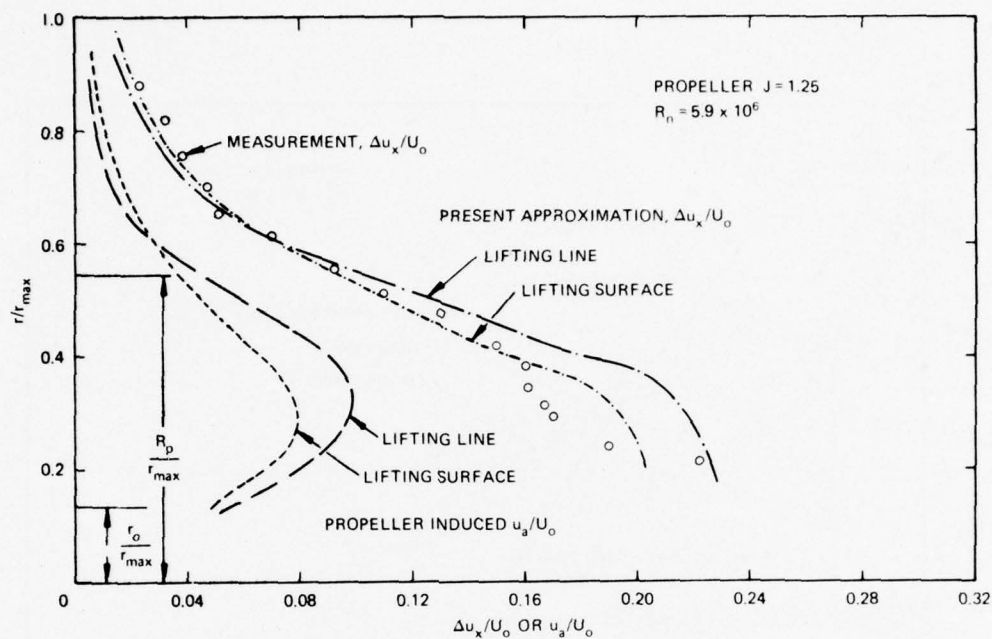


Figure 22a - At  $X/L = 0.977$ , Propeller  $J = 1.25$

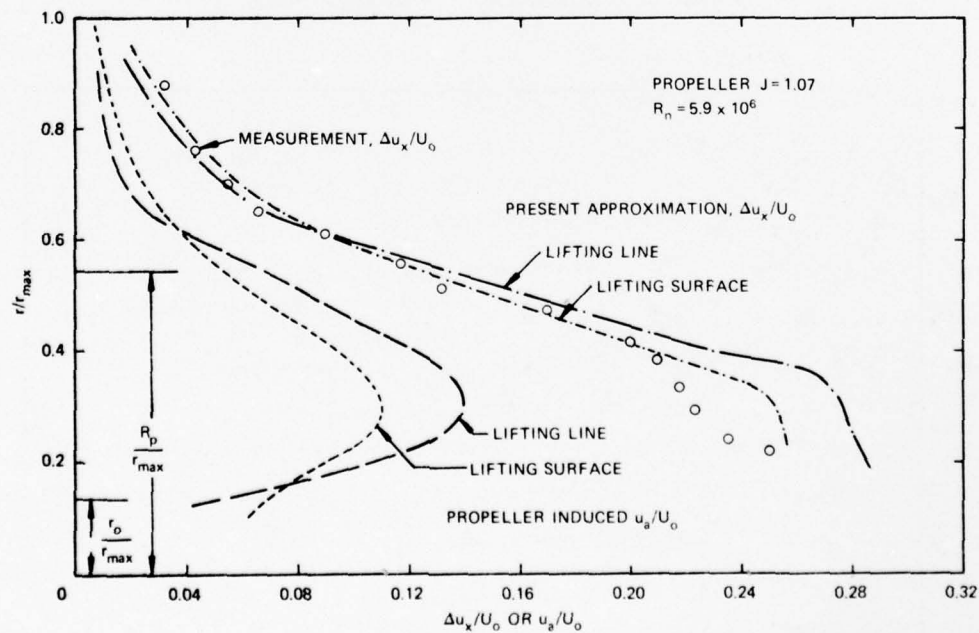


Figure 22b - At  $X/L = 0.977$ , Propeller  $J = 1.07$

Figure 22 - Measured and Computed Axial Velocity Increase on Afterbody 3 Due to Propeller Suction at  $X/L = 0.977$

## CONCLUSIONS

A comprehensive set of experimental data has been presented for three axisymmetrical afterbodies, two with attached flows and one with separated flow. In addition to enabling analytical techniques to be evaluated, these data also serve to give insight into the details of the flow in the stern region. The following conclusions were drawn:

1. The potential flow boundary-layer interaction program computed accurate values of pressure and shear stress on Afterbody 1 (which has a fine stern), gave less satisfactory predictions for Afterbody 2 (which has a fuller stern) and were in only fair agreement for Afterbody 3 (which separates at  $X/L = 0.92$ ).
2. For all sterns, the agreement between computed and measured velocity profiles was excellent up to about  $X/L = 0.9$ . Thereafter, the agreement progressively worsened as the tail was approached, particularly for Afterbody 3. These results suggest that the modeling of the wake should be modified to handle cases of separated flow and that the boundary-layer equations should be modified to properly model the thick stern boundary layer.
3. In most cases, the propeller stern boundary-layer interaction program predicted reasonably accurate effective velocity profiles. The difference between the computed effective and nominal velocity profiles was largest at the propeller hub and became smaller at the propeller tip. This is in contrast to results obtained by the conventional method wherein the effective wake is scaled up or down from the nominal wake by a constant factor, a procedure which usually yields the largest difference between the effective and nominal velocity profiles at the propeller tip. Since the present experimental results compared well with the present theory, it is concluded that the constant-factor method is not satisfactory and should no longer be used for bodies of revolution. The present theory takes as input the measured nominal velocity profile without the propeller in operation and uses standard propeller computer codes for computing propeller blade loading and induced field-point velocities.
4. The use of lifting-surface theory to predict the induced field-point velocities usually gives more accurate effective velocity profiles than provided by lifting-line theory.
5. When propeller-induced pressure distribution is used to calculate velocity profiles near the propeller by the CS boundary-layer method, predictions usually deviate substantially from the measured velocity profiles in the presence of a propeller.
6. The experimental results show that the potential-flow propeller-hull interaction methods predict thrust deduction and the propeller-induced pressure distribution very well.



### **ACKNOWLEDGMENTS**

The authors express their gratitude to Mr. Justin H. McCarthy who introduced the problem to them. His guidance, enthusiasm, and continuous support during the course of this investigation contributed greatly to the project as a whole. The authors would also thank Dr. Bruce D. Cox and Mr. Thomas A. Lafone for their assistance in applying propeller theories and computer programs, Dr. William B. Morgan for his advice in understanding propeller theories, Dr. Allen G. Hansen for providing thrust deduction calculations, and Mr. Ray Hollowell and the staff of the DTNSRDC anechoic flow facility for their effective experimental support.

## APPENDIX

### OFF-AXIS DUAL-BEAM BACKSCATTER LASER DOPPLER VELOCIMETER

A focal length of 1.5 m was selected for the LDV optics so that the entire optical bench could be located in the quiescence region of the anechoic chamber. The selection of a beam separation of 99 mm with a total beam angle of 3.722 deg was based on the desired size of probe volume.

As shown in Figure 23, the collimated beam emitted by a multicolor argon-ion laser (Coherent Radiation Model CR-3) is tuned to emit green ( $\lambda = 5145 \text{ \AA}$ ) light and is polarized parallel to the x-axis by a polarization rotator. Such polarization is necessary to ensure maximum scatter intensity.<sup>37</sup> A beam splitter separates the beam into two equal-intensity parallel beams with a separation of 50 mm. The beams are separated further by prisms to a final separation of 99 mm. A 15.24-cm-diameter lens is used to focus the two parallel beams at probe volume. The focal diameter for a diffraction-limited system is given<sup>38,39</sup> by

$$2b_o = \frac{4}{\pi} \frac{FL}{2b} \lambda$$

Here  $b_o$  is the radius of the focused beam,  $b$  is the radius of the unfocused beam,  $\lambda$  is the wave length of the laser, and  $FL$  is the focal length of the focusing lens. Since each beam can be assumed to have a Gaussian intensity distribution, the probe volume will be ellipsoidal in shape and have the following dimensions:

$$\Delta X = \frac{2b_o}{\cos\left(\frac{\theta}{2}\right)} = 0.491 \text{ mm}$$

$$\Delta Y = 2b_o = 0.491 \text{ mm}$$

$$\Delta Z = \frac{2b_o}{\sin\left(\frac{\theta}{2}\right)} = 15.09 \text{ mm}$$

<sup>37</sup>Born, M. and E. Wolf, "Principles of Optics," Pergamon Press, New York (1965), p. 652.

<sup>38</sup>Goethert, W.H. and D.B. Brayton, "New Velocity Measuring Technique Using Dual Scatter Laser Doppler Shift," Arnold Engineering Development Center AEDC-TR-205 (1970).

<sup>39</sup>Yanta, W.J., "Turbulence Measurements with a Laser Doppler Velocimeter," Naval Ordnance Laboratory NOLTR-73-94 (1973).

Here  $\Delta X$  is in the direction of the mean flow,  $\Delta Y$  is perpendicular to the mean flow, and  $\Delta Z$  is in the bisector of the beam angle. The parameters for the laser and optics are as follows:

$$\lambda = 5145 \text{ \AA}$$

$$2b = 2.0 \text{ mm at } 1/e^2 \text{ with beam expander}$$

$$FL = 1500 \text{ mm}$$

$$\theta = 3.722 \text{ deg}$$

The large size of  $\Delta Z$  is primarily due to the beam angle  $\theta$  which is the ratio of lens diameter to its focal length. The present choice of lens diameter (15.24 cm) was limited mainly by expense since the cost of the lens increases drastically with increasing diameter. The back-scattered radiation was collected vertically off axis ( $\cong 28 \text{ deg}$ ) by a 15.24-cm-diameter lens which focuses the scattered light onto a photomultiplier tube. This off-axis dual-beam back scatter mode of operation was chosen to reduce the background noise from the radiation of the two long transmitting beams; it can also be used to reduce the effective length of the long axis of probe volume  $\Delta Z$ . An effective  $\Delta Z$  of 5 mm can be achieved by carefully focusing the receiving optics on the center portion of the volume.

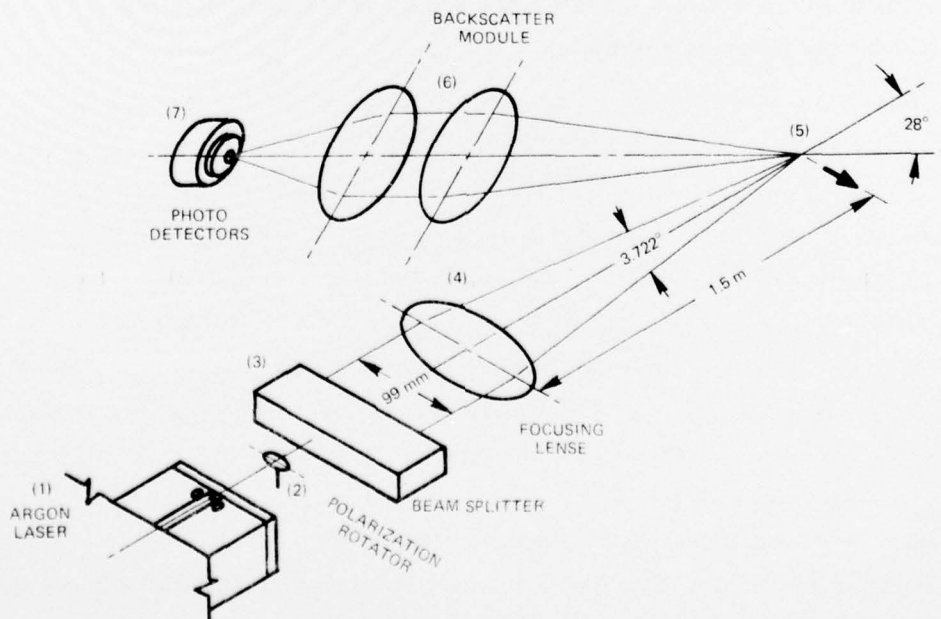


Figure 23 – Off-Axis, Dual-Beam Backscatter Optics

In view of the coherence characteristics of the laser light, the two beams will interface constructively and destructively to establish a set of closely spaced, planar interference fringes at the probe volume. The peak-to-peak fringe spacing  $d_o$  is

$$d_o = \frac{\lambda}{2 \sin\left(\frac{\theta}{2}\right)} = 7.9 \mu\text{m}$$

The number of fringes contained in a probe volume can be determined by dividing the peak-to-peak fringe spacing into the focal diameter  $\Delta X$  as follows:

$$N = \frac{\Delta X}{d_o} = \frac{4 b_o}{\lambda} \tan\left(\frac{\theta}{2}\right) = \frac{4}{\pi} \frac{2 FL}{2b} \tan\left(\frac{\theta}{2}\right) = \frac{4}{\pi} \frac{\text{beam separation}}{2b}$$

where beam separation  $= 2 FL \tan(\theta/2) = 99 \text{ mm}$  and  $2b = 2 \text{ mm}$ . Thus, the total number of fringes in the probe volume is  $N = 63$ , which is sufficient for the present purpose ( $N$  must be greater than 10).

As a particle traverses the probe volume at a velocity  $U_x$ , the interference fringes are cut at a rate of

$$\frac{1}{f} = \frac{d_o}{U_x} = T, \quad f = \frac{2 U_x \sin\left(\frac{\theta}{2}\right)}{\lambda}, \quad \text{or} \quad U_x = \frac{\lambda}{2 \sin\left(\frac{\theta}{2}\right)} \frac{1}{T}$$

where  $T$  is the period of Doppler frequency  $f$ . The unique feature of this dual-beam scatter technique is that it is possible to place the receiving optics in any position since the view direction does not affect the measurement. It should be noted that forward scatter has a higher signal-to-noise ratio; however, the mechanical difficulty associated with placing the transmitting and receiving optics 3 m apart on an optical bench prevented the use of forward scatter techniques for this experiment. The off-axis dual-beam backscatter technique was used as a tradeoff between mechanical difficulty and optical difficulty.

In order to produce satisfactory backscatter radiation, it was necessary to seed the boundary layer with a fine oil mist; the mist was generated by a standard atomizer with a Laskin nozzle<sup>29</sup> and oil was emitted from an orifice at the model bow. The size of the particles generated varied between 1 to 10  $\mu\text{m}$ , peaking at about 5  $\mu\text{m}$ ; this was very satisfactory compared to the fringe spacing of 7.9  $\mu\text{m}$ .

The backscatter radiation of these particles cutting through the fringes was detected by a photomultiplier operated at a 1400-V potential. The signals from the photomultiplier were filtered and amplified, and were then processed by a laser Doppler digital data processor



(Arnold Research Organization, Inc. Model 8) which has been described in detail by Kalb.<sup>40</sup> The raw data were recorded on a Hewlett-Packard Model 5055A Digital Printer, which allowed a maximum data rate of 10 points per second.

For completeness, a general operating procedure will be given for the counter-type digital data processor (DDP). Before the Doppler frequency or "frequency-burst" signal can be processed, several tasks must be performed. The "pedestal" voltage and other gross low frequency baseline shifts must be filtered out along with noise above and below the frequency range of interest. The pedestal voltage arises because of unequal beam intensities, or polarization of the two beams, or because the particle does not pass through the geometrical center of the scattering volume. This pedestal voltage is removed by a band-pass filter applicable to the signal frequency of interest. The nine bands of the DDP each cover  $2\frac{1}{2}$  octaves; together they provide wide frequency coverage from 15 kHz to 50 MKz. An oscilloscope-triggered gate is used to synchronize the processor sampling interval with the burst signal event displayed on the oscilloscope.

The DDP employs high-speed, emitter-coupled integrated circuit flip-flops to convert the first eight pulses of Doppler frequency data into a square waveform with the same frequency as the original burst signal. The processor then digitizes the resultant time interval via period counter techniques. The DDP then uses high-speed digital computing circuitry to test the data pulse train for periodicity. It compares the time interval of both four and five data pulses to the time interval of eight data pulses. The two-stage time interval comparison enhances the accuracy of the Doppler readings, especially when sampling low signal-to-noise data. The use of both  $4/8$  and  $5/8$  time interval comparators significantly reduces alias or false readings caused by pulse dropouts and pulse additions. The DDP has a switchable error band available with 0.78, 1.5, and 3.0 percent for both  $4/8$  and  $5/8$  time interval comparators. If the errors of the two comparators are within the error band chosen, the data are accepted for recording in the form of natural binary for a minicomputer or magnetic tape recorder or in the form of binary code decimal for conventional digital printers.

After validation, data are accepted by the data acquisition system which, in turn, releases the recycle sequence switch and issues a zero reset pulse to all counters. At reset pulse termination, the processor must further await the reception of a +A gate signal from the oscilloscope before a new sample interval may begin. The recycle sequence is altered when the errors of one or both comparators exceed the error band chosen. A "data reject" signal

<sup>40</sup>Kalb, H.T. et al., "Laser Velocimetry Data Processing," Arnold Engineering Development Center AEDC-TR-73-116 (1973).

will then be issued by the comparator. All counters are reset to zero, the invalid data will be inhibited, and the data will not be transferred to the data acquisition system. A new data processing cycle will be initiated.

The valid data from DDP were printed by a digital printer (Hewlett-Packard Model 5055A) at a rate of about 10 points per second. At each profile location of the boundary layer, 200 to 400 Doppler data points were taken and used as input to the CDC 6700 digital computer. The instantaneous velocity  $u_{xi}$  was calculated from the instantaneous Doppler period  $T_i$  via

$$u_{xi} = \frac{\lambda}{2 \sin\left(\frac{\theta}{2}\right)} \frac{1}{T_i}$$

It is important to note that there is statistical bias in the time-average mean velocity as calculated from the individual velocity data point realizations from the output of the data processor. On the average, the scattering particles may be assumed to distribute uniformly throughout the flow. Over a long interval of time, particles moving faster than the time-average velocity will be detected more frequently than slower velocity particles since the probability of detecting a particle is proportional to the volume of fluid swept through the probe volume. Reischman and Tiederman<sup>41</sup> have shown that an improved estimate of the time-average velocity can be made by weighting each velocity realization  $u_{xi}$  with a function which is inversely proportional to the volume flow through the probe volume at that instant. To account for this fact, an improved estimate of the time-average mean velocity proposed by Reischman and Tiederman<sup>41</sup> has been adopted here:

$$\bar{U}_x = u_x = \frac{\sum_{i=1}^N u_{xi} \left(\frac{1}{u_{xi}}\right)}{\sum_{i=1}^N \left(\frac{1}{u_{xi}}\right)} = \frac{\lambda N}{2 \sin\left(\frac{\theta}{2}\right)} \bigg/ \left(\sum_{i=1}^N T_i\right)$$

Here  $u_{xi}$  is inversely proportional to  $T_i$  which is a direct output of the DDP. A complete accuracy analysis of the present laser Doppler velocimeter system has not been made. However, during many repeated runs in the course of the experiment, it was found that the standard deviations of the measured  $u_x$  were less than  $0.02 U_0$ .

<sup>41</sup>Reischman, M.M. and W.G. Tiederman, "Laser-Doppler Anemometer Measurements in Drag Reducing Channel Flows," Journal of Fluid Mechanics, Vol. 70, Pt 2, pp. 369-382 (1975).

## REFERENCES

1. Beveridge, J.L., "Analytical Prediction of Thrust Deduction for Submersibles and Surface Ships," *Journal of Ship Research*, Vol. 13, No. 4, pp. 258-271 (1969).
2. Weinblum, G.P., "The Thrust Deduction," *Journal of American Society of Naval Engineers*, Vol. 63, pp. 363-380 (1951).
3. Aintsberg, H., "Investigations on the Interaction between Hull and Propeller of Bodies of Revolution," (in German), *Jahrbuch der Schiffbautechnischen Gessellschaft*, Vol. 54, pp. 117-152 (1960); also available as David Taylor Model Basin Translation 309 (1965).
4. Tsakonas, S. and W.R. Jacobs, "Potential and Viscous Parts of the Thrust Deduction and Wake Fraction for an Ellipsoid of Revolution," *Journal of Ship Research*, Vol. 4, No. 2, pp. 1-16 (1960).
5. Nowacki, H., "Potential Wake and Thrust Deduction Calculations for Ship-Like Bodies," *Jahrbuch der Schiffbautechnischen Gessellschaft*, Vol. 57, pp. 330-363 (1963).
6. Nowacki, H. and S.D. Sharma, "Surface Effects in Hull Propeller Interaction," The Ninth Office of Naval Research Symposium on Naval Hydrodynamics, Paris, France (Aug 1972); available in U.S. Government Printing Office, ACR-203, Vol. 2, pp. 1845-1961 (1972).
7. Hucho, W.-H., "On the Effect of a Stern Propeller on the Pressure Distribution and the Boundary-Layer of an Afterbody of Revolution," *Institut für Strömungsmechanik der Technischen Hochschule Braunschweig*, Bericht 64/65, Pt II (1965).
8. Massaki Namimatsu and Moraoka Kenji, "Wake Distribution of Full Form Ships," *Engineering Review (Japan)*, Vol. 7, No. 3 (1975).
9. Kempf, G., "Wirbelablosung bei Volligen Schiffsformen," *Schiff und Hafen*, Vol. 6, No. 7, pp. 407-408 (1954).
10. Granville, P.S., "Geometrical Characteristics of Noses and Tails for Parallel Middle Bodies," *NSRDC Report 3763* (1972).
11. Hess, J.L. and A.M.O. Smith, "Calculation of Potential Flow about Arbitrary Bodies," in "Progress in Aeronautical Sciences," Vol. 8, Pergamon Press, New York (1966), Chapter 1.
12. Kerney, K.P. and N.M. White, "Description and Evaluation of a Digital-Computer Program for Calculating the Viscous Drag of Bodies of Revolution," *DTNSRDC Report 4641* (1975).
13. Cebeci, T. and A.M.O. Smith, "Analysis of Turbulent Boundary Layers," Academic Press, New York (1974), pp. 329-384.
14. Huang, T.T. and C.H. von Kerczek, "Shear Stress and Pressure Distribution on a Surface Ship Model: Theory and Experiment," The Ninth Office of Naval Research Symposium on Naval Hydrodynamics, Paris, France (Aug 1972); available in U.S. Government Printing Office, ACR-203, Vol. 2, pp. 1963-2010 (1972).

15. Lighthill, M.J., "On Displacement Thickness," *Journal of Fluid Mechanics*, Vol. 4, Pt 4, pp. 383 - 392 (1958).
16. Beatty, T.D., "A Theoretical Method for the Analysis and Design of Axisymmetric Bodies," National Aeronautics and Space Administration CR-2498 (1975).
17. Cebeci, T. et al., "Calculation of Viscous Drag and Turbulent Boundary-Layer Separation on Two-Dimensional and Axisymmetric Bodies in Incompressible Flows," Douglas Aircraft Report MDC J0973-01 (1970).
18. Beveridge, J.L., "Pressure Distribution on Towed and Propelled Streamlined Bodies of Revolution at Deep Submergence," David Taylor Model Basin Report 1665 (1966).
19. Myring, D.F., "The Profile Drag of Bodies of Revolution in Subsonic Axisymmetric Flow," Royal Aircraft Establishment (Great Britain) Technical Report 72234 (1972).
20. Lyon, H.M., "Effect of Turbulence on Drag of Airship Models," Aeronautical Research Committee (Great Britain) Reports and Memoranda 1511 (1932).
21. Lyon, H.M., "A Study of the Flow in the Boundary Layer of Streamlined Bodies," Aeronautical Research Committee Reports and Memoranda 1622 (1934).
22. Freeman, H.B., "Pressure Distribution Measurements on the Hull and Fins of a 1/40-Scale Model of the US Airship 'Akron'," National Advisory Committee for Aeronautics Report 443 (1932).
23. Nakayama, A., "Viscid-Inviscid Interaction Due to the Thick Boundary Layer near the Tail of a Body of Revolution," Ph.D. Thesis, University of Iowa (1974).
24. Patel, V.C. et al., "Measurements in the Thick Axisymmetric Turbulent Boundary Layer near the Tail of a Body of Revolution," *Journal of Fluid Mechanics*, Vol. 63, Pt 2, pp. 345 - 367 (1974).
25. Brune, G.W. et al., "The Analysis of Flow Fields with Separation by Numerical Matching," Symposium on Flow Separation, Advisory Group for Aerospace Research and Development, Germany (1975).
26. Granville, P.S., "The Calculation of the Viscous Drag of Bodies of Revolution," David Taylor Model Basin Report 849 (1953).
27. Smith, A.M.O. and J. Pierce, "Exact Solution of the Neumann Problem. Calculation of Non-Circulatory Plane and Axially Symmetrical Flows About or Within Arbitrary Boundaries," Douglas Aircraft Report ES-26988 (1958).
28. McCarthy, J.H. et al., "The Roles of Transition, Laminar Separation, and Turbulence Stimulation in the Analysis of Axisymmetric Body Drag," The Eleventh Office of Naval Research Symposium on Naval Hydrodynamics, London, England (1976).
29. Eggers, H.A., "Wake Survey of the Mark 13 Torpedo," David Taylor Model Basin Report 583 (1947).



30. Cebeci, T. et al., "*A Finite-Difference Method for Calculating Compressible Laminar and Turbulent Boundary Layers*," Douglas Aircraft Report DAC-67131 (1969).
31. Kerwin, J.E. and R. Leopold, "*A Design Theory for Subcavitating Propellers*," Transactions of the Society of Naval Architects and Marine Engineers, Vol. 72, pp. 294-335 (1964).
32. Thwaites, B., "*Incompressible Aerodynamics*," Oxford University Press (1960), Chapter XI.
33. Huang, T.T., "*User's Manual for a Fortran IV Computer Program for Calculating Propeller/Stern Boundary-Layer Interaction on Axisymmetrical Bodies*," DTNSRDC Report SPD-737-02 (1976).
34. Cummings, D.E., "*Numerical Prediction of Propeller Characteristics*," Journal of Ship Research, Vol. 17, Pt 3, pp. 12-18 (1973).
35. Cox, G.G. and W.B. Morgan, "*Use of Theory in Propeller Design*," Marine Technology, Vol. 2, No. 4, pp. 319-329 (1972).
36. Morgan, W.B. et al., "*Propeller Lifting-Surface Corrections*," Transactions, the Society of Naval Architects and Marine Engineers, Vol. 76, pp. 309-347 (1968).
37. Born, M. and E. Wolf, "*Principles of Optics*," Pergamon Press, New York (1965), p. 652.
38. Goethert, W.H. and D.B. Brayton, "*New Velocity Measuring Technique Using Dual Scatter Laser Doppler Shift*," Arnold Engineering Development Center AEDC-TR-205 (1970).
39. Yanta, W.J., "*Turbulence Measurements with a Laser Doppler Velocimeter*," Naval Ordnance Laboratory NOLTR-73-94 (1973).
40. Kalb, H.T. et al., "*Laser Velocimetry Data Processing*," Arnold Engineering Development Center AEDC-TR-73-116 (1973).
41. Reischman, M.M. and W.G. Tiederman, "*Laser-Doppler Anemometer Measurements in Drag Reducing Channel Flows*," Journal of Fluid Mechanics, Vol. 70, Pt 2, pp. 369-382 (1975).

# INITIAL DISTRIBUTION

## Copies

1 DOD, ARPA G. Donahue  
 1 WES  
 1 U.S. ARMY TRAS R&D  
 Marine Trans Div  
 1 CHONR/438 Cooper  
 2 NRL  
     1 Code 2027  
     1 Code 2629  
 1 ONR/Boston  
 1 ONR/Chicago  
 1 ONR/New York  
 1 ONR/Pasadena  
 1 ONR/San Francisco  
 1 NORDA  
 3 USNA  
     1 Tech Lib  
     1 Nav Sys Eng Dept  
     1 B. Johnson  
 3 NAVPGSCOL  
     1 Library  
     1 T. Sarpkaya  
     1 J. Miller  
 1 NADC  
 1 NELC/Lib  
 4 NUC, San Diego  
     1 Library  
     1 T. Lang  
     1 J.W. Hoyt  
     1 D.M. Nelson  
 1 NCSL/712 D. Humphreys  
 1 NCEL/Code 131  
 1 NSWC, White Oak/Lib  
 1 NSWC, Dahlgren/Lib  
 1 NUSC/Lib

## Copies

7 NAVSEA  
     1 SEA 0322  
     1 SEA 033  
     1 SEA 03512/Peirce  
     1 SEA 037  
     3 SEA 09G32  
 1 NAVFAC/Code 032C  
 1 NAVSHIPYD PTSMH/Lib  
 1 NAVSHIPYD PHILA/Lib  
 1 NAVSHIPYD NORVA/Lib  
 1 NAVSHIPYD CHASN/Lib  
 1 NAVSHIPYD LBEACH/Lib  
 2 NAVSHIPYD MARE  
     1 Library  
     1 Code 250  
 1 NAVSHIPYD BREM/Lib  
 1 NAVSHIPYD PEARL/Code 202.32  
 8 NAVSEC  
     1 SEC 6034B  
     1 SEC 6110  
     1 SEC 6114H  
     1 SEC 6120  
     1 SEC 6136  
     1 SEC 6140B  
     1 SEC 6144  
     1 SEC 6148  
 1 NAVSEC, NORVA/6660.03 Blount  
 12 DDC  
 1 AFOSR/NAM  
 1 AFFOL/FYS, J. Olsen  
 2 MARAD  
     1 Div of Ship R&D  
     1 Lib  
 1 NASA HQS/Lib  
 3 NBS  
     1 Lib  
     1 P.S. Klebanoff  
     1 G. Kulin  
 1 NSF/Eng Lib

## Copies

- 1 LC/Sci & Tech
- 1 DOT/Lib TAD-491.1
- 2 MMA
  - 1 National Maritime Research Center
  - 1 Library
- 1 U. of Bridgeport/E. Uram
- 4 U. of Cal/Dept Naval Arch, Berkeley
  - 1 Library
  - 1 W. Webster
  - 1 J. Paulling
  - 1 J. Wehausen
- 2 U. of Cal, San Diego
  - 1 A.T. Ellis
  - 1 Scripps Inst Lib
- 5 CIT
  - 1 Aero Lib
  - 1 T.Y. Wu
  - 1 A.J. Acosta
  - 1 I. Sabersky
  - 1 D. Coles
- 1 City College, Wave Hill/Pierson
- 1 Catholic U. of Amer./Civil & Mech Eng
- 1 Colorado State U./Eng Res Cen
- 1 U. of Connecticut/Scottron
- 1 Cornell U./Shen
- 2 Florida Atlantic U.
  - 1 Tech Lib
  - 1 S. Dunne
- 2 Harvard U.
  - 1 G. Carrier
  - 1 Gordon McKay Lib
- 1 U. of Hawaii/Bretschneider
- 1 U. of Illinois/J. Robertson
- 4 U. of Iowa
  - 1 Library
  - 1 L. Landweber
  - 1 J. Kennedy
  - 1 V.C. Patel
- 1 Johns Hopkins U./Phillips
- 1 Kansas State U./Nesmith
- 1 U. of Kansas/Civil Eng Lib

## Copies

- 1 Lehigh U./Fritz Eng Lab Lib
- 5 MIT
  - 1 Library
  - 1 P. Leehey
  - 1 P. Mandel
  - 1 M. Abkowitz
  - 1 J.N. Newman
- 4 U. of Minn/St. Anthony Falls
  - 1 Silberman
  - 1 Lib
  - 1 Song
  - 1 R. Arndt
- 4 U. of Mich/NAME
  - 1 Library
  - 1 F. Ogilvie
  - 1 Hammitt
  - 1 Cough
- 2 U. of Notre Dame
  - 1 Eng Lib
  - 1 Strandhagen
- 2 New York U./Courant Inst
  - 1 A. Peters
  - 1 J. Stoker
- 4 Penn State
  - 1 B.R. Parkin
  - 1 R.E. Henderson
  - 1 J.L. Lumley
  - 1 ARL Lib
- 1 Princeton U./Mellor
- 2 U. of Rhode Island
  - 1 F.M. White
  - 1 T. Kowalski
- 5 SIT
  - 1 Library
  - 1 Breslin
  - 1 Savitsky
  - 1 P.W. Brown
  - 1 Tsakonas
- 1 U. of Texas/Arl Lib
- 1 Utah State U./Jeppson
- 2 Southwest Res Inst
  - 1 Applied Mech Rev
  - 1 Abramson

Copies

- 3 Stanford U.
  - 1 Eng Lib
  - 1 R. Street, Dept Civil Eng
  - 1 S.J. Kline, Dept Mech Eng
- 1 Stanford Res Inst/Lib
- 1 U. of Washington/Arl Tech Lib
- 3 VPI
  - 1 H.L. Moses, Dept Mech Eng
  - 1 D.P. Telionis, Dept Mech Eng
  - 1 J. Schetz, Dept Aero & Ocean Eng
- 3 Webb Inst
  - 1 Library
  - 1 Lewis
  - 1 Ward
- 1 Woods Hole/Ocean Eng
- 1 Worchester PI/Tech Lib
- 1 SNAME/Tech Lib
- 1 Bethlehem Steel/Sparrows Point
- 1 Bethlehem Steel/New York/Lib
- 1 Bolt, Beranek & Newman/Lib
- 1 Exxon, NY/Design Div, Tank Dept
- 1 Exxon Math & System, Inc.
- 1 General Dynamics, EB/Boatwright
- 1 Gibbs & Cox/Tech Info
- 4 Hydronautics
  - 1 Library
  - 1 E. Miller
  - 1 V. Johnson
  - 1 C.C. Hsu
- 1 Lockheed, Sunnyvale/Waid
- 2 McDonnell Douglas, Long Beach
  - 1 T. Cebeci
  - 1 J. Hess
- 1 Newport News Shipbuilding/Lib
- 1 Nielsen Eng & Res
- 1 Oceanics
- 3 Rand Corp
  - 1 E.R. Van Driest
  - 1 C. Gazley
  - 1 J. Aroesty

Copies

- 1 Rockwell International/B. Ujihara
- 1 Sperry Rand/Tech Lib
- 1 Sun Shipbuilding/Chief Naval Arch
- 1 Robert Taggart
- 1 Tracor
- 2 Westinghouse Electric
  - 1 M.S. Macovsky
  - 1 Gulino



# CENTER DISTRIBUTION

Copies	Code		Copies	Code	
1	012	R.C. Allen	1	1560	G. Hagen
1	11	W.M. Ellsworth	1	1562	M. Martin
1	117	R.M. Stevens	1	1564	J. Feldman
1	1500	W.E. Cummins	1	1568	G. Cox
1	1504	V.J. Monacella	1	1572	M.D. Ochi
1	1506	M.K. Ochi	1	1572	E. Zarnick
1	1507	D. Cieslowksi	1	1572	C.M. Lee
1	1508	F. Peterson	1	1576	W.E. Smith
1	1512	J.B. Hadler	1	1615	R.J. Furey
1	1520	R. Wermter	1	1802.2	F. Frenkiel
1	1521	P. Pien	1	183	E. Cuthill
1	1524	Y.T. Shen	1	184	H. Lugt
1	1524	W.C. Lin	1	1843	J. Schot
1	1524	Day	1	1843	C. Dawson
1	1524	Scragg	1	19	M.M. Sevik
1	1532	G. Dobay	1	1942	J.T. Shen
1	1532	M. Wilson	1	1942	W.R. Brown
1	1540	W.B. Morgan	1	1942	F.C. DeMetz
1	1541	Granville	1	1942	T.M. Farabee
1	1542	Yim	1	1942	F.E. Geib
1	1544	Cumming	1	1942	T.C. Mathews
1	1544	Boswell	1	1946	Anechoic Flow Facility (J. Padgett)
1	1544	Caster			
1	1544	Cox	30	5214.1	Reports Distribution
1	1544	Lafone	1	5221	Unclassified Library (C)
1	1544	Jessup	1	5222	Unclassified Library (A)
1	1544	Valentine			
1	1552	J. Bai			
1	1552	M. Chang			
30	1552	T.T. Huang			
1	1552	N. Groves			
1	1552	N. Santelli			
1	1552	N. Salvesen			
1	1552	C. von Kerczek			
10	1552	H.T. Wang			
1	1552	Brockett			
1	1552	J. McCarthy			